Gesture Sensing with Flexural Ultrasonic Transducers

by

Julia Claire Canning

Submitted to the Department of Mechanical Engineering
in partial fulfillment of the requirements for the degree of

Master of Science in Mechanical Engineering

at the

MASSACHUSETTS INSTITUTE OF TECHNOLOGY

June 2019

Signature redacted

Author .....
Department of Mechanical Engineering
May 10, 2019

Signature redacted

Certified by .....
Alexander Slocum
Walter M. May & A. Hazel May Professor of Mechanical Engineering
Thesis Supervisor

Signature redacted

Accepted by .....
Nicolas Hadjiconstantinou
Chairman, Department Committee on Graduate Theses

Gesture Sensing with Flexural Ultrasonic Transducers

by

Julia Claire Canning

Submitted to the Department of Mechanical Engineering
on May 10, 2019, in partial fulfillment of the
requirements for the degree of
Master of Science in Mechanical Engineering

Abstract

As everyday devices become increasingly interactive, there is a need for improved interface sensors between humans and machines, as well as for expansion of the form factors and materials through which such sensors can operate. This thesis explores sensing technologies to enable user input on a consumer electronics device, specifically technologies that are capable of sensing touch and hover gestures through a metal substrate. Electromagnetic, optical, and acoustic technologies are explored. Capacitive and pinhole camera approaches for sensing through a mostly metal substrate are presented briefly. The bulk of the thesis focuses on the development of an array of flexural ultrasonic transducers to allow sensing through a fully metal substrate. An analytical model, finite element simulations, and experiments are presented to characterize and optimize the transducers, and a prototype is developed as a proof of concept of the combined touch and hover sensor system. The prototype successfully demonstrates the capability of a mesoscale piezo unimorph array to detect and distinguish between tap, touch, and swipe contact gestures and to detect a hovering object, albeit in a limited range, above a metal substrate. There are opportunities for improvements in circuitry, sensor design, and fabrication that could lead to finer resolution, decreased sensor size, and a larger range for hover detection.

Thesis Supervisor: Alexander Slocum
Title: Walter M. May & A. Hazel May Professor of Mechanical Engineering

Thesis Errata Sheet

Author Julia Canning

Primary Dept. Department of Mechanical Engineering

Degree Master of Science **Graduation date** Jun 2019

Thesis title

Gesture Sensing with Flexural Ultrasonic Transducers

Brief description of errata sheet

Errata sheet includes corrections to equations used to calculate resonant frequency and sensitivity, as well as a correction to a reference.

Number of pages 3 (11 maximum, including this page)

▶ **Author**: I request that the attached errata sheet be added to my thesis. I have attached two copies prepared as prescribed by the current *Specifications for Thesis Preparation*.

Signature of author Signature redacted Date 5/31/2021

▶ **Thesis Supervisor** or **Dept. Chair**: I approve the attached errata sheet and recommend its addition to the student's thesis.

Signature redacted 6/3/2021

Signature _____ Date _____

Name Alexander Slocum X ☐ Thesis supervisor ☐ Dept. Chair

▶ **Vice Chancellor or his/her designee**:

I approve the attached errata sheet and direct the Institute Archives to insert it into all copies of the student's thesis held by the MIT Libraries, both print and electronic.

Signature Signature redacted Date 10/28/21

Name Ian Waitz

Errata

Entry 1

Page 65, line 8

$f = \frac{\pi}{2a^2}\sqrt{\frac{D}{I0}\beta_{00}^2}$ should read $f = \frac{\pi}{2a^2}\sqrt{\frac{D}{I0}}\beta_{00}^2$

Entry 2

Page 73, Figure 4-10

r_{ef} should read r_{ref}

Entry 3

Page 75, line 2

$D_C = \frac{Y_c h_p^3}{12(1-\upsilon_c))}$ should read $D_C = \frac{Y_c(h_m+h_p)^3}{12(1-\upsilon_c)}$

Entry 4

Page 75, line 11

$$B_1 = 2abh_m h_p S_{11} S_m\left(h_m^3 S_{11} + h_p^3 S_m\right) + b^2 h_p^2 S_m^2\left(4h_m^3 S_{11} + 6h_m^2 h_p S_{11} + 3h_m h_p^2 S_{11} + h_p^2 S_m\right) + a^2 h_m^2 S_{11}^2\left(h_m^3 S_{11} + 3h_m^2 h_p S_m + 6h_m h_p^2 S_m + 4h_p^3 S_m\right)$$

should read

$$B_1 = 2abh_m h_p S_{11} S_m\left(h_m^3 S_{11} + h_p^3 S_m\right) + b^2 h_p^2 S_m^2\left(4h_m^3 S_{11} + 6h_m^2 h_p S_{11} + 3h_m h_p^2 S_{11} + h_p^3 S_m\right) + a^2 h_m^2 S_{11}^2\left(h_m^3 S_{11} + 3h_m^2 h_p S_m + 6h_m h_p^2 S_m + 4h_p^3 S_m\right)$$

Entry 5

Page 76, line 6

Insert the following text after line 6: In order to calculate the sensitivity over the full disk, *Sensitivity* is multiplied by the area of the piezo disk, πb^2.

Entry 6

Page 99, line 3

Insert the following text after line 3: The analytical model assumes the piezo is ideally bonded to the substrate, which may explain the discrepancy between it and the experimental and simulated results. If $(h_m + h_p)$ is replaced by a thickness between that of the membrane and the composite, the value is in line with experimental and simulated results.

Entry 7

Page 99, Table 4.2

Analytical sensitivity should be 1.2mVpp/Pa instead of 0.4mVpp/Pa

Entry 8

Page 154, line 25

Reference [18] should read: R. Liang and Q. Wang, "High sensitivity piezoelectric sensors using flexible PZT thick-film for shock tube pressure testing," *Sensors and Actuators A: Physical,* vol. 235, pp. 317-327, Nov. 2015. [Online]. Available: http://dx.doi.org/10.1016/j.sna.2015.09.27

Acknowledgments

I would like to thank my advisor, Alex Slocum, for his support and guidance over the past two years. I have learned so much from your suggestions and insights over the course of this project. Thank you also for demonstrating how to approach challenges with enthusiasm while maintaining balance in life and for encouraging your students to do the same.

Thank you to my sponsors for supporting this project and for giving me the freedom to run with it. Thank you for the design suggestions, guidance, feedback, and resources you have given me. It has been amazing to learn from so many bright people. Thanks in particular to Kate Bergeron for authorizing and arranging this project, Ed Siahaan for mentoring me directly on this project, and Kurt Stiehl for helping set up this project and for starting me off with design suggestions.

Thank you to Professor Lang and Professor Trumper for sharing your insights on this project. I went into this with little background in electrical engineering, and the knowledge I gained from your classes and from conversations with you was incredibly valuable. Thank you also to other professors and graduate students who have lent an ear and offered expertise and advice along the way.

Thanks to my lab mates in PERG for all the laughter. I appreciate your friendship, support, and engineering insights. It's been amazing to be in a group that works on such a wide range of interesting projects.

Thanks to the MechE administrative staff for all that you do to support students. In particular, thank you to Irina Gaziyeva for supporting everyone in PERG.

Thanks to MIT MakerWorkshop for providing me with another community in grad school. MW has been a place to go spend time with friends and work on fun projects, both of which improved my time in the master's program.

Thanks finally to my family and friends, especially to my parents, brother, and sister and to Wilson. Thank you for your love, support, and encouragement always.

Contents

List of Figures

List of Tables

Chapter 1

Introduction

Gesture recognition is becoming ubiquitous as a method for human-machine interaction. Consumer products like smartphones, tablets, laptops, and smartwatches make use of touch gestures to allow users to navigate the screen. Gaming consoles like the Xbox 360 recognize non-contact body and hand gestures, allowing players to play a game without physical controllers. VR headsets and car consoles are among other systems that use non-contact hand gestures as controls. In medicine, non-contact gesture recognition presents surgeons with the possibility of reviewing patient files without breaking scrub, which reduces surgery times. As the market for gesture recognition systems continues to grow and new applications for the technology are identified, the industry will benefit from increased flexibility in sensor materials, form factors, and recognized gesture types.

1.1 Problem Statement

The goal of this thesis is to investigate sensing technologies to enable user input on a consumer electronics product; the technology should:

- Accept user inputs including touch, tap, and swipe finger gestures
- Accept two categories of the above inputs:
  - contacting the sensing substrate

  - away from the sensing substrate

- Fit into a small mechanical volume

- Work through metal substrates, among others

This sensing technology would be applicable to a myriad of applications ranging from wearable to stationary consumer electronics.

1.2 Functional Requirements

Based on the above problem statement, a number of functional requirements and design parameters were identified and are shown in Table 1.1, which is organized by importance with the most important requirements at the top. For the scope of this thesis, particular attention was paid to the categories of modes through size. Future work will be required to thoroughly investigate the remaining requirements.

1.2.1 Modes

The sensor should have two modes of operation that it can switch between: touch and hover. In touch mode, gestures contacting the surface of the substrate are detected. In hover mode, gestures between 2 and 100 mm above the surface are detected. The low range for hover gestures was chosen such that there would be a buffer between touch and hover operation to prevent confusion between gestures. The high range was chosen with personal devices in mind. The sensor should detect intentional inputs from the user and disregard unintentional inputs from the user, inputs from other users and inputs from the environment. A limited sensing range helps to differentiate between intentional and unintentional inputs and minimize power consumption.

1.2.2 Gestures

Three gestures were targeted for initial development, with the option of including more complex gestures later on. These three gestures were chosen for their simplicity

Table 1.1: Functional requirements and design parameters.

Functional Requirements		**Design Parameters**
Modes	Touch	Contacting Surface
	Hover	2 - 100mm range from surface
Gestures (for both modes)	Stationary Input	Duration >250ms
	Swipe Input	Velocities between 200 and 500 mm/s
	Tap Input	Duration <250ms
Substrate	Solid Metal	Unbroken Surface, Thickness >0.4mm (Al)
	Perforated Metal	Holes or lines with width or diameter < 400 microns
	Other (Plastic, Glass, etc.)	Unbroken Surface, Thickness of >0.7mm
Size	Fits in a Small Mechanical Volume	Occupies Surface Area <25 Square Centimeters
		Occupies Thickness <10mm
Robustness	Works in the Presence of Water Droplets	User Can Still Input Commands
	Works in the Presence of Rain	User Can Still Input Commands, No Accidental Inputs from Rain Droplets
	Resistant to Moisture, Water, and Other Contaminants	User Can Still Input Commands
	Robust to Environment	Not Triggered by Other Objects, Ambient Noise or Light, Motion, etc.
Form	Works Through Curved Surfaces	Radius of Curvature >7.5mm
Power	Low Power Consumption	<100 mW Active
Performance Specifications	Field of View	$\pm 45^o$
	Resolution	Spatial Resolution (X,Y,Z): millimeter range (<1cm)
		Velocity Resolution: <1mm/s
	Signal to Noise Ratio	20x
Manufacturability	Easy to Manufacture	Scalable

and for their ubiquity in current human-machine interfaces. Each gesture has a touch version and a hover version. A stationary input is one in which the user places their hand on or above the surface for a duration of at least 250 ms. A tap input is a similar, but shorter duration, event in which the user places their hand on or above the surface for a period of less than 250 ms and then removes it. This threshold was picked based on values from informal user testing. A swipe gesture involves the user moving their hand horizontally above the surface or moving their finger along the surface at a velocity between 200 and 500 mm/s. The velocity was set based on values reported in literature [7].

1.2.3 Substrate

One of the primary goals of this work was to investigate sensing technologies that would enable designers to use a wide range of materials in interactive devices and that would have a minimal impact on the aesthetics of a consumer device. Ideally, the technology would work through a solid metal surface. However, for initial investigation, this requirement was relaxed to include substrates that have a similar appearance to solid metal. This includes metal surfaces with small, regular features such as holes or gaps, which can be filled with a non-metal material.

1.2.4 Size

The desired sensor size was chosen based on the size of some common consumer devices. Potential use locations for the sensor system explored in this research include the surface of a smartphone, a smartwatch, a touchpad, headphones, or earbuds. The largest of these surfaces span a few inches, the smallest about a centimeter. A target area of 25 square centimeters and thickness of 1 centimeter were chosen for the sensor prototypes, with the potential for miniaturization. At the chosen size, prototypes are easier to fabricate and could work in the larger of the identified products.

1.2.5 Robustness

The sensor system should be robust to the environment in which it is operated, which may be indoors or outside. It should work in the presence of water droplets or rain, meaning it should recognize inputs from the user and should not mistake inputs from the water droplets as user inputs. The system should also be capable of rejecting other false inputs, such as those caused by the presence of other objects, contaminants other than water, ambient noise, light, or motion.

Chapter 2

Prior Art

A wide variety of approaches to gesture sensing have been explored in literature. These approaches are reviewed and evaluated for their fulfillment of the identified functional requirements. Particular attention is paid to detectable modes (touch and/or hover), target requirements, and ability to sense through various substrates. The prior work has been grouped into three sensing modalities: electromagnetic, optical, and acoustic.

2.1 Electromagnetic Methods

Electromagnetic methods for gesture sensing fall into three main categories: inductive, resistive, and capacitive.

Inductive sensors typically consist of a coil and an oscillator, which generate a high frequency magnetic field that radiates from the device. When a conductive target enters the field, an eddy current is induced in the target, changing the load on the magnetic circuit, shifting its natural frequency, and causing a decrease in oscillation amplitude. The closer the target, the larger the eddy current and the lower the oscillation amplitude [13]. This sensing method works best for good conductors, such as metals. Inductive sensors can also detect magnetizable targets that are poor conductors, although not through eddy-currents. Inductive sensors were not considered for this research as they would require the use of certain materials as an accessory to

interact with the device, which is not desirable from a user experience perspective.

Resistive sensors are a contact method for sensing touch. A common type is a piezoresistive sensor, which is made of a material that experiences a change in electrical resistivity under mechanical strain. Another type of resistive sensor consists of two conductive layers separated by an air gap; the device is activated when a user applies a force to the top layer, causing it to bend and contact the bottom layer. There are voltage gradients along x and y on one of the surfaces, so when the two layers come in contact, the system acts like a voltage divider. The voltage can be probed on the non-graduated surface to determine the position of the contact point [2]. Resistive sensors were not considered for this research because they require contact with the sensor surface, so they cannot detect hover.

Capacitive sensors can be used for both touch and hover sensing; these sensors detect a change in the capacitance of a system upon the introduction of a finger, which has a high dielectric constant that will increase the value of a capacitor. Capacitive touch screens fall into two broad categories: surface capacitive and projected capacitive. Surface capacitive sensors consist of a uniform conductive layer mounted behind an insulator with wires at each corner that deliver a small voltage to the conductor. When a finger touches the surface, a small current flows to that location, which causes a voltage drop at each corner related to the distance from the corner to the contact point. The x,y position of the contact point can be obtained from these readings [35]. Projected capacitive screens have two conductive layers separated by an insulator forming a grid pattern. Within projected capacitive screens, there are two subcategories: self-capacitive and mutual-capacitive. Self-capacitive screens measure the sum of the self-capacitance of the device and the capacitance added by the finger. The capacitance between a row electrode and ground and between a column electrode and ground are recorded and indicate the contact location. Mutual-capacitive screens, on the other hand, measure the capacitance between electrodes, so the capacitance at each electrode intersection can be measured [2].

Capacitive proximity sensors can be used to detect targets further from the sensing surface. Sensors include a conductive base layer and a smaller conductive layer above

the base layer separated by an air gap. The plates are held at different potentials, so they act like an open capacitor. The plates are driven by an oscillator, and when a target approaches the surface the capacitance of the plates increases, causing an increase in the oscillation amplitude [14]. Capacitive proximity sensors have been applied to sense hover. For instance, Microchip's GestIC technology uses an electric field for proximity sensing up to a range of 200mm. However, the range is directly proportional to the electrode size, so the range decreases as the product form factor shrinks [21]. Capacitive sensors were chosen for further exploration, described in chapter 3.

2.2 Optical Methods

Common optical methods for gesture sensing include infrared (IR) systems and visible light camera-based systems.

IR systems can be classified as active or passive. Active IR systems emit a burst of IR light that travels toward a target and is reflected back toward a receiver. Izadi et al. present such a device with optosensors mounted behind an liquid-crystal display (LCD) screen. As fingers approach the screen, they appear as blobs that increase in intensity as they near the surface [10]. Cheng et al. present a non-contact gesture recognition system that uses two IR light-emitting diodes (LEDs) and an IR receiver placed behind plastic or glass. The system recognizes gestures like swipe, push, and pull with 98 percent precision [4].

Other groups have explored passive IR gesture sensing with systems that detect IR radiation emitted by warm bodies. Wojtczuk et al. use a passive thermal infrared sensor array to pick up IR waves emitted from the human body. They use a 16 element array to identify four directions of a swipe gesture, in which a hand is waved over the array [40].

Visible light camera-based systems for gesture recognition have also been explored and presented in literature. Traver et al. present an integral imaging system using camera arrays that can recognize gestures through occlusions. Each camera captures

a slightly different view of the object, enabling 3D scene reconstruction, and the image can be focused at different depths [37]. Chang et al. use pinhole array cameras to capture light field data for depth estimation [3]. Hirsch et al. use tiled broadband masks in place of pinholes to achieve a similar effect but let in more light [9]. Pinhole imaging systems are capable of real-time depth estimation and touch plus gesture interaction. Other approaches use a single video camera to capture the scene and then apply computer vision algorithms to recognize gestures [10].

Both IR and visible light camera-based systems were chosen for further exploration, as certain subsets of each could potentially be adapted to work through a metal grid with small, regular perforations.

2.3 Acoustic Methods

Acoustic methods have been explored for both touch and hover gesture recognition.

2.3.1 Touch Sensors

A variety of configurations of touch sensors have appeared in industry and in literature. One common approach is known as Surface Acoustic Wave (SAW) sensing. In SAW sensing, transmitters, receivers, and reflectors are positioned along the edges of a sheet of glass such that they direct a grid of acoustic waves along the front surface of the glass. When a finger comes into contact with a point on the surface, it absorbs the acoustic waves and a drop in amplitude at the receiver is observed, signaling a touch event [36].

Alonso-Martin et al. present a system for detecting touch in a robot that uses the audio signals from contact microphones adhered to the robot's shell. The authors apply machine learning to recognize different types of touch gestures [1]. Lamberti et al. present a track-pad based on a vibrating piezoelectric bimorph. When a stylus touches the surface, it changes the displacement field at that point, resulting in a change in the electrical input impedance of the device. The stylus position can then be determined based on the change in impedance [15].

Tang et al. present an ultrasonic fingerprint sensor, which consists of an array of piezoelectric micromachined ultrasonic transducers (PMUTs) mounted behind a layer of Fluorinert and a plastic lid. The transducers are driven simultaneously to generate a plane wave that travels through the intermediate layers to the fingertip. The air in the valleys of the fingertip have a strong impedance mismatch with the intermediate layers, causing a strong reflection, while the skin has an impedance closer to that of the intermediate layers, resulting in a weaker reflection. The resulting pattern can be detected and used to identify the user [33]. Qualcomm has recently released an ultrasonic fingerprint sensor that can work through a layer of glass or aluminum several hundreds of microns thick [23].

2.3.2 Hover Sensors

Typically, hover systems consist of one or more transmitters, which emit an acoustic signal into the air above the device, and one or more receivers, which pick up signals directed toward the device. If an object is present in the interaction space, the transmitted signals will be reflected off the object and picked up by the receivers. Based on the transmitted and received signals, the system can obtain information about the position and motion of the object, as well as the frequency response of the system, which varies based on object position and motion. Gesture classification is often performed by combining some subset of this information to define gestures.

A number of papers have explored hover recognition using off-the-shelf (OTS) acoustic sensor systems. For instance, Gupta et al. demonstrate that the speaker and microphone already embedded in a computer can be used to detect gestures that involve motion of the hand. The system uses frequencies at the high end of what audio speakers can emit, between 18 and 22 kHz, so that the signals are inaudible to most people. The authors measure the frequency shift between the transmitted and received signal and use it to infer information about the velocity, direction, proximity, and size of the target, as well as information about the time variation of the four preceding factors. The authors combine these factors to produce a set of gestures [7]. Sang et al. use a commercially available ultrasound transceiver operating at 300kHz

to recognize micro hand gestures. The authors use pulsed radar signal processing techniques, which result in time-sequential Range-Doppler features, to obtain information about the distance and velocity of nearby objects. The authors use machine learning, specifically a Hidden Markov Model, to characterize gestures based on the range-Doppler features [29].

Other groups make use of a single transmitter with an array of receivers. For instance, Willigen et al. use an OTS piezoelectric transmitter with a resonant frequency of 40kHz and an array of commercially available microelectromechanical systems (MEMS) microphones. The receiver array enables beamforming, which makes the array receptive only to signals coming from a certain direction and allows the authors to estimate the location of the object. The system tracks the position of the object and identifies certain sequences as gestures [39]. Kalgaonkar and Raj also use a single OTS transmitter and an array of OTS receivers. The three receivers each pick up a signal that has been reflected off of a moving hand and has undergone a frequency shift based on the velocity of the hand. The result is a time-dependent reading of the hand's velocity in multiple directions, which is used to recognize gestures [11].

A number of other groups have developed custom sensor arrays that can be used for gesture recognition with a smaller form factor. For instance, Pang and Chiang present a transparent capacitive micromachined ultrasonic transducer (CMUT) array with 12 transducers operating at different frequencies. Each transducer is used to measure the time and frequency response of a transmitted signal that is reflected off a finger, and the finger's position is identified based on the reflected signal's frequency [27]. Pryzbyla et al. present a PMUT array comprising 2 transmitters and 7 receivers, which localizes objects using pulse-echo time-of-flight measurements and beamforming. The array has a maximum dimension of approximately 5mm [28]. The company Chirp Microsystems grew out of this research at UC Berkeley and Davis and has commercialized PMUT systems for ultrasonic time-of-flight sensing [34].

2.3.3 Touch and Hover Sensors

Fewer groups have published on systems capable of both touch and hover detection. Tsuruta et al. from the University of Tsukuba present work that uses a piezoelectric microphone and a speaker of the same construction to detect touch and hover gestures on and around a variety of household objects. The microphone and speaker are adhered to the object with double sided tape, and the speaker excites the object with a sine sweep from 20kHz to 40kHz to obtain the frequency response of the object, which depends on how the user manipulates it. The frequency spectrum is run through a Support Vector Machine (SVM) which classifies it as a certain gesture [38].

2.3.4 Synopsis

One shortcoming of all of these approaches to hover sensing is that the transducers must be exposed to air, which limits the design space when incorporating the technology into products. In the work by Tsuruta et al, the sensors are placed on the exterior surface of existing objects, where they are visible to users. In the work by Pryzbyla et al, the PMUT array must be exposed to air, necessitating holes in the exterior casing of products. The off-the-shelf components used by other groups often are bulky and intended for prototyping or for applications, such as car back-up sensors, with more available space than wearables and other consumer electronics devices. A major goal of this work is to create a sensing technology that can be integrated seamlessly into product shells of a variety of materials, so that designers do not need to compromise the aesthetics of a product to include interactivity. An additional benefit to a lack of seams or holes in a product is that the technology lends itself to less ideal environments, such as outdoor applications where products might be exposed to rain. Ultrasonic sensors were chosen for further exploration in this thesis.

2.4 Comparison with Functional Requirements

While there are many approaches to sensing touch and hover gestures, there are no systems, to the author's knowledge, that can sense both touch and hover through a metal surface. The ability to sense through metal would open up the design space for interactive products, with a few notable benefits. Designers would have more options when making choices about the aesthetics of a product. Sensing surfaces could more easily serve as structural elements of a device. Sensors could also become more robust to impacts, heat, and other factors, which would allow them to be used in more extreme environments.

For these reasons, the requirements of supporting touch and hover modes and operating through metal substrates were prioritized. Specifically, the surfaces must have a regular appearance and be made primarily of metal. For instance, a metal shell with an array of small perforations would be acceptable, as would an array of small but thick electrodes embedded in a non-conductive material. Such systems would still offer aesthetic benefits for product designers. The following methods were selected for further exploration: capacitive sensors, thermal sensors, pinhole arrays, and ultrasonic sensors. These systems are explored in chapter 3.

Chapter 3

Preliminary Experiments and Modality Selection

Three common sensing modalities were explored in the beginning of this project: electromagnetic, optical, and acoustic. Within each category, a literature review was conducted and a strategy that could come closest to meeting the functional requirements set forth above was selected for further exploration, which ranged from analytical work to experimental testing. The preliminary explorations of each area are summarized in this section.

3.1 Electromagnetics

Capacitive sensing was selected as the most promising of the electromagnetic approaches, as it can detect the human hand in both touch and hover cases without requiring any accessories to be worn or held by the user. Traditionally, capacitive grids are placed behind a surface made of glass or another insulating material. In order to achieve the appearance of a metal surface and maintain the ability to identify and localize touch and hover gestures, one could potentially move the electrodes to the surface of the device and maintain thin insulating walls between them. One way to do this would be to embed the electrodes in a plastic surface. The responsivity of this type of small electrode grid is explored below.

3.1.1 Capacitive Sensing with a Small Electrode Grid

This section focuses on preliminary calculations to assess the ability of a grid of small exposed electrodes to recognize touch and hover gestures. As two of the functional requirements of this project are that the system fits in a small mechanical space and maintains a regular pattern that comes close to the appearance of unbroken metal, a square grid of electrodes with size in the ones of millimeters was considered.

The first set of calculations is performed for a grid of square electrodes of alternating positive and negative potential. A single line of these electrodes is considered and is represented as a sinusoidal potential distribution. This approximation should hold as long as both the distance between the electrodes and the hand and the size of the hand are considerably larger than the length of the individual electrodes and the spacing between them. The hand is considered to be a perfect conductor, due to its high salt-water content. It is approximated as ground due to the body's large capacity to absorb charge. If the body is approximated as a sphere with radius of 0.5 m, it's capacitance can be calculated as $C = 4\pi\epsilon_0 R$ and turns out to be around 55 pF. The capacitance between two flat, coplanar electrodes can be calculated as [6]:

$$C = \frac{\epsilon_r l \ln\left(-\frac{2}{4\sqrt{1-\frac{s^2}{(s+2w)^2}}-1}\left(4\sqrt{1-\frac{s^2}{(s+2w)^2}}+1\right)\right)}{377\pi v_0} \quad for\ 0 < \frac{s}{s+2w} \leq \frac{1}{\sqrt{2}} \tag{3.1}$$

where ϵ_r is the relative permittivity of the medium in which the electrodes are embedded, l is the electrode length, s is the separation between electrodes, w is the electrode width, and v_0 is the speed of light in a vacuum. Assuming two 5 mm x 5 mm electrodes with a separation of 1 mm embedded in PC with $\epsilon_r = 3$, the capacitance is approximately 0.3 pF, which is significantly less than the capacitance of the human body.

A sketch of the proposed system is shown in Figure 3-1. The electric potential, Φ, is calculated as

$$\Phi = v\sin(kx)\frac{\sinh(k(z-G))}{\sinh(-kG)} \tag{3.2}$$

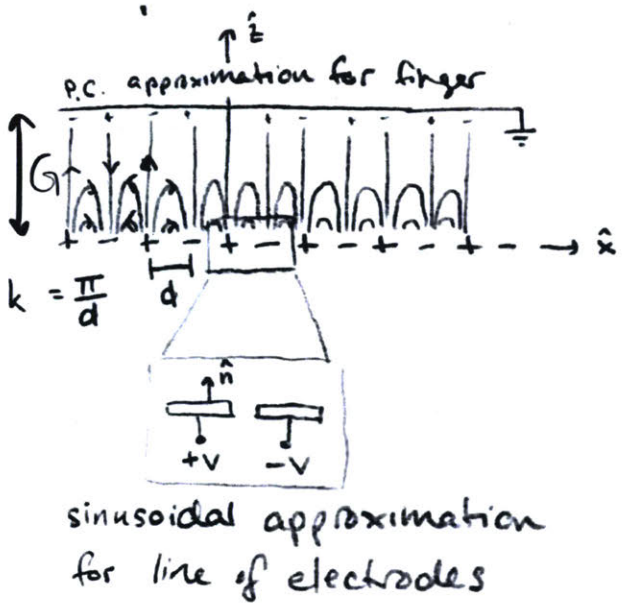

Figure 3-1: Sketch showing a simplified representation of a row of electrodes with alternating positive and negative voltage and a hand hovering above the electrodes.

where v is voltage, k is equal to π/d, d is the spacing between neighboring electrodes, z is the height of the point of interest above the electrodes, and G is the gap between the hand and the electrodes. The equipotential lines are plotted in Figure 3-2.

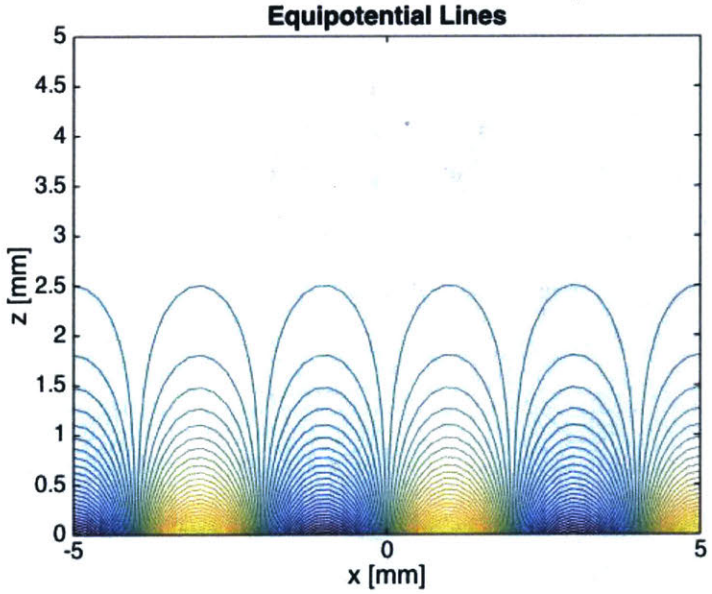

Figure 3-2: Equipotential lines between a row of electrodes with alternating voltage and a hovering hand. Colors correspond to potential values.

The electric field, E, can then be written as

$$E = -\nabla\Phi = -v\cos(kx)k\frac{\sinh(k(z-G))}{\sinh(-kG)}\hat{x} - v\sin(kx)\frac{\cosh(k(z-G))k}{\sinh(-kG)}\hat{z} \tag{3.3}$$

The surface charge density, σ_s, on the electrode can be found from the electric field, evaluated at z = 0, as

$$\sigma_s = \hat{n}\cdot\|\epsilon_0\bar{E}\| = v\epsilon_0 k\sin(kx)\frac{\cosh(-kG)}{\sinh(-kG)} \tag{3.4}$$

where ϵ_0 is the permittivity of a vacuum, 8.85e-12 $\frac{F}{m}$. The total charge, Q, on an electrode is

$$Q = d\int_0^{\frac{\pi}{k}} v\epsilon_0 k\sin(kx)\frac{\cosh(-kG)}{\sinh(-kG)}dx = \frac{2vd\epsilon_0\cosh(kG)}{\sinh(kG)} \tag{3.5}$$

The capacitance, C, between an electrode and the system is

$$C = \frac{Q}{v} = \frac{2d\epsilon_0\cosh(kG)}{\sinh(kG)} \tag{3.6}$$

The capacitance between an electrode and the system as a function of distance between the hand and the electrode is plotted in Figure 3-3. This capacitance is a combination of the capacitance due to fringing fields from adjacent electrodes and capacitance to the finger, represented by the parallel plate approximation. As shown, the capacitance drops off significantly and levels off within a distance of a few millimeters. The transition in the graph occurs around $\frac{2}{3}d$, which means objects must be within that distance from the sensor surface to be detected. A different voltage pattern was explored in order to increase the range. Rather than an alternating positive and negative voltage, a grid of electrodes with positive voltages and a guard shield with a negative voltage was considered. The same assumptions as above were made, and the simplified system is shown in Figure 3-4.

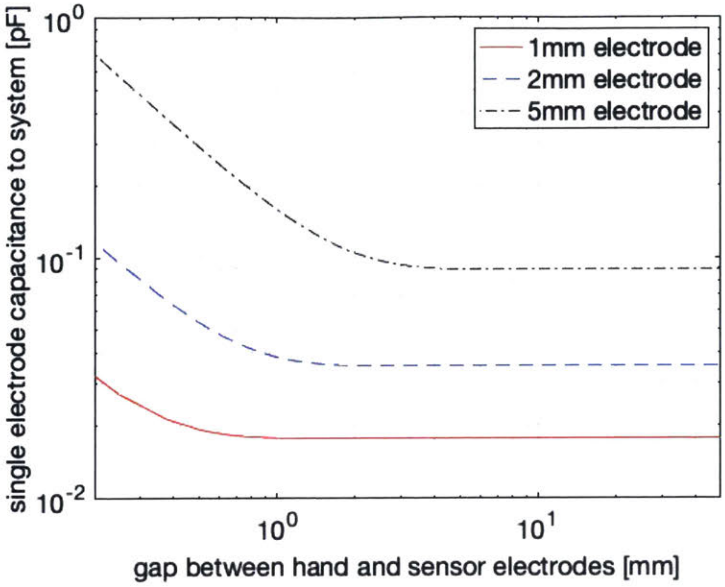

Figure 3-3: Capacitance between a single electrode and the system versus distance between the hand and the electrodes for electrodes with alternating voltage. The capacitance levels out at a distance of around two thirds of the electrode length.

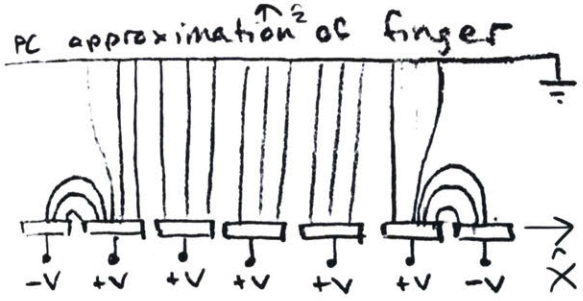

Figure 3-4: Sketch showing a simplified representation of a hand hovering above a row of electrodes with positive voltage and a negative guard shield.

In this case, the electric potential Φ, shown in Figure 3-5, is simply

$$\Phi = v - \frac{v}{G}z \tag{3.7}$$

The electric field, E, is

$$E = -\nabla\Phi = \frac{v}{G}\hat{z} \tag{3.8}$$

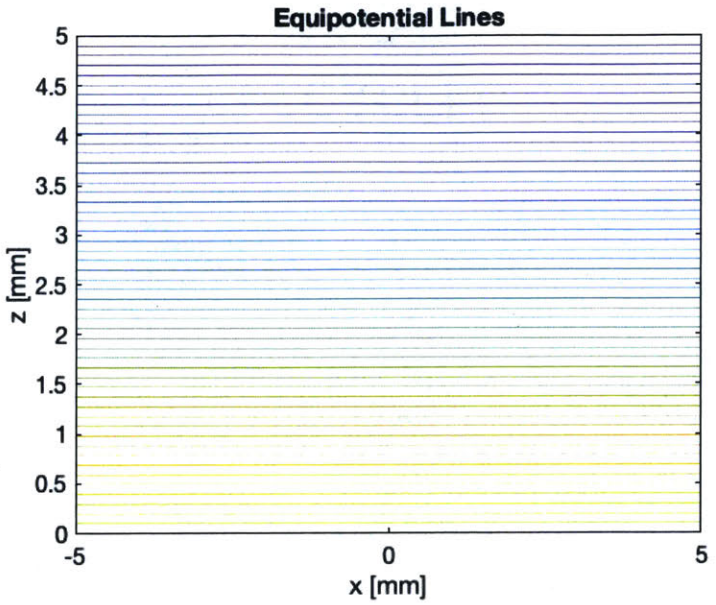

Figure 3-5: Equipotential lines between a row of electrodes with positive voltage surrounded by a negative guard shield and a hovering hand. Colors correspond to potential values.

The surface charge density, σ_s, at z = 0 is

$$\sigma_s = \hat{n} \cdot \|\epsilon_0 \bar{E}\| = \frac{\epsilon_0 v}{G} \tag{3.9}$$

The total charge, Q, on an electrode is

$$Q = d \int_0^d \frac{\epsilon_0 v}{G} dx = \frac{\epsilon_0 v d^2}{G} \tag{3.10}$$

The capacitance, C, is

$$C = \frac{Q}{v} = \frac{\epsilon_0 d^2}{G} \tag{3.11}$$

The capacitance between a single electrode and the hand drops off as one over the distance between the hand and the electrode, as shown in Figure 3-6. For each electrode size, the capacitance drops to approximately 10 percent of its original value when the gap between finger and electrodes increases from 1 to 10 mm. It should be noted that this solution only applies when the point of interest is at least a distance

G from the edge in x.

One concern with capacitive sensing, which is not addressed here, is its sensitivity to water. One of the functional requirements for the proposed sensor system is to function in the presence of rain and water droplets. Since water has a similar dielectric constant to a finger, it has the potential to trigger false touch or hover events. This is a significant concern, which should be addressed should capacitive sensing be explored further.

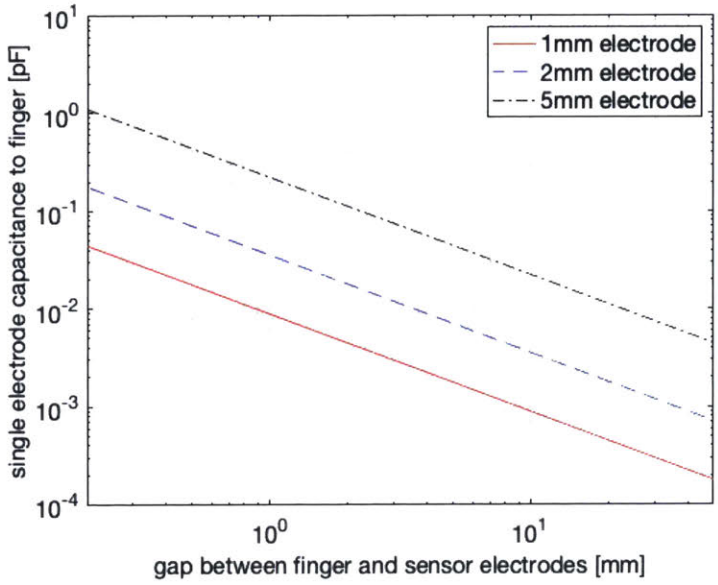

Figure 3-6: Capacitance between a single electrode and the hand for a system with positive electrodes and a negative guard shield. The capacitance drops off with one over the distance between the hand and the electrode.

3.2 Optics

3.2.1 Passive IR Thermal Imaging Through a Metal Grate

One approach to passive sensing of touch and hover is to use thermal imaging to identify a hand or finger above a surface. The human body radiates energy at thermal wavelengths with the highest intensity at a wavelength of approximately 9 micrometers [8], and thermal IR sensors can detect and record this thermal radiation as

Table 3.1: Constant definition for thermal IR calculations.

Symbol	Value	Description
σ	5.670e-8 $\frac{W}{m^2K^4}$	Stefan-Boltzmann Constant
A	0.0025 m^2	Surface Area
ϵ	1	Object Emissivity
T	310 K	Object Temperature
A_2	2.8e-7 m^2	Area of Perforation
G	0.02 m	Distance Between Surfaces
r_{perf}	0.0003 m	Perforation Hole Radius

images. A brief calculation and experiment were performed to assess how the introduction of a metal sheet with small circular perforations above a sensor array would influence its thermal measurements. First, the expected power emitted by a fingertip was calculated. Then, the amount of power expected to be received through a hole in the metal sheet was calculated.

The fingertip is approximated as a cylinder with a radius of 10mm and a length of 30mm. The total power output of the finger can be found as

$$P = \sigma A \epsilon T^4 \tag{3.12}$$

where σ is the Stefan-Boltzmann constant, A is the surface area, ϵ is the emissivity of the object, and T is the temperature of the object. For the case of a finger hovering above the array, the emissivity is near unity for near and far-infrared, so the equation simplifies. The values used for the constants are shown in table 3.1; using these values, the total power emitted is approximately 1.3W.

The view factor from the finger to one perforation in the metal sheet can then be considered to give an estimate of the power received behind each hole. The view factor, F_{12}, is calculated as

$$F_{12} = \frac{A_2}{\pi G^2} \tag{3.13}$$

where G is the distance between two perpendicular surfaces and A_2 is the area of the perforation, as illustrated in Figure 3-7. Using the values listed in table 3.1, the calculation results in an estimated power of approximately 0.3 mW coming through each perforation.

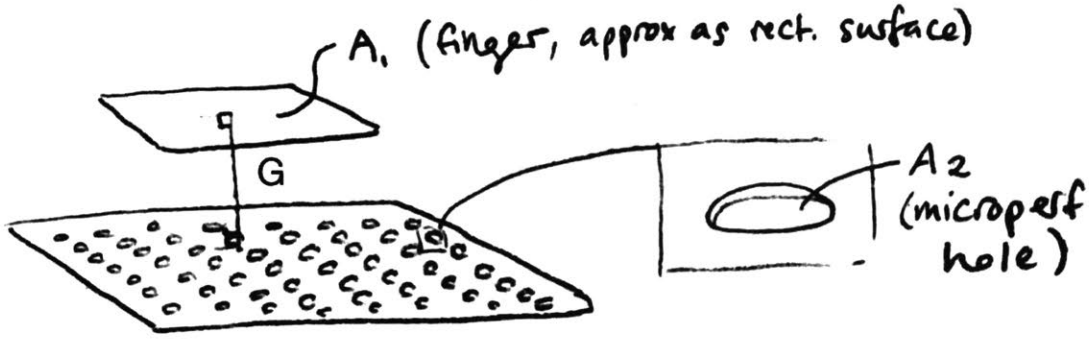

Figure 3-7: Sketch depicting a finger hovering above a thermal sensor array blocked by a perforated metal sheet.

Following this approach, the ratio of the power received by a sensor array covered by a perforated aluminum sheet to the power received by a bare sensor array should correspond to the ratio of the area of the perforations within the sensor array aperture to the area of the sensor array aperture. In order to test this prediction, a brief experiment was performed that compared thermal readings of a finger by a sensor array with a perforated aluminum sheet in front of it, "case 2", to readings by a bare sensor array, "case 1". The experimental setup for the two cases are illustrated in Figure 3-8. The ratio of the signal in case 2 to the signal in case 1 was computed for two configurations: one in which a finger was contacting the surface and one in which a finger was hovering above the surface. The experiment used an Adafruit AMG8833 IR Thermal Camera Breakout, which is capable of measuring temperatures from 0 to 80 degrees Celsius, plus or minus 2.5 degrees, and can detect people up to 7 feet away over a 60 degree viewing angle. A perforated aluminum sheet with thickness of 0.8 mm, hole diameter of 300 microns, and hole spacing of approximately 930 microns was placed over the sensor in case 2.

The anticipated ratio of the sensor reading in case 2 to the reading in case 1

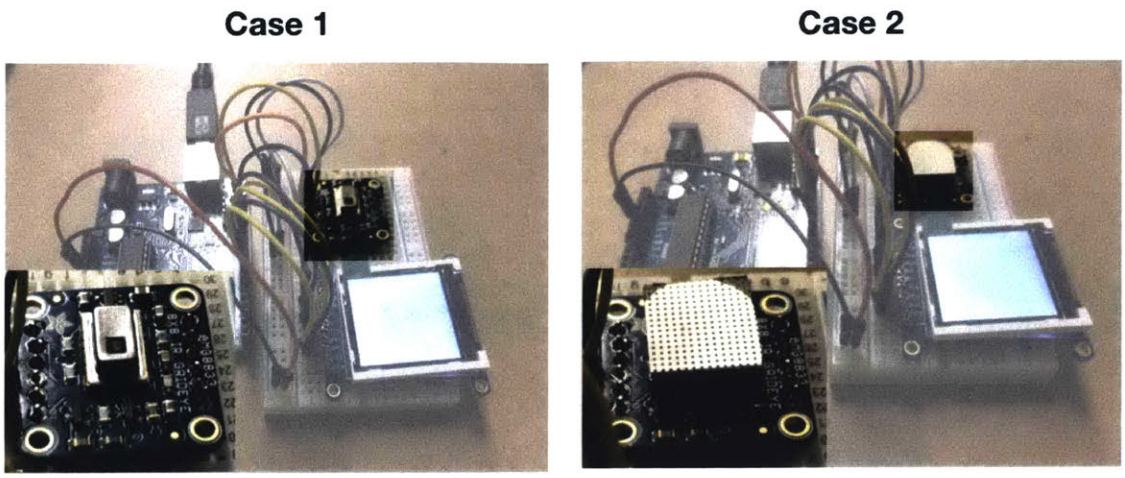

Figure 3-8: Image of the test setup for the exposed sensor (case 1) and covered sensor (case 2).

Table 3.2: Temperature readings in various test configurations.

	Open Air	Hand Hovering	Finger Contacting Surface
Case 2	21.9C (71.5F)	23.5C (74.2F)	28.6C (83.4F)
Case 1	22.8C (73.0F)	29.7C (85.4F)	33.5C (92.3F)

corresponds to the ratio of the area of the perforations within the sensor array aperture to the area of the sensor array aperture, which is approximately 0.09.

The experimental ratio, R_e, is calculated as

$$R_e = \frac{T_{finger,2} - T_{ambient,2}}{T_{finger,1} - T_{ambient,1}} \tag{3.14}$$

where $T_{finger,2}$ is the temperature read in the presence of a finger in case 2, $T_{ambient,2}$ is the temperature read in open air in case 2, $T_{finger,1}$ is the temperature read in the presence of a finger in case 1, and $T_{ambient,1}$ is the temperature read in open air in case 1. The temperatures were taken to be the average temperature detected by the sensor array in the various situations. The temperature readings are recorded in table 3.2.

For the hover case an experimental ratio of 0.22 was observed, and for the touch case a ratio of 0.62 was observed. The discrepancy may be due to heating of the

aluminum sheet by the finger, which was unaccounted for in the calculation. One of the main drawbacks to this approach is that if the sensor were to be used in a wearable device, it may experience large changes in ambient temperature, which would need to be differentiated from the presence of a hand or finger.

3.2.2 Light Field Imaging with an Aluminum Pinhole Array

Studies have shown that integral imaging with camera arrays can be used for gesture recognition through occlusions. Each camera captures a slightly different view of the object, enabling 3D scene reconstruction, and the image can be focused at different depths [37]. Prior art has also demonstrated the use of pinhole camera arrays for depth estimation and touch plus gesture interaction [9]. However, these works focus on thin pinhole cameras, whereas this thesis seeks to create a sensor array that can work through a metal substrate that is also a structural component in a device. As such, it should be at minimum 0.4 mm thick, if it is made from aluminum, to withstand impacts. The functional requirements also dictate a small hole size and small spacing between holes in order to maintain a nondescript appearance.

Therefore, this thesis investigates thick pinhole imaging through aluminum. As a preliminary investigation of this system, calculations were performed to predict the image of a sphere hovering above a surface at various heights using a thin pinhole approximation, and a benchtop experiment was performed to validate the analytical results and test whether the thin pinhole approximation is applicable to a thick pinhole system. The expectation is that the calculations will accurately represent the image geometry but will not capture effects like vignetting that would be caused by the thick walls of the pinhole.

The predicted image was put together using ray casting techniques [19] and considered the system shown in Figure 3-9. Each pinhole in the array has a corresponding sensor array at a distance d_i below it. For each pixel in that array, there is a ray that passes from the pixel through the center of the pinhole to the scene above the surface, where it may intersect the hovering sphere. For simplicity's sake, each pixel is assumed to have only one corresponding ray, which can be represented as a para-

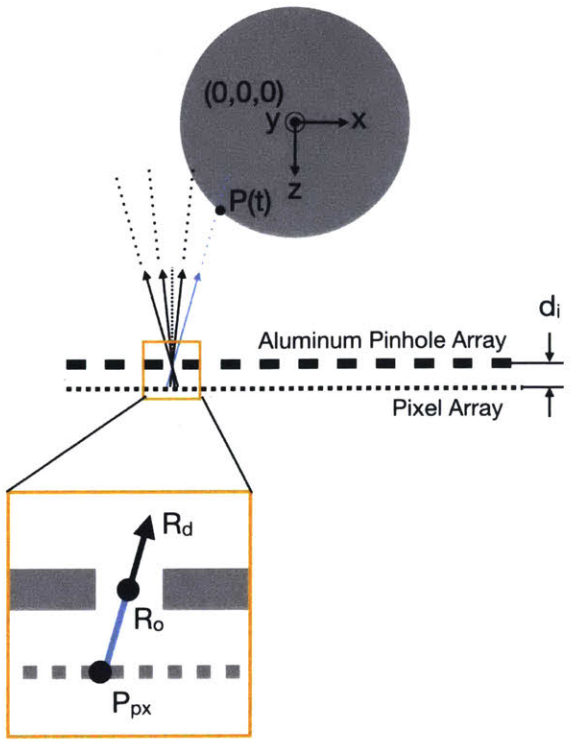

Figure 3-9: Diagram of rays from a single pinhole within a thick pinhole array and their intersection with a hovering sphere.

metric line with origin R_0 at the center of the pinhole and direction R_d determined by the line from P_{px}, the center of the pixel, to R_0. The equation for the line can be written as

$$P(t) = R_0 + R_d t \tag{3.15}$$

The sphere, placed at the origin for ease of calculation, is represented by the following equation:

$$H(P) = P \cdot P - r^2 = 0 \tag{3.16}$$

The point of interest, the intersection of the ray with the sphere, lies at the smallest t, such that $P(t)$ lies on an object in the scene. To find this point on each ray, the ray expression is substituted for P in the sphere equation, and the equation is solved for t. If the result for t is empty, the ray does not intercept the sphere, and a value

of zero is assigned to the corresponding pixel. This step assumes that other objects in the scene are much further away than the sphere and can be neglected in this experiment. If there is a solution for t, the dot product of the sphere surface normal and the normalized ray R_d is taken. The result of the dot product gives a shade value, which is assigned to the pixel under consideration. The procedure is repeated for all pixels in the pinhole array, and the result is plotted in MATLAB for various sphere heights, as shown in Figure 3-10. It should be noted that this model did not account for the lighting in the scene, which could be included in future iterations.

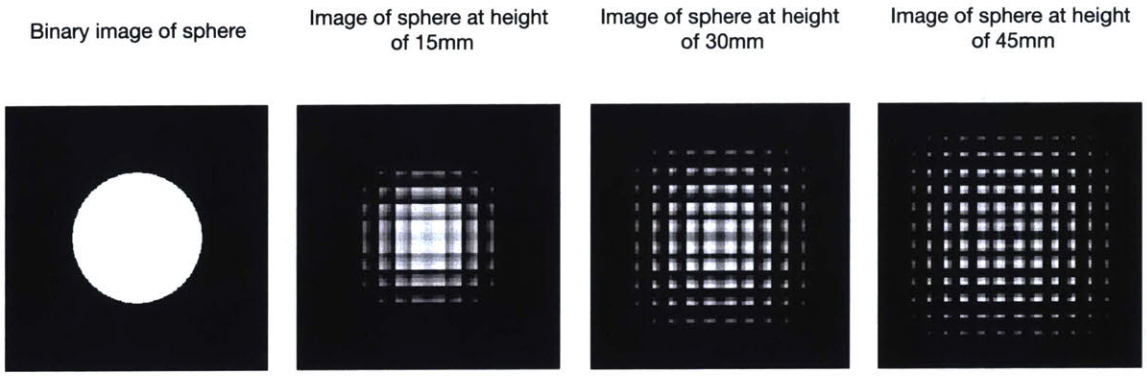

Figure 3-10: Variation in the image of a sphere through a thin pinhole array with object height, which can be used to measure distance to an object.

The pinhole array geometry in the model comes from the array used for the experimental test. The microperforated aluminum sheet is 0.8 mm thick and has holes that are 300 microns in diameter. A benchtop experiment was set up in order to validate the predicted images using a section of the microperforated sheet. The sheet was mounted in a 3D printed fixture which held it above a CMOS sensor (OV2640 with breakout board and shield). This assembly was mounted in a mill, and a metal sphere with diameter of 9.52 mm was mounted in the chuck. Since the CMOS array did not cover the full field of view of all pinholes in the array, the housing was designed to block the light from all but one pinhole, and the assembly was moved using the mill stage in increments of 1.75 mm in order to approximate a full pinhole array. Additionally, a white backdrop was added to the sphere, and the sphere was illuminated from below in order to boost contrast between the object and the background. The test set-up

is shown in Figure 3-11.

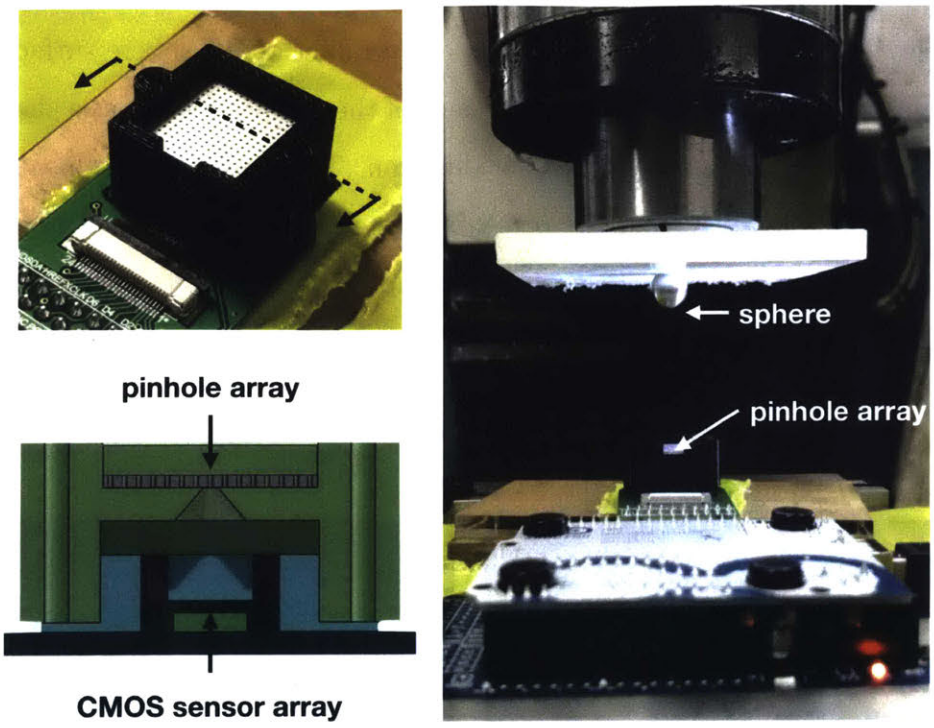

Figure 3-11: Experimental pinhole set-up, with a microperforated aluminum sheet mounted above a CMOS array.

The results from the experiment are compared to the MATLAB model, with colors inverted, in Figure 3-12. There is some difference between the geometry of the simulated and experimental images, which may be explained by imprecision in the placement of the array in the experimental set-up. Only one quarter of the array was imaged, as the image should be symmetric, and that quarter was mirrored to fill in the remainder of the image. Another experiment with an alignment fixture for the pinhole array and a full scan of the surface could be performed to check the discrepancy is due to physical misalignment.

There is also vignetting around the edges of the images from the experimental setup, which is characteristic of pinhole cameras as the thickness of the substrate approaches or exceeds the hole diameter and the hole begins to act as both the aperture and the field stop. It occurs because the hole has a smaller effective area to let in light for the edge pixels than it does for the central pixels. When viewed head

on, it appears to be a circle; when viewed from an angle, it appears to be an ellipse with the same major diameter as the circle. This vignetting could be compensated for computationally.

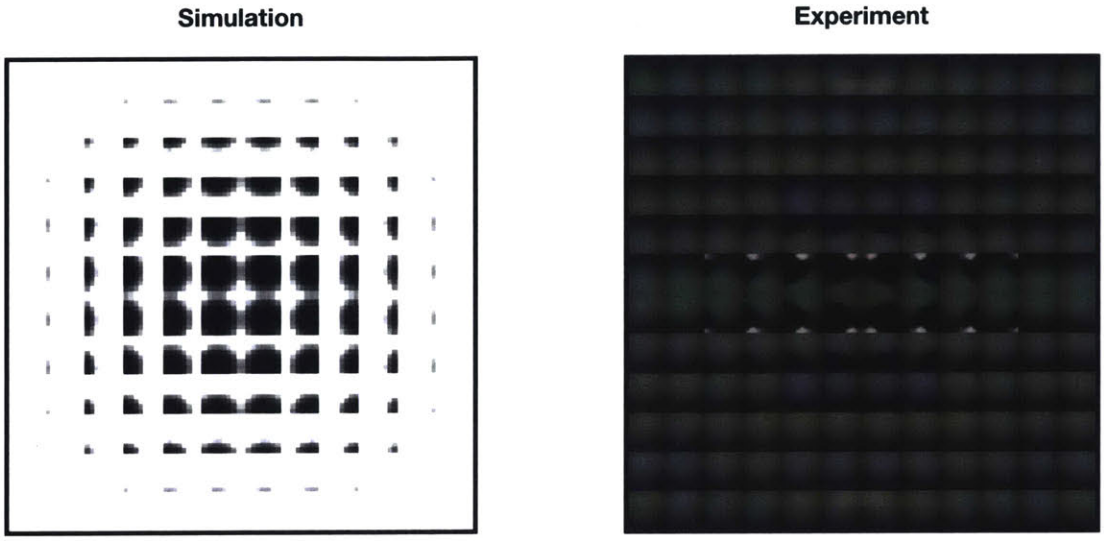

Figure 3-12: Results from the MATLAB model and experiment showing the image of a sphere at a height of 40 mm above the substrate surface.

Despite these features, the results indicate that the thin pinhole approximation can give an adequate estimate for the image that will result from a thick pinhole array. As such, once can apply optical design guides used for traditional pinhole imaging, like those described by Hirsch et al. [9] and repeated below. This approach effectively describes the behavior of the pinhole as the aperture of the system. The variables used in the following equations are depicted in Figure 3-13.

The width of the optical point spread function (PSF), b, which describes the spread of a point source through an optical system, is

$$b = \frac{2.44\lambda d_i}{a} + \frac{a(d_o + d_i)}{d_o} \tag{3.17}$$

The field of view, α, is shown in Figure 3-13 and is defined as

$$\alpha = 2\arctan(\frac{a}{h}) \tag{3.18}$$

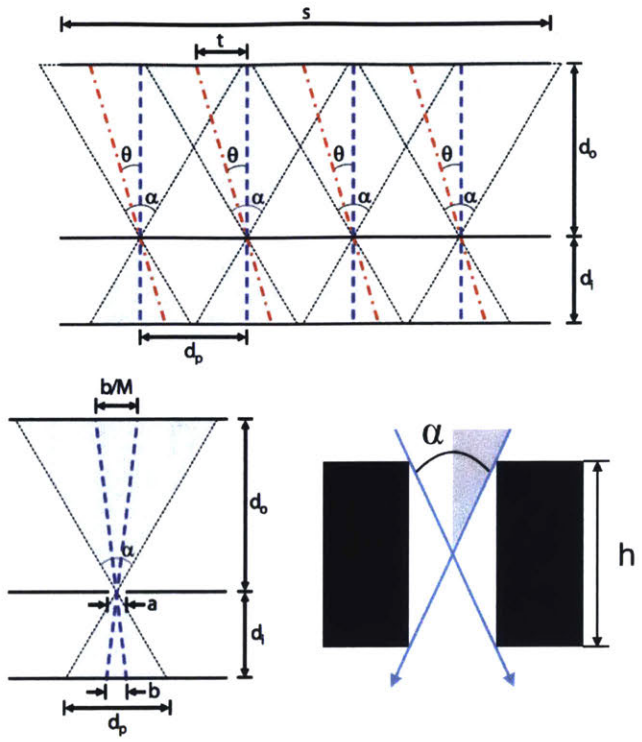

Figure 3-13: Pinhole array geometry [9] and thick pinhole field of view. d_0 is the distance from the object to the pinholes, d_i is the distance from the pinholes to the sensor, s is the width of the object being imaged, θ is the viewing angle, a is the pinhole diameter, b is the optical PSF width, M is the magnification, h is the pinhole thickness, α is the field of view, and d_p is the minimum pinhole spacing, which is also the pinhole image width. The values used for calculations are shown in Table 3.3.

The minimum pinhole spacing to prevent neighboring images from overlapping is dependent on the PSF and field of view, as follows:

$$d_p = 2d_i \tan(\frac{\alpha}{2}) + b \tag{3.19}$$

The number of orthographic views obtained by the system is

$$N_{angular} = \frac{d_p}{b} \tag{3.20}$$

The number of independent spatial samples is

$$N_{spatial} = min(\frac{s}{d_p}, \frac{d_i s}{d_o b}) \tag{3.21}$$

Table 3.3: Constant definition for pinhole calculations.

Symbol	Value	Description
λ	550 nm	Wavelength
d_0	0.4:100 mm	Distance from Object to Pinholes
d_i	8.2 mm	Distance from Pinholes to Sensor
a	0.3 mm	Pinhole Diameter
h	0.8 mm	Pinhole Thickness
s	14 mm	Width of Object Imaged

The magnification is

$$M = \frac{d_i}{d_o} \tag{3.22}$$

Figure 3-14 explores how some of these features change as an object moves above the pinhole array. The wavelength is assumed to be the peak wavelength produced by daylight, approximately 550 nm. Unless the light is filtered, there will be some chromatic aberrations. The constant values used for the calculations are shown in table 3.3. The minimum object distance is set to half the thickness of the pinhole array. The angular views reach 90% of their final value around 36mm, and the number of spatial views reaches 90% of the end value much more quickly, at around 3mm.

Some of the benefits of pinhole imaging include ease of manufacture and long sensing range. The main limitation in pursuing a pinhole design is that the system has a low sensitivity to light compared with other optical methods, as the pinhole substrate blocks most of the light from reaching the sensor array. This is evident in Figure 3-12. There are a number of approaches to take to mitigate this problem, including increasing the diameter of the pinholes, exploring more sensitive CMOS arrays, adding active visible or IR lighting, and increasing exposure time (though this would also increase latency). An additional concern is that surface contaminants could block the holes and interfere with imaging. A countermeasure to this would be to backfill the holes with a clear epoxy, which would make the surface easier to clean.

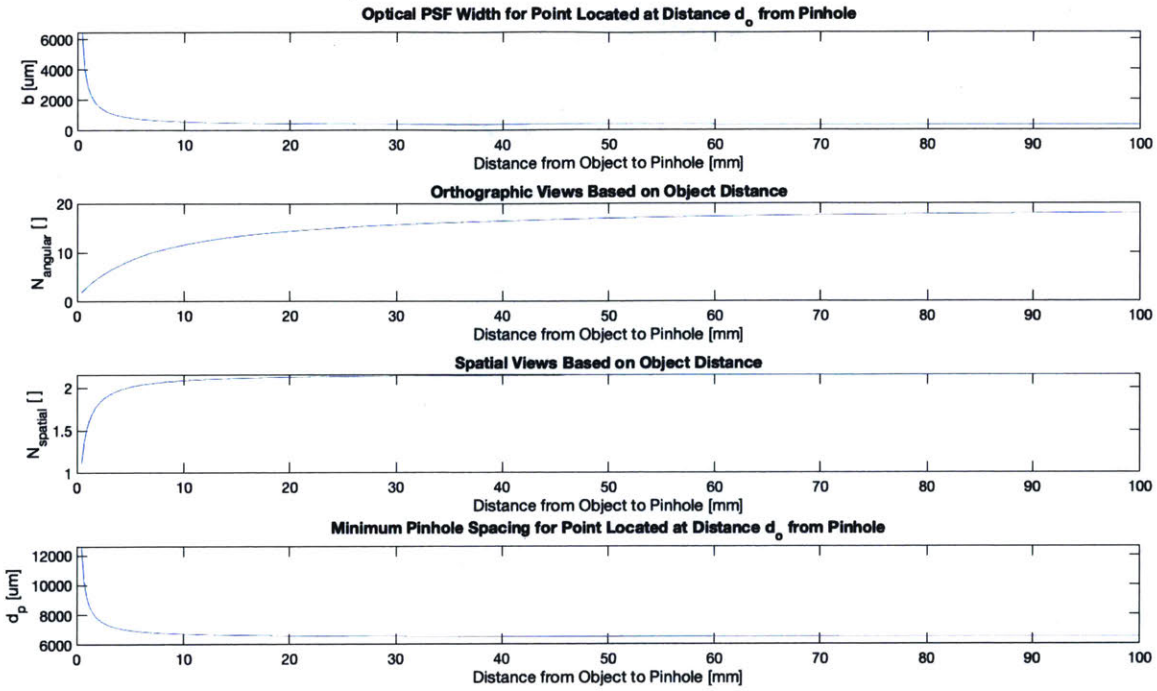

Figure 3-14: Change in PSF, number of orthographic and spatial views, and minimum pinhole spacing with varying object distance.

However, this interface would not be very robust; as it ages, scratches could cause clouding of the surface, degrading the image.

3.3 Acoustics

3.3.1 Pulse Echo Time of Flight Through a Metal Barrier

Ultrasonic waves have much less difficulty than electromagnetic waves at passing through a metal barrier. As such, one approach to sensing hover with acoustic methods might be to place a metal membrane in front of a traditional sensor array, as shown in Figure 3-15. Some of the outgoing wave would be reflected by the boundary and picked up by the receiver quickly, and another part would continue through the barrier and be reflected off of nearby objects. The first signal would occur at a known time and could be ignored, and the latter signal processed as a gesture input. The transmission loss caused by the introduction of a metal membrane is calculated below. The system considered includes air on both sides of the membrane to give

an estimate of the worst-case transmission loss. The situation could be improved by including coupling layers.

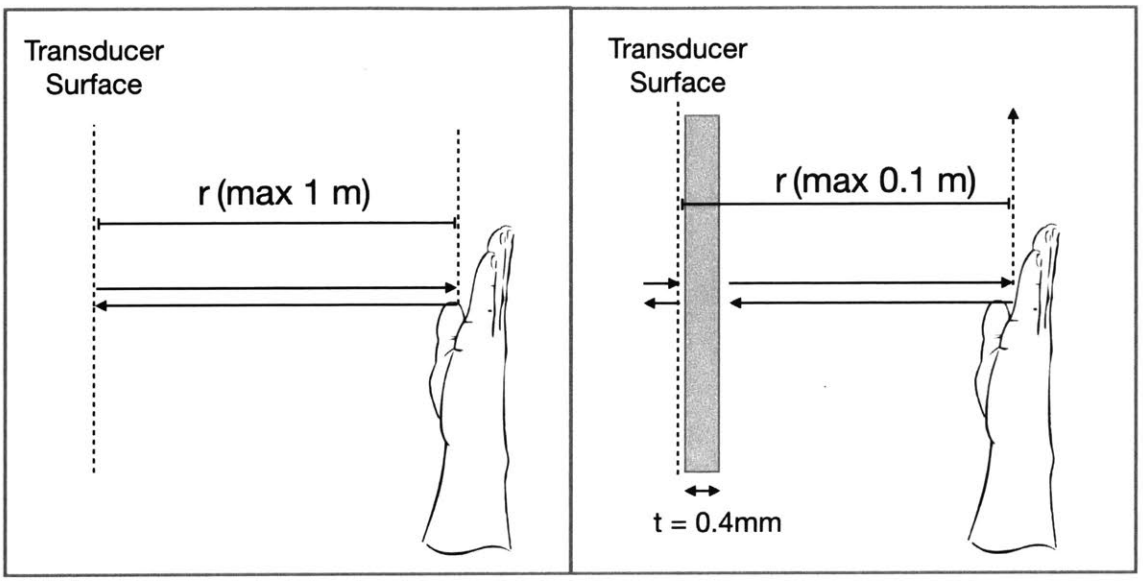

Figure 3-15: Hover detection system, with and without metal barrier.

Transmission loss through a wall can be calculated as [25]:

$$10\log_{10}\left(\frac{4\rho_0^2 c_0^2}{4\rho_0^2 c_0^2 + \omega^2 m^2}\right) \tag{3.23}$$

where $\rho_0 c_0$ is the acoustic impedance of the surrounding medium (in this case air), ω is the frequency of the acoustic signal in radians/s, and m is the wall mass per unit area. Transmission loss due to propagation through free space can be calculated as

$$10\log_{10}\left(\frac{r^2}{r_{ref}^2}\right) \tag{3.24}$$

where r_{ref} is the reference distance and r is the distance of the point of interest from the source. Transmission loss due to reflection off of the finger can be found as

$$10\log_{10}\frac{(\rho_1 c_1 - \rho_0 c_0)^2}{(\rho_1 c_1 + \rho_0 c_0)^2} \tag{3.25}$$

where $\rho_0 c_0$ is the acoustic impedance of air and $\rho_1 c_1$ is the acoustic impedance of the finger, which is assumed to be equal to the acoustic impedance of skin. The above

equations refer to attenuation of acoustic intensity, $I = \frac{|p|^2}{\rho_0 c} = \frac{W}{4\pi r^2}$ for an omnidirectional point source, where p is pressure and W is power. The total transmission loss for the system with the metal barrier can be written as

$$2 * 10\log_{10}(\frac{4\rho_0^2 c_0^2}{4\rho_0^2 c_0^2 + \omega^2 m^2}) - 2 * 10\log_{10}(\frac{r^2}{r_{ref}^2}) + 10\log_{10}\frac{(\rho_1 c_1 - \rho_0 c_0)^2}{(\rho_1 c_1 + \rho_0 c_0)^2} \tag{3.26}$$

The total transmission loss for the system with no barrier can be written as

$$-2 * 10\log_{10}(\frac{r^2}{r_{ref}^2}) + 10\log_{10}\frac{(\rho_1 c_1 - \rho_0 c_0)^2}{(\rho_1 c_1 + \rho_0 c_0)^2} \tag{3.27}$$

Expressions 3.26 and 3.27 can be translated to a scaling factor relating the output intensity, I_{out}, to the input intensity, I_0, using equation 3.28.

$$ScalingFactor = 10^{\frac{TransmissionLoss[dB]}{10}} \tag{3.28}$$

The received acoustic intensity for the system with the metal barrier can then be written as

$$I_{out,barrier} = \frac{16\rho_0^4 c_0^4 r_{ref}^4 (\rho_1 c_1 - \rho_0 c_0)^2}{(4\rho_0^2 c_0^2 + \omega^2 m^2)^2 r^4 (\rho_1 c_1 + \rho_0 c_0)^2} I_0 \tag{3.29}$$

The received acoustic intensity for the system with no barrier would be

$$I_{out,free} = \frac{r_{ref}^4 (\rho_1 c_1 - \rho_0 c_0)^2}{r^4 (\rho_1 c_1 + \rho_0 c_0)^2} I_0. \tag{3.30}$$

The ratio of the power received in the system with the metal barrier to the power received in the system with no barrier is $I_{out,barrier}/I_{out,free}$.

Assuming the dimensions shown in the figure and the constant variables given in Table 3.4 the final intensity for the system with no barrier would be orders of magnitude higher than that of the system with the barrier. Since intensity is directly proportional to power, assuming the transducers can be operated at higher voltages than they currently are, the system with the wall would need orders of magnitude more power to achieve similar operation. The situation could be improved by coupling

Table 3.4: Constant definition for acoustic calculations.

$\rho_0 c_0(air)$	408 $\frac{kg}{m^2 s}$
$\rho_1 c_1(skin)$	1.99e6 $\frac{kg}{m^2 s}$
ρ_{Al}	2700 $\frac{kg}{m^3}$
m	ρ_{Al}t
f	40 kHz
r_{ref}	0.03 m

the transducers to the wall and adding matching layers to the far side of the wall to reduce the impedance mismatch between the air and the metal. However, it would be preferable to remove the mismatch altogether. This could be done by building the ultrasonic transducers into the wall, such that the wall becomes the vibrating membrane of the transducer. Such systems have been explored previously for both air and water-coupled systems [30] [12] and are discussed further in chapter 4.

3.4 Sensing Modality Selection

Based on the literature review and on the preliminary investigations described above, a comparison of sensing modalities in terms of sensing range, power requirements, substrate flexibility, sensitivity to lighting conditions, and manufacturability was put together in order to determine which modality to continue exploring. The power requirements of selected systems in literature are presented in Table 3.5 for context. The modality comparison is summarized in Table 3.6.

Acoustic sensors were chosen as the most promising option to pursue. Capacitive approaches are unlikely to meet the desired sensing range in a small form factor, as the range is limited by sensor size. They also are unlikely to work as intended in the presence of water, which has a similar dielectric constant to a person's hand. The pinhole camera approach is likely to be highly sensitive to lighting conditions and to surface contaminants. The images of the sphere in section 3.2 were already quite dark, and adding active illumination would drive up power requirements. The risk

Table 3.5: Estimated power requirements of various sensing modalities from [28], [20], [4], [26], [32], and [24] (left to right).

Acoustic	**Electromagnetic**	**Optical**		
Active	**Capacitive**	**IR**		**Visible**
Pulse-Echo		**Pulse-Echo**	**Thermal**	**Light Field**
400 µW (active) for PMUT designs	< 300 µW (active)	20 mW (active) 0.3 mW (stand-by)	22.5 mW (active) 4 mW (stand-by)	140 mW (active) 2 mW (stand-by) Per Pixel: 84 pW (active)

* Estimations based on literature & preliminary experiments

Table 3.6: Comparison of sensing modalities in terms of factors of interest. Green represents "Low Risk", yellow represents "Moderate Risk", and red represents "High Risk".

	Acoustic	Electromagnetic	Optical
Sensing Range	Potentially 100mm	Limited by Sensor Size	Feasibly 100mm
Power Requirements	Moderate Power	Low Power	Moderate-High Power
Substrate Flexibility	Potential to Work Through Desired Substrates	Electrodes Would Form Majority of Surface	Material Needs Perforations for Pinhole Approach
Sensitivity to Lighting Conditions	Not Sensitive	Not Sensitive	Sensitive
Manufacturability	Potentially Difficult to Implement in Small Form Factor	Easy to Manufacture	Fairly Easy to Manufacture

of contaminants blocking the pinholes could be reduced by using a filler material, but this could wear over time, leading to image degradation. Thermal camera approaches would be highly sensitive to ambient temperature. By comparison, acoustic methods don't have any factors that stand out as particularly risky. PMUT designs have demonstrated their ability to meet the desired sensing range and maintain low power requirements. Flexural ultrasonic transducers may lead to lower sensing range and higher power requirements by comparison, but their work in other applications suggests these limitations will not be prohibitive. Flexural transducers may lead to a larger than ideal form factor, but should still fall within the functional requirements.

Additionally, this type of acoustic sensing is the only strategy considered that could potentially work through a solid metal substrate, which is most in line with the goal of this research to increase the options for materials and form factors in interaction design.

Chapter 4

Flexural Ultrasonic Transducers

4.1 Prior Art

In the past few years, there has been work published on mesoscale flexural ultrasonic transducer arrays. Savoia *et al.* from Universita Degli Studi Roma Tre present a low frequency broadband flextensional ultrasonic transducer array for use in a variety of water-coupled applications, including traditional sonar applications as well as biomedical applications, such as transdermal drug delivery and treatment of wounds. The authors present a transducer array constructed of a number of circular cells with piezoceramic disks and a steel sheet forming the vibrating elements and FR-4 laminates and brass forming the walls and backing. This construction forms an array of piezo unimorph transducers and results in a lighter and more compact design than the commonly used thickness-mode piezoelectric transducers, which is beneficial in applications where portability and easy use are important [30]. Kang *et al.* from the University of Warwick present a similarly constructed flexural ultrasonic phased array that is designed for gas flow measurement. This array is composed of a titanium membrane with piezoceramic disks adhered to it, a steel baffle that defines the walls, and a steel back plate [12]. To the author's knowledge, no groups as of yet have published work applying mesoscale flexural ultrasonic transducers to gesture sensing. These transducers have the potential to enable a more seamless incorporation of sensing capabilities into consumer products. The remainder of this thesis aims to

evaluate their application to touch and hover sensing.

4.1.1 System Overview

The transducer array under consideration here is made up of a sheet of steel with nine flat bottom holes on the underside that create locally thin sections referred to as membranes. An axially polarized piezoceramic disk is bonded to the underside of each membrane, and a steel back plate is bonded to the bottom surface of the assembly. When a voltage is applied across the piezoceramic disk, it expands or contracts, forcing the membrane to bend. This construction forms an array of piezo unimorph transducers.

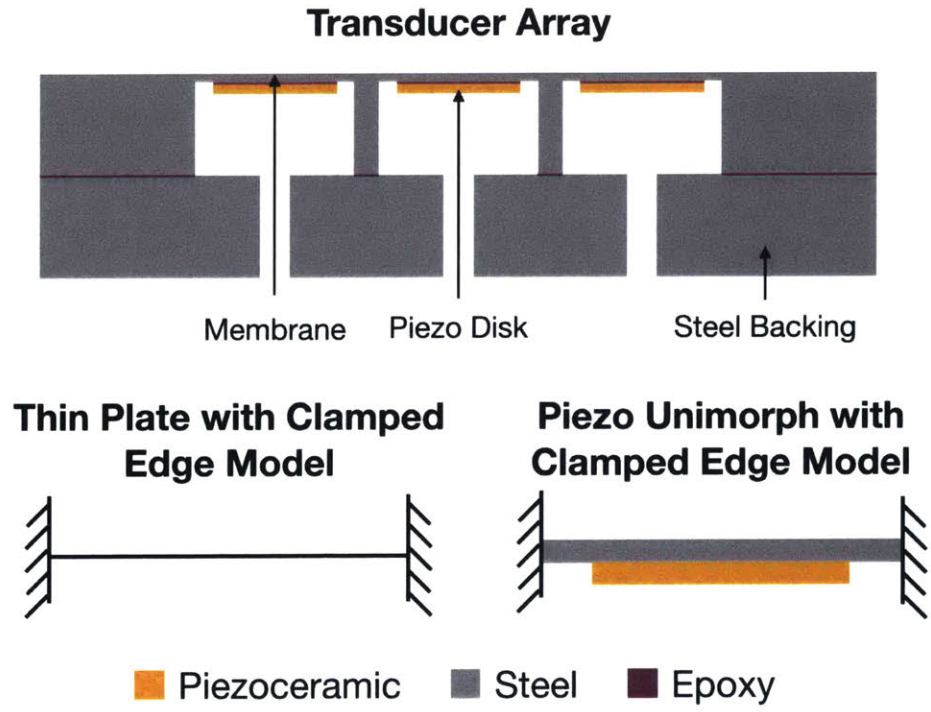

Figure 4-1: Cross section of transducer array, thin plate with clamped edges model for a single transducer, and perfectly bonded piezo unimorph with clamped edges model for a single transducer.

For the purpose of analytical modeling, each transducer is considered individually and two simplified transducer models are used. When estimating mode shapes and natural frequency, the transducer is modeled as a thin vibrating plate with clamped

edges. When calculating deflection due to voltage loading and voltage due to pressure loading, the transducer is modeled as a cylindrical membrane with clamped edges and a piezo disk perfectly bonded to it. The perfect bonding assumption means the adjacent membrane and piezo disk surfaces will have matching displacements. Cross sections of the full array along with the two simplified individual transducer models are shown in Figure 4-1.

4.1.2 Hover Detection Strategy

When operated in hover mode, one transducer in the array is operated as a transmitter, and the other transducers act as receivers. The transmitter is driven near its resonant frequency and the vibrating plate displaces the air above the surface, sending a pressure wave into the space above the device. If an object, like a hand, is placed in the path of the pressure wave, it will reflect the wave back toward the surface of the array where it can be picked up by the receivers. The incoming pressure causes displacement of the receiver membranes, which generates voltages across the receiver piezos. Multiple transducers can also be used as transmitters, which is discussed in future work, but for chapters 4 and 5 the case of a single transmitter is considered. This system is illustrated in figure 4-2.

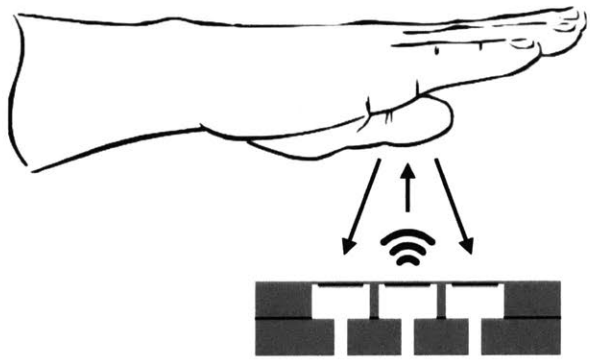

Figure 4-2: Illustration of the array detecting a hand in hover mode. Image is not to scale.

There are several ways to get information about hover gestures using this configuration. The distance of the hand from a receiver can be obtained using pulse

echo time of flight measurements. The position of the hand can be obtained through triangulation using the distances from multiple receivers. The velocity of the hand can be calculated using the Doppler shift. Finally, information about the frequency response of the system can be collected either using a frequency sweep or by inputting a stochastic binary signal and taking the input-output cross correlation over the input auto-correlation; the second approach is demonstrated in Appendix A. Gestures can be defined in terms of some subset of the above information.

4.1.3 Touch Detection Strategy

When operated in touch mode, all transducers in the array are excited by an AC voltage near their resonant frequency and the current draw is monitored by measuring the voltage across a sense resistor in series with the piezo. At resonance, the piezo is most willing to give and receive current, so the voltage drop across the resistor is relatively large. When an object, like a finger, comes into contact with the transducer surface, it adds damping to the system and changes the loading conditions, resulting in a drop in the measured voltage. A threshold can be set, below which a touch event will be declared. The location of the finger can be be determined based on which transducer responses in the array are damped. This configuration is illustrated in the following figure.

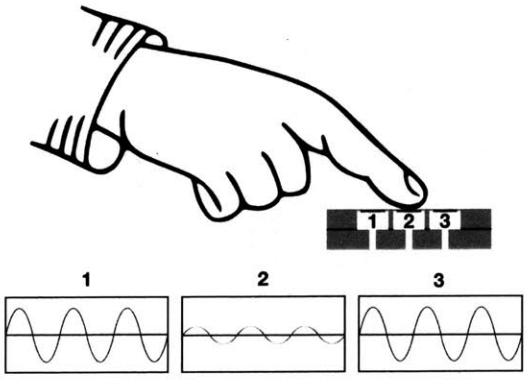

Figure 4-3: Illustration of the array detecting a hand in touch mode. Image is not to scale.

4.2 Design and Modeling

This section presents an analytical model for an individual transducer, focusing on the physics relevant to hover applications as they have more steps to model. The section is divided into the following subsections:

- Natural frequency and mode shapes of a vibrating plate
- Deflection of a piezo unimorph under voltage loading
- Acoustic pressure output
- Geometry optimization for maximum deflection
- Acoustic wave propagation in a hover detection system
- Voltage generation in a piezo unimorph under pressure loading
- Amplification factor at resonance

The steps mostly sequentially follow the path a signal would take through the system. First, a voltage is applied to deflect the membrane. Next, the deflection displaces air and generates a pressure wave. Then the pressure wave travels through the air and is reflected back toward the transducer by a hovering object. Finally, that pressure wave deforms the membrane and generates a voltage across the piezo disk. These sections are all calculated for a static voltage case.

There are three sections which are not steps in this path. One section identifies the mode shape that is most suited to hover applications and calculates the resonant frequency at which the transducer should be operated. Another looks at optimizing geometry to achieve the greatest deflection and, as they are directly related, the greatest output pressure. Finally, a third section explores the amplification factor, which links the static analysis to dynamic operation at resonance.

The values used for the constants described in this section can be found in Appendix G.

4.2.1 Natural Frequency and Mode Shapes of a Vibrating Plate

In order to maximize the sound output and the sensitivity of the transducer, it should be operated at or near its resonant frequency, where the amplitude of oscillation is large. In order to determine which frequency it should be operated at, the first steps are to model the deflection profiles of various resonant modes of the transducer membrane and to determine the frequencies at which they occur. To find this information, the transducers are approximated as thin vibrating plates with clamped edges. This assumption holds provided the ratio of the membrane thickness to diameter is low enough and the surrounding structure is considerably stiffer than the membrane. In each case, an order of magnitude is considered sufficient.

The calculation of the mode shapes can be described using Bessel functions, as detailed by Katie Smyth and repeated below [31]. The modal shape function describing deflection as a function of distance from the transducer center is

$$W(r) = A(J_0(\gamma_{mn}r) - \frac{J_0(\gamma_{mn}a)}{I_0(\gamma_{mn}a)}I_0(\gamma_{mn}r)) \tag{4.1}$$

Where A is a scaling constant that depends upon energy input to the system and system damping properties, a is the plate radius, r is the distance of a given point from the center of the plate, J_0 is the Bessel function of order zero of the first kind, I_0 is the modified Bessel function of order zero of the first kind, and γ_{mn} is a constant that depends on the vibration mode shape (m,n), where m refers to the number of modal circles and n refers to the number of modal diameters. γ_{mn} is defined in relation to β_{mn}, another constant related to the vibration mode shape, as

$$\gamma_{mn} = \frac{\pi}{a}\beta_{mn} \tag{4.2}$$

β_{mn} is defined as

$$\beta_{mn} = \frac{\sqrt{\lambda^2}}{\pi} \tag{4.3}$$

where λ^2 is equal to 10.2158 for mode (0,0), 39.771 for mode (1,0), and 89.104 for mode (2,0) [16]. The normalized plate deflection profiles for the first three axisymmetric vibration modes are plotted in figure 4-4. The first axisymmetric mode is most

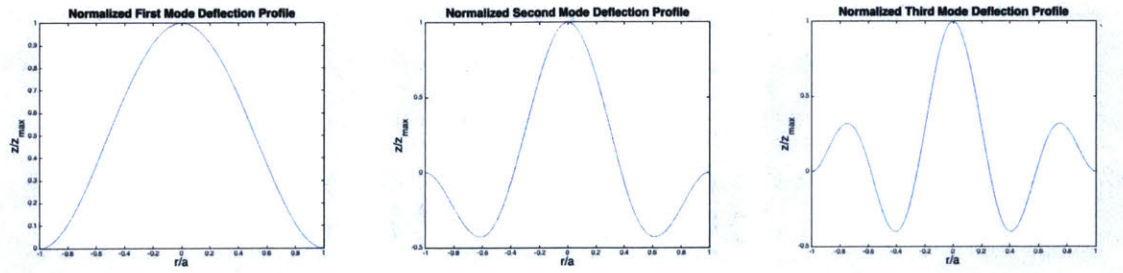

Figure 4-4: Normalized plate deflection profiles for the first three axisymmetric vibration modes of a clamped-edge plate. The first mode is most advantageous for an ultrasonic transducer.

advantageous in an ultrasonic transducer, as the simultaneous positive and negative deflection in higher modes can create destructive interference, which decreases acoustic output. The resonant frequency for the first axisymmetric mode of the plate, with $(m, n) = (0, 0)$, can be calculated as

$$f = \frac{\pi}{2a^2}\sqrt{\frac{D}{I0}\beta_{00}^2} \tag{4.4}$$

where $I0$ is the mass moment of inertia, defined as

$$I0 = \rho h \tag{4.5}$$

where ρ is the density of the membrane substrate and h is the thickness of the membrane, and D is the bending stiffness of the membrane, defined as

$$D = \frac{Qh^3}{12} \tag{4.6}$$

Q is the axial elastic stiffness coefficient

$$Q = \frac{Y}{1 - \nu^2} \tag{4.7}$$

where Y is the Young's modulus of the membrane and ν is the Poisson's ratio of the membrane. The transducers will be operated at or near the resonant frequency associated with their first axisymmetric mode for the prototypes presented in this thesis.

Since the construction of the array, shown in section 4.1.1, creates an air cavity with a narrow opening behind the transducer membrane, the Helmholtz resonance of this feature was also calculated, to ensure it would not overlap with the resonant frequency of the membrane. The Helmholtz frequency is

$$f_{Helmholtz} = \frac{c}{2\pi}\sqrt{\frac{A_o}{V_c l}} \tag{4.8}$$

where A_o is the area of the opening, V_c is the volume of the cavity, l is the length of the opening, and c is the sound speed in air. For the prototypes included in this chapter, the Helmholtz resonance is about an order of magnitude less than the membrane resonant frequency.

4.2.2 Deflection of a Piezo Unimorph Under Voltage Loading

The previous section gives the deflection profile, but in order to model the absolute deflection of the transducer membrane, the constant A must be determined. A varies based on the operating frequency. For DC operation, A is equal to the peak static deflection. For operation at resonance, A is the product of the peak static deflection and an amplification factor, A_r, which depends on the damping characteristics of the system. Mo et al. describe the static deflection of a unimorph circular piezoelectric actuator under voltage loading for transducers in which the diameter of the piezoceramic disk is smaller than the diameter of the transducer membrane. [22] The system analyzed is shown in Figure 4-5, and the authors' solution for deflection is summarized below.

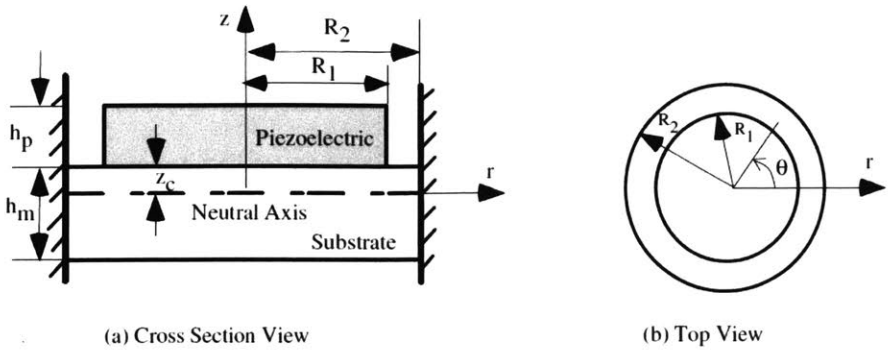

Figure 4-5: Partially covered piezoelectric circular plate [22]. The transducer membrane is labeled as substrate in this image.

The transverse deflection of the transducer, w, is given by [22]:

$$w(r) = \begin{cases} \frac{C_5\{2R_1^2 \ln(\frac{R_1}{R_2}) + [1-(\frac{R_1}{R_2})^2]r^2\}V}{C_6 - C_7(\frac{R_1}{R_2})^2 + \frac{1}{2}h_p^4 S_m^2(1+\nu)(\frac{R_1}{R_2})^4}, & \text{if } r \leq \mathrm{R}_1 \\ \frac{C_5\{2R_1^2 \ln(r) - R_1^2[2\ln(R_2)-1] - (\frac{R_1}{R_2})^2 r^2\}V}{C_6 - C_7(\frac{R_1}{R_2})^2 + \frac{1}{2}h_p^4 S_m^2(1+\nu)(\frac{R_1}{R_2})^4}, & \text{if } R_1 < r \leq \mathrm{R}_2 \end{cases} \tag{4.9}$$

where

$$C_5 = 3d_{31}h_m S_{11}^E S_m(h_m + h_p), \tag{4.10}$$

$$C_6 = 4S_{11}^E h_p h_m^3 S_m + 6S_{11}^E h_m^2 h_p^2 S_m + 4S_{11}^E h_m h_p^3 S_m + \frac{1}{2}h_p^4 S_m^2(1+\nu) + \frac{2h_m^4 {S_{11}^E}^2}{1+\nu} \tag{4.11}$$

and

$$C_7 = 4S_{11}^E h_p h_m^3 S_m + 6S_{11}^E h_m^2 h_p^2 S_m + 4S_{11}^E h_m h_p^3 S_m + h_p^4 S_m^2(1+\nu) \tag{4.12}$$

V is the voltage applied across the piezo disk, S_m is the elastic compliance constant of the membrane, ν is the Poisson's ratio of the piezo disk, d_{31} is the piezoelectric constant, and S_{11}^E is the elastic compliance constant for the piezoceramic.

In order to get the scaling factor for the static case, the expression can be evaluated

at $r = 0$. The amplification factor, A_r, is difficult to model analytically, so for now it will be represented symbolically, and it will be explored further in section 4.2.7 and measured experimentally.

4.2.3 Acoustic Pressure Output

The acoustic pressure output can be found from the deflection profile, as described by Smyth [31]. When transmitting, the transducer acts as a boundary surface for acoustic wave radiation.

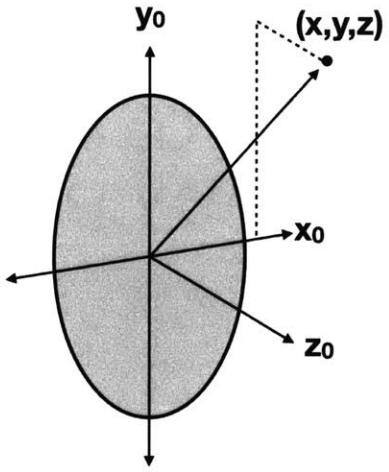

Figure 4-6: Illustration of the transducer centered on the plane $z_0 = 0$ and a point (x, y, z) above the surface.

The pressure at a given point (x, y, z) above the surface of the transducer can be expressed in terms of Green's function for a rigid boundary and the velocity along the surface of the transducer $(x_0, y_0, 0)$ as

$$p_w(x, y, z) = jk\rho_m c_m \iint (u_w(x_0, y_0) G_w(x, y, z|x_0, y_0, 0)) dx_0 dy_0 \tag{4.13}$$

where k is the wavenumber, defined as $\frac{2\pi f}{c_m}$, f is the frequency calculated in the previous section, c_m is the sound speed in air, and ρ_m is the density of air. The velocity profile is the time derivative of the axial deflection profile, calculated in

section 4.2.1. The amplitude of the velocity can be expressed as:

$$u_w = j\omega A[J_0(\gamma r) - \frac{J_0(\gamma a)}{I_0(\gamma a)} I_0(\gamma r)] \tag{4.14}$$

where ω is equal to $2\pi f$ and r can be expressed in cartesian coordinates as $r = \sqrt{x_0^2 + y_0^2}$ when plugged into the expression for pressure. The Green's function for a rigid boundary is defined as:

$$G_w(R|R_0) = \frac{1}{4\pi L} e^{ikL} + \frac{1}{4\pi L'} e^{ikL'} \tag{4.15}$$

where

$$L = \sqrt{(x - x_0)^2 + (y - y_0)^2 + (z - z_0)^2} \tag{4.16}$$

$$L' = \sqrt{(x - x_0)^2 + (y - y_0)^2 + (z + z_0)^2} \tag{4.17}$$

The pressure at a point above the transducer surface is fully defined by equations 4.13 through 4.17, with the exception of the parameter A, which has yet to be experimentally determined.

4.2.4 Geometry Optimization for Maximum Deflection

In order to achieve a greater range or reduced power consumption, the acoustic pressure output of the transducer should be maximized. Given that pressure output is directly related to deflection, this next section seeks to optimize the transducer construction in order to maximize deflection. In order to make use of readily available piezoelectric materials and accessible membrane materials, this section explores how changes in geometric parameters, specifically the ratio of the piezoelectric disk radius to the membrane radius and the ratio of the height of the piezoelectric disk to the height of the membrane, affect deflection.

The static deflection was first calculated as in section 4.2.2, and then a simulation was performed using COMSOL Multiphysics and compared to the analytical solution.

The piezoelectric material was chosen to be lead zirconate titanate (PZT-5H), which is available as a material in COMSOL. The membrane material was chosen to be aluminum. It should be noted that this same procedure can be followed for other materials, and aluminum is chosen as an example. The thickness of the membrane was fixed at 0.5mm and the radius of the membrane was fixed at 5mm. The thickness of the membrane is limited to about 0.4 to 0.5mm in aluminum to be easily machinable and survive impact loading. Once the thickness is set, the diameter is chosen to ensure the resonant frequency remains in the desired range of approximately 30 to 50kHz, which is inaudible and can be produced by standard microcontrollers. The thickness, h_p, and radius, R_1, of the piezo disk were then defined as the product of some constant and the membrane thickness, h_m, or radius, R_2. The constant was varied between 0 and 1.2 for the thickness and between 0 and 1 for the radius, and the center displacement of the transducer was computed for each variation with 1V loading. The results are shown in Figure 4-7.

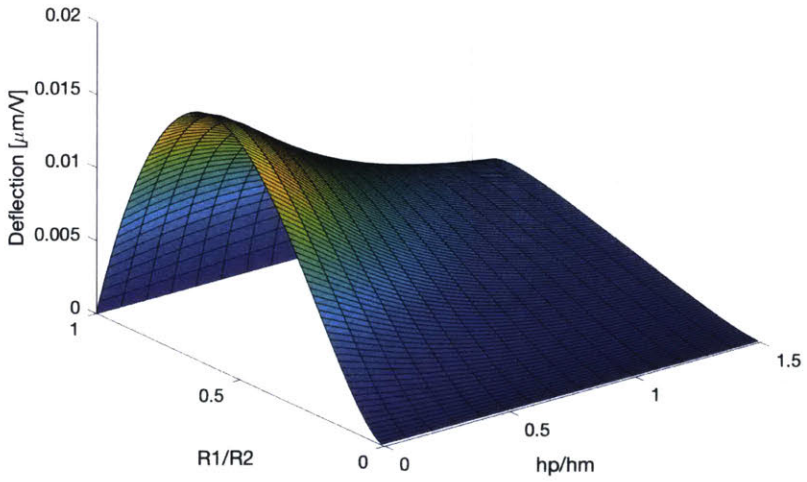

Figure 4-7: Center deflection of the transducer with varying thickness ratio and radius ratio.

One shortfall of the analytical solution is that when the piezo disk thickness is zero, the transducer still appears to deflect under voltage loading. This is not the

case in reality. However, as the piezo disk can still handle 1V down to a thickness of approximately 0.01mm, the solution serves as a useful tool over most of the design space.

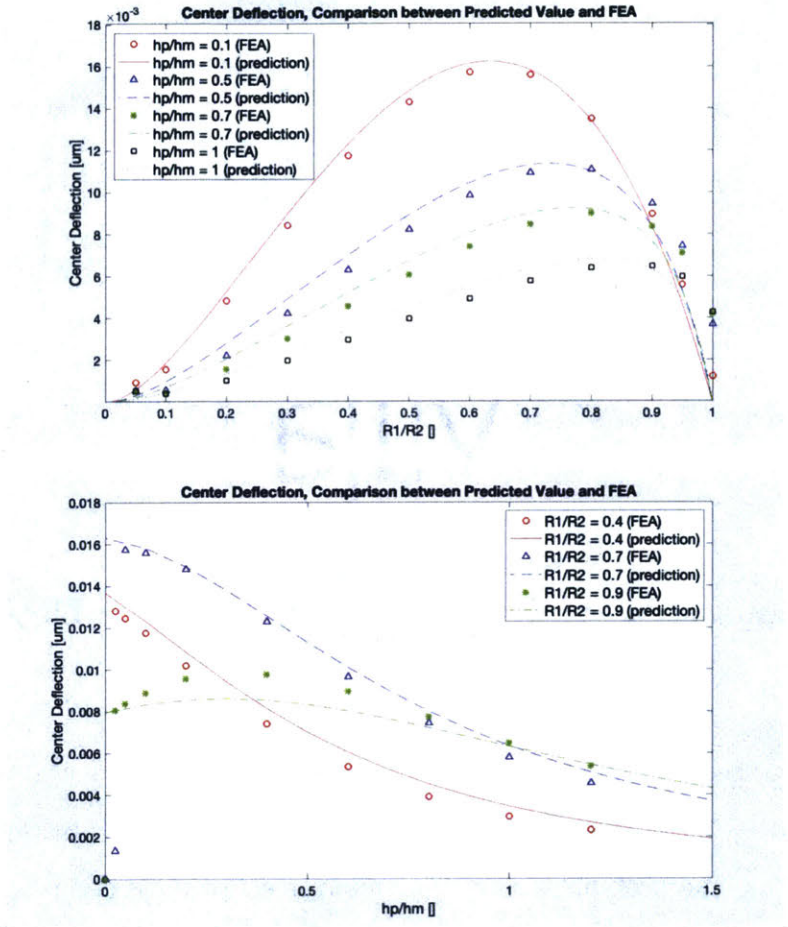

Figure 4-8: Simulated center deflection of the transducer with varying thickness ratio and radius ratio plotted against the analytical results.

The COMSOL study is set up as a 2D axisymmetric model, where the transducer is modeled as a cylindrical membrane with fixed edges and a cylindrical piezoelectric disk coupled to the membrane. A DC voltage of 1V is applied across the piezoelectric disk, with the top electrode grounded, and the maximum displacement of the membrane, which occurs at the center point, is recorded. Data from the simulation is plotted against the analytical solution in Figure 4-8 and shows good agreement. Unlike the analytical solution, at zero thickness the simulation shows that there will be zero

deflection, but as expected this drop occurs at small thicknesses. An image of one simulation result is shown in Figure 4-9 for reference.

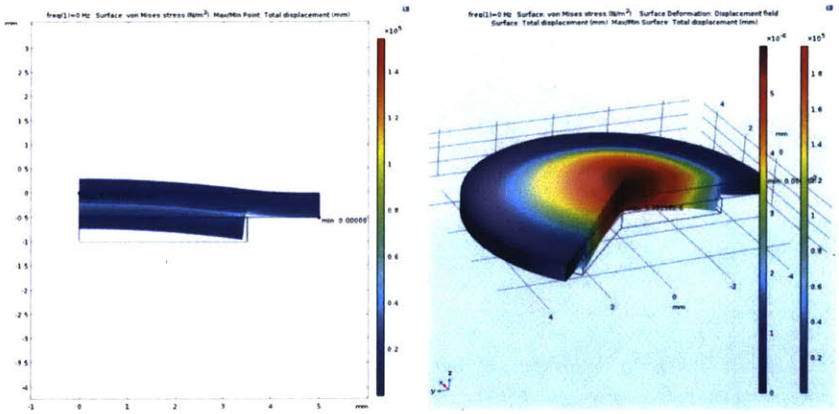

Figure 4-9: Image of stress results for a simulation of the transducer under voltage loading.

4.2.5 Acoustic Wave Propagation in a Hover Detection System

Once the pressure output of the transducer has been calculated, the change in pressure as it travels through the hover system can be computed. In order to simplify the calculations, the pressure can first be converted to decibels using the following equation:

$$L_p = 20 \log_{10} \left(\frac{|p|}{|p_{ref}|} \right) dB \; re \; p_{ref} \tag{4.18}$$

where p_{ref} for air is typically 20 μPa. The system considered here has been described in chapter 3 but is repeated here for clarity. It consists of one transmitting transducer and one receiving transducer, which lie in the same plane and face the same direction. A hand or other object is placed above the transducers and reflects the transmitted pressure waves back toward the receiver. For simplicity, the hand is considered to be a flat, infinite plane. This assumption should give an acceptable first order approximation provided the transducer size is small in comparison to the hand and the hand

is held flat.

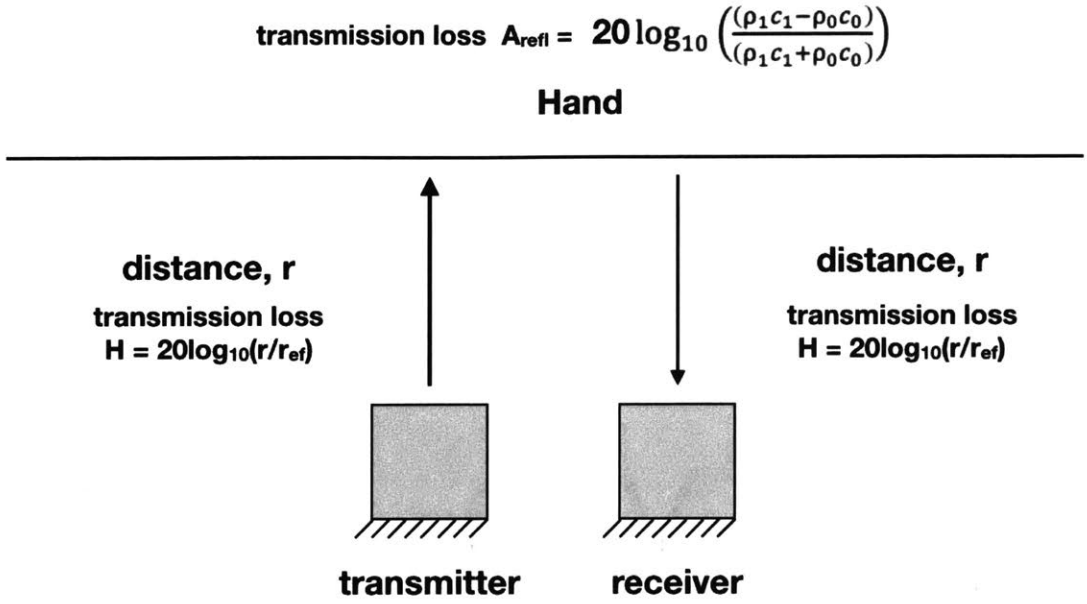

Figure 4-10: Simplified representation of the hover system with transmission losses.

Transmission loss due to propagation through free space can be calculated as

$$20\log_{10}\left(\frac{r}{r_{ref}}\right) \tag{4.19}$$

where r_{ref} is the reference distance and r is the distance to the point of interest, while transmission loss due to reflection off of the finger can be calculated as

$$20\log_{10}\frac{(\rho_1 c_1 - \rho_0 c_0)}{(\rho_1 c_1 + \rho_0 c_0)} \tag{4.20}$$

where $\rho_0 c_0$ is the acoustic impedance of air and $\rho_1 c_1$ is the acoustic impedance of the hand. The sound pressure level expected at the receiver would then be written as

$$L_{p,r} = L_p - 2 * 20\log_{10}\left(\frac{r}{r_{ref}}\right) + 20\log_{10}\frac{(\rho_1 c_1 - \rho_0 c_0)}{(\rho_1 c_1 + \rho_0 c_0)} \tag{4.21}$$

The sound pressure level at the receiver can be translated back to absolute pressure

as

$$p_r = 10^{\frac{L_{p,r}}{20}} p_{ref} \tag{4.22}$$

4.2.6 Voltage Generation in a Piezo Unimorph Under Pressure Loading

The last link to determine the voltage picked up by the receiver in this system is the sensitivity of the transducer, which describes the voltage produced across the transducer due to an input pressure. Liang et al. derive an analytical solution of sensitivity using electromechanical coupling and energy methods for uniform pressure loading [18]. Their solution for sensitivity is recorded below, and the derivation can be seen in their paper. It is assumed in the application of the solution to the current system that p_r, the pressure at the receiver, can be considered a plane wave since the pressure waves will have travelled approximately ten times the wavelength, allowing far field assumptions to be used. Liang et al. define the sensitivity as:

$$Sensitivity = \frac{V_{gen}}{P} = -\frac{3}{4}\frac{aB_3B_5d_{31}D_ch_mh_p(h_m+h_p)S_{11}^E S_m(1+\nu)}{B_6B_1b^2\pi\epsilon_{33}^T(1-\frac{2k_{31}^2B_7}{B_1(1-\nu)})} \tag{4.23}$$

Table 4.1: Constant definition for sensitivity calculations.

Variable	Definition
a	membrane radius
d_{31}	piezoelectric constant
h_m	membrane thickness
h_p	piezo disk thickness
S_{11}^E	piezoceramic elastic compliance constant
S_m	membrane elastic compliance constant
v	Poisson's ratio for composite plate
b	piezo disk radius
ϵ_{33}^T	permittivity of the piezo material in the direction of polarization under constant stress
k_{31}	electromechanical coupling factor for a piezo plate for low frequencies

where variables are as defined in Table 4.1 and D_c is the flexural rigidity of the

composite piezo and membrane plate, defined as [18]:

$$D_c = \frac{Y_c h_p^3}{12(1-\nu_c))} \tag{4.24}$$

where Y_c is the Young's modulus of the composite plate:

$$Y_c = c_1 Y_p + c_2 Y_m + \frac{c_1 c_2 Y_p Y_m (\nu_p - \nu_m)^2}{c_1 Y_p (1-\nu_m^2) + c_2 Y_m (1-\nu_p^2)} \tag{4.25}$$

with Y_p being the Young's Modulus of the piezo, Y_m the Young's Modulus of the membrane, ν_p the Poisson's ratio of the piezo, ν_m the Poisson's ratio of the membrane, and c_1 and c_2 constants defined as follows:

$$c_1 = \frac{h_p}{h_m + h_p} \tag{4.26}$$

$$c_2 = \frac{h_m}{h_m + h_p} \tag{4.27}$$

The constants B_1, B_3, B_4, B_5, B_6, and B_7 are defined as follows:

$$\begin{aligned}
B_1 &= 2abh_m h_p S_{11} S_m (h_m^3 S_{11} + h_p^3 S_m) + b^2 h_p^2 S_m^2 (4h_m^3 S_{11} + 6h_m^2 h_p S_{11} + 3h_m h_p^2 S_{11} \\
&\quad + h_p^2 S_m) + a^2 h_m^2 S_{11}^2 (h_m^3 S_{11} + 3h_m^2 h_p S_m + 6h_m h_p^2 S_m + 4h_p^3 S_m) \\
B_3 &= a h_m S_{11} + b h_p S_m \\
B_4 &= a^2 h_m^5 S_{11}^3 + a h_m^2 h_p ((3a+2b)h_m^2 + 6a h_m h_p + 4a h_p^2) S_{11}^2 S_m + b h_m h_p^2 (4b h_m^2 + 6b h_m h_p \\
&\quad + (2a+3b)h_p^2) S_{11} S_m^2 + b^2 h_p^5 S_m^3 \\
B_5 &= (a-b)(a+b)(2a^2 + b^2(3+\nu)) - 2a^2 b^2 (3+\nu)(\log(a) - \log(b)) \\
B_6 &= -b^2 (D_c - D_m)(1+\nu) + a^2 (D_c + D_m + D_c \nu - D_m \nu) \\
B_7 &= B4 - 3a^2 h_m^2 h_p (h_m + h_p)^2 S_{11}^2 S_m
\end{aligned} \tag{4.28}$$

Where D_m is is the flexural rigidity of the membrane, defined as:

$$D_m = \frac{Y_m h_m^3}{12(1-\nu_m)} \tag{4.29}$$

and all other variables are as defined above.

In order to calculate the sensitivity of the device operated at resonance, the amplification factor, A_r, is added to the definition. Sensitivity becomes:

$$Sensitivity = \frac{V_{gen}}{P} = -A_r \frac{3}{4} \frac{aB_3B_5d_{31}D_c h_m h_p (h_m + h_p) S_{11}^E S_m (1+\nu)}{B_6 B_1 b^2 \pi \epsilon_{33}^T (1 - \frac{2k_{31}^2 B_7}{B_1(1-\nu)})} \tag{4.30}$$

4.2.7 Amplification Factor at Resonance

Up to this point, absolute deflection has been calculated for the static loading case, and an unknown amplification factor has been included to account for the amplification at resonance. The transducer can be thought of as a second order system, in which case the amplification factor A_r, also known as Q, can be expressed in terms of the damping ratio, ζ, as:

$$A_r = \frac{1}{2\zeta\sqrt{1-\zeta^2}} \; (\zeta \leq 0.707) \tag{4.31}$$

However, the damping ratio is difficult to model analytically, so the amplification factor will be determined experimentally further on.

4.3 Fabrication

4.3.1 Current Fabrication Process

A prototype with the layout shown in figure 4-1 has been built and characterized. It is made from the following components:

- Machined 4140 steel front plate

- Waterjet 4140 steel back plate
- Axially polarized piezoceramic disks (APC material 851)
- Epoxy (Loctite EA E-30CL) with 0.002" diameter glass microspheres (Miapoxy 65) mixed in
- 32 gauge wire

The main dimensions of interest are shown in Figure 4-11. An SLA vacuum fixture

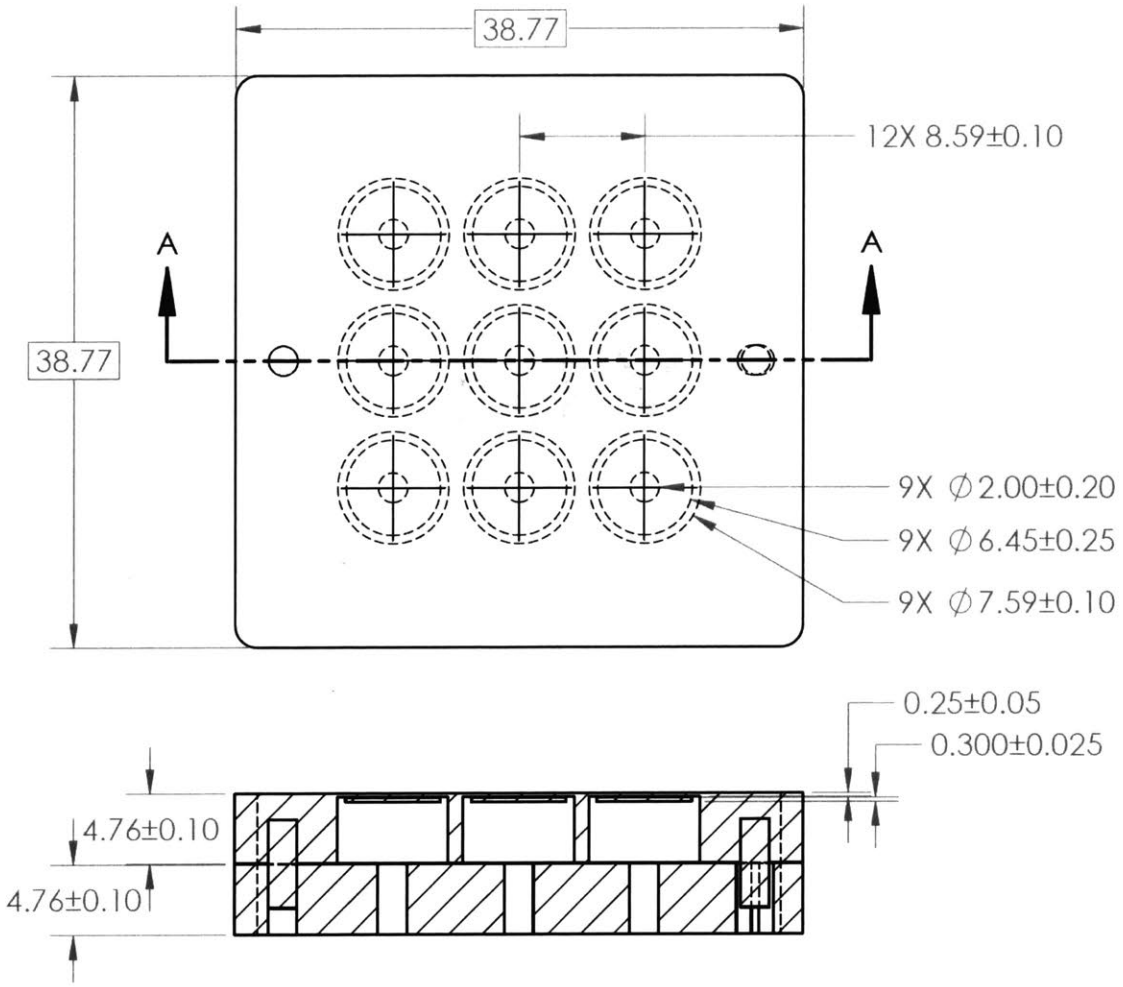

Figure 4-11: Dimensioned drawing of array prototype. Dimensions are in millimeters.

printed on the Formlabs Form 2 SLA printer, a Robinair VacuMaster vacuum pump, Blu Tack, and a 1kg weight were also used during assembly.

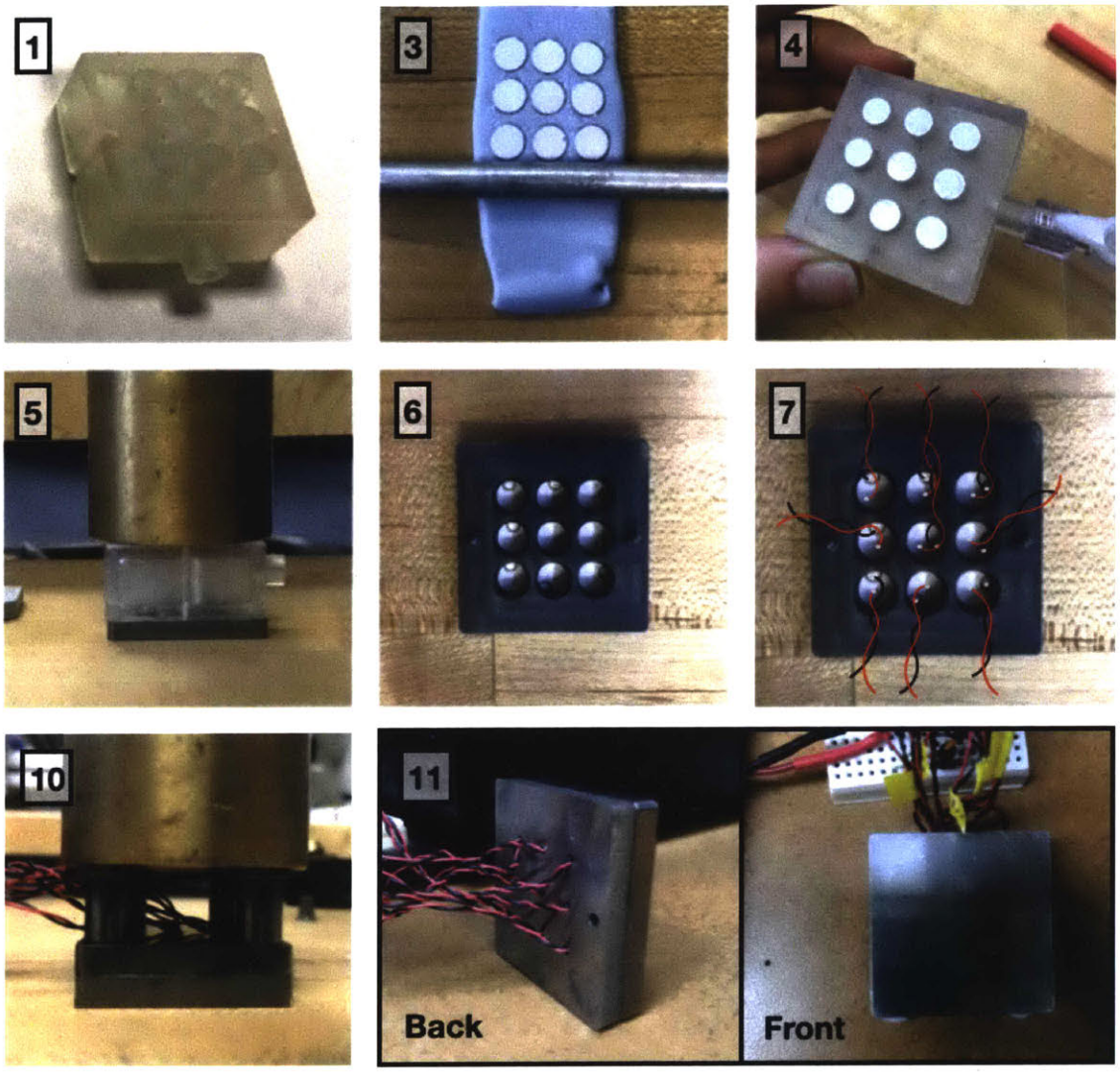

Figure 4-12: Pictures of fabrication process and finished array.

The assembly was performed according to the following steps, some of which are illustrated in Figure 4-12.

1. Spray vacuum fixture with mold-release.

2. Mix epoxy and mix 0.05 mm diameter microspheres into epoxy.

3. Mount piezo disks (ground side up) in putty and apply epoxy using a roller rod.

4. Align piezo disks (ground side up) on top of vacuum fixture and draw vacuum.

5. Place vacuum fixture (piezo disk side down) into steel front plate and align

with pins, then place 1kg weight on top of vacuum fixture and turn vacuum off. Allow 24h for epoxy to cure.

6. Remove weight and vacuum fixture.

7. Solder leads to piezo electrodes.

8. Mix epoxy and microspheres and apply to steel back plate using roller rod.

9. Thread leads through exit holes in back plate.

10. Place back plate onto front plate, aligning with pins, and place standoffs with 1kg weight on top of steel plates. Allow 24h for epoxy to cure.

11. Remove weights.

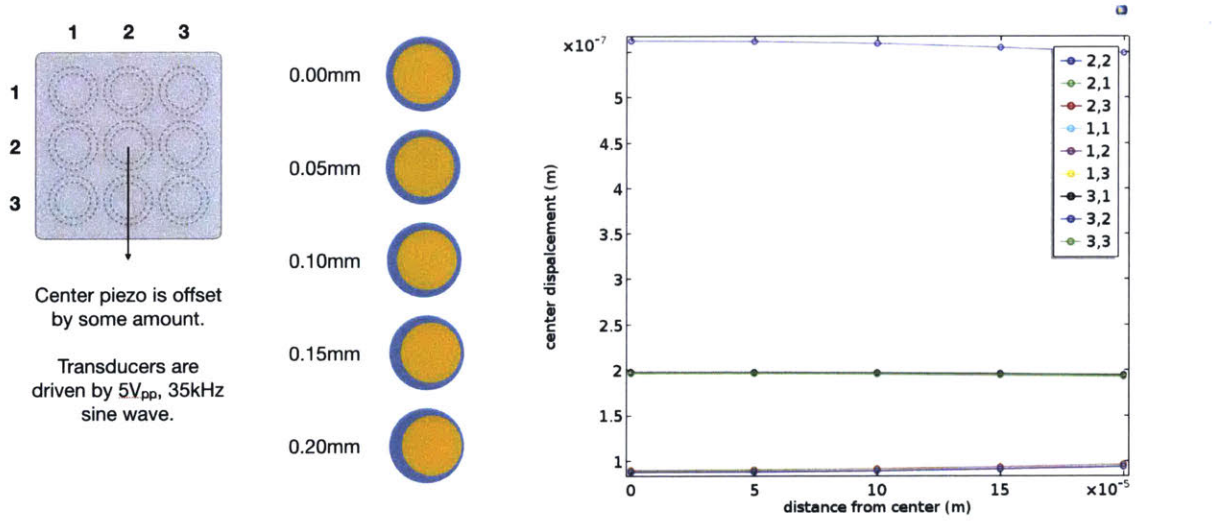

Figure 4-13: Results from the COMSOL simulation of transducer center displacement with error in concentricity between the central piezo element and the membrane. Transducers are referred to by their location in the grid shown on the left. Results show little variation with increased concentricity error.

One of the main concerns with this method of assembly is that the piezo disks may not be perfectly centered on the vacuum fixture or may shift when inserted into the steel front plate. In order to assess whether this method would suffice, a simulation was run to determine the change in center displacement of the transducers with error

in concentricity between the piezo element and the steel membrane. This simulation was performed in COMSOL. A 5Vpp sine wave at the transducers' resonant frequency was applied across each of the piezo disks and the central (2,2) piezo disk was offset from center in steps of 0.05 mm up to 0.2 mm. At each step, the simulation was run and the center displacement of each transducer was probed. The results are shown in Figure 4-13 and show little variation with increased concentricity error. Based on these results, the assembly procedure described above was deemed acceptable. The assembly can be validated by looking at the variation in frequency response across the various transducers. If the assembly method works well, there should be a clear and consistent resonant peak. These measurements were performed and are reported in section 4.4, Transducer Characterization.

4.3.2 Alternative Fabrication Methods

One alternative fabrication method that was explored involved separating the steel front plate into two separate components, a steel baffle with holes defining the transducer walls and a thin sheet of steel that served as the membrane, which were joined using epoxy. The beginning of the assembly process was modified to include the following steps:

1. Spray vacuum fixture and alignment fixture with mold-release.
2. Mix epoxy and mix 0.05 mm diameter microspheres into epoxy.
3. Apply epoxy to one side of the membrane using a roller rod.
4. Position membrane in alignment fixture, epoxied side up.
5. Place steel baffle onto vacuum fixture, aligning with pins.
6. Align piezo disks (ground side up) on top of vacuum fixture and draw vacuum.
7. Place vacuum fixture and steel baffle (piezo disk side down) onto steel membrane in alignment fixture and lock in place. Then place 1kg weight on top of vacuum fixture and turn vacuum off. Allow 24h for epoxy to cure.

At this point the process continued as before. Some of the modified steps are illustrated in Figure 4-14.

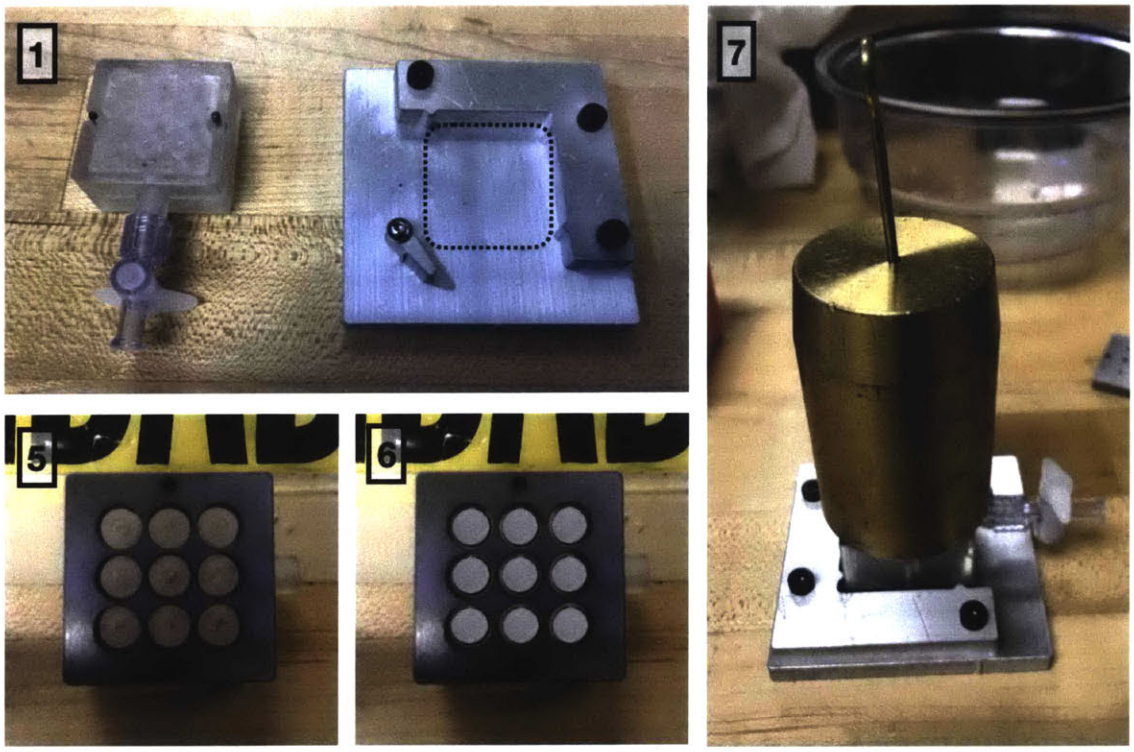

Figure 4-14: Pictures of modified fabrication process. The dotted outline in image 1 indicates where the membrane was positioned in the alignment fixture.

This modified process reduces manufacturing time and cost. However, it demonstrated two main drawbacks: the frequency response was less consistent across array elements, and simulations showed a larger amount of crosstalk between elements. Sheet epoxy, which is used for circuit boards, could be explored as a way to achieve a more consistent response with epoxy, due to its precise thickness. Another option to explore would be maintaining the two part front plate, but joining the plates in another way, perhaps welding, to achieve a more consistent response than the epoxy gives.

4.4 Transducer Characterization

4.4.1 Frequency Response

The frequency response of the transducers can be measured using only a function generator, oscilloscope, and sense resistor using the configuration shown in Figure 4-15. The series combination of the transducer and sense resistor are driven through a frequency sweep by the function generator, and the voltage across the sense resistor is measured by the oscilloscope. At resonance, the piezo transducer will be most willing to give and receive current, so the voltage observed across the sense resistor will be at its highest.

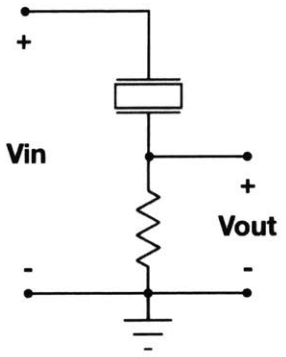

Figure 4-15: Circuit to measure transducer frequency response. V_{in} is 20 V_{pp} and the value of the resistor is 100Ω.

The frequency response of each transducer in the array was observed by driving its piezo element with a 20Vpp sine wave and reading the voltage across its sense resistor while letting the other transducers float. The results are shown in Figure 4-16. There is a fairly consistent frequency response across the transducers, which is an indicator that the fabrication process described before is sufficient for creating prototypes. The resonant frequency for the transducers is around 40kHz ± 1kHz. The resonant frequency predicted by the analytical model was approximately 44kHz, which is not far off considering it was based on the thin plate model which neglected the piezo disk. The results are close enough to use the analytical solution as a design tool.

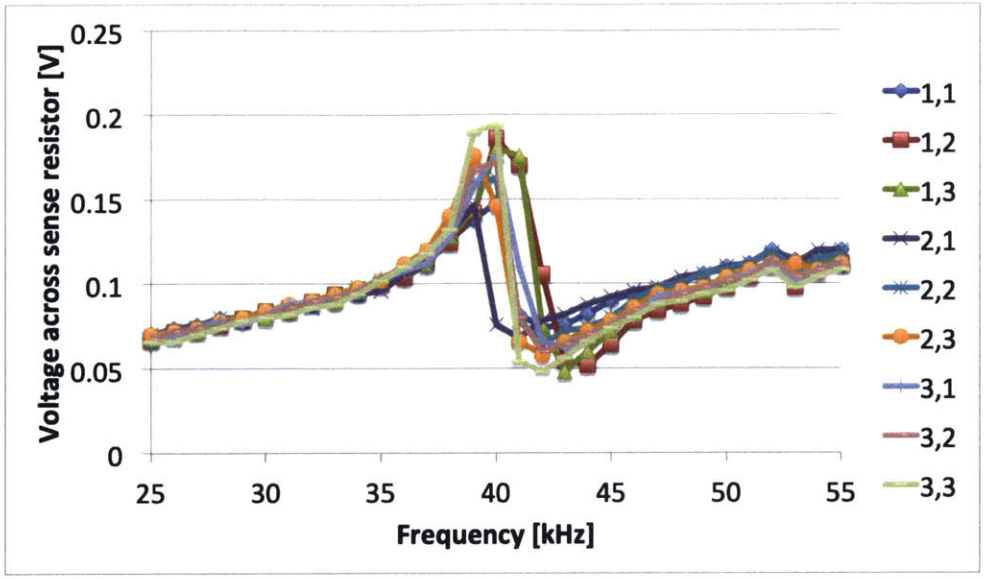

Figure 4-16: Frequency response for each transducer in the prototype array.

4.4.2 Power Consumption of Hover Detection System

The power consumption of an individual transducer operated at resonance at 20Vpp can be calculated using the the circuit shown in Figure 4-15. The peak to peak current through the transducer can be calculated using the voltage measured across the sense resistor and the value of the resistor as $I_{pp} = \frac{V_{out}}{R}$. The peak to peak voltage across the transducer can be calculated as $V_{pp} = V_{in} - V_{out}$. These values can be converted to the RMS values by dividing by 2.8, and then the average power, P_{avg}, across the transducer can be calculated from the RMS values as:

$$P_{avg} = I_{RMS} V_{RMS} \tag{4.32}$$

The power consumed by each transducer in the prototype is approximately 6 mW.

4.4.3 Deflection Under Voltage Loading

In order to validate the analytical model, the surface deflection of the transducer was measured using a laser vibrometer, the Polytec IVS-500. The transducer array was mounted to a YZ translation stage using a 3D printed fixture and Blu Tack,

as shown in Figure 4-17. The stage was positioned such that the front face of the transducer was a distance of 329 mm from the front of the vibrometer in order to obtain maximum signal level, according to guidelines in the IVS-500 manual. The stage was moved in increments of 1 mm in Y and Z in order to obtain a grid of surface deflection measurements.

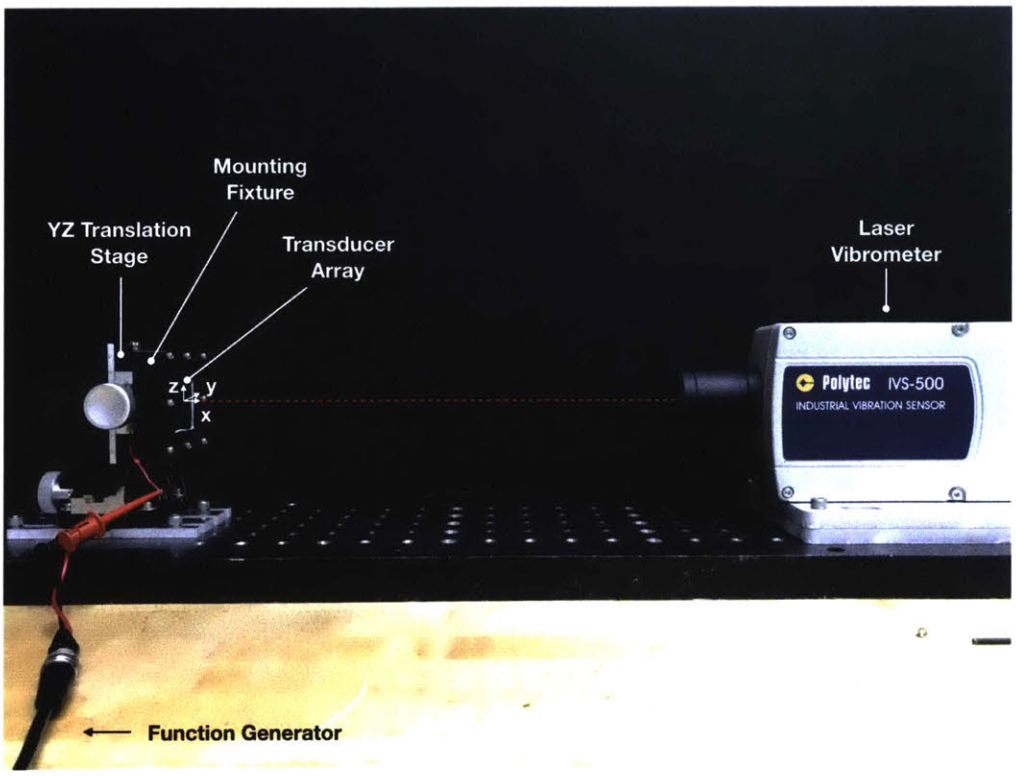

Figure 4-17: Laser vibrometer setup. Plate deflection of interest occurs in the x direction.

The results were used to calculate the amplification factor mentioned previously in this section by dividing the maximum of the measured displacement by the maximum predicted displacement for each analytical model. An amplification factor of approximately 18.3 was obtained for the piezo unimorph model, which calculates the static displacement, and an amplification factor of 1.0306e-06 was obtained for the thin plate model, which had an arbitrary scaling factor of 1. The results for the displacement along the midline of the transducer are plotted against the scaled analytical solutions using the thin plate model and the piezo unimorph model in Figure

4-18. The piezo unimorph model more accurately reflects the results, but the thin plate model can be used to give an approximation of acoustic pressure.

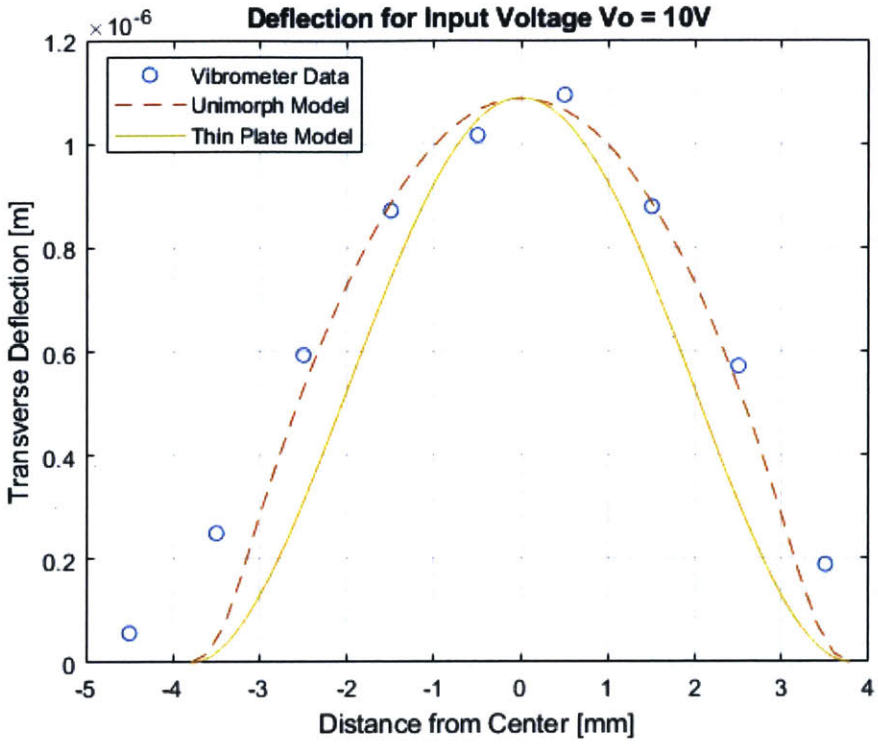

Figure 4-18: Analytical and experimental results for deflection along the midsection of the transducer.

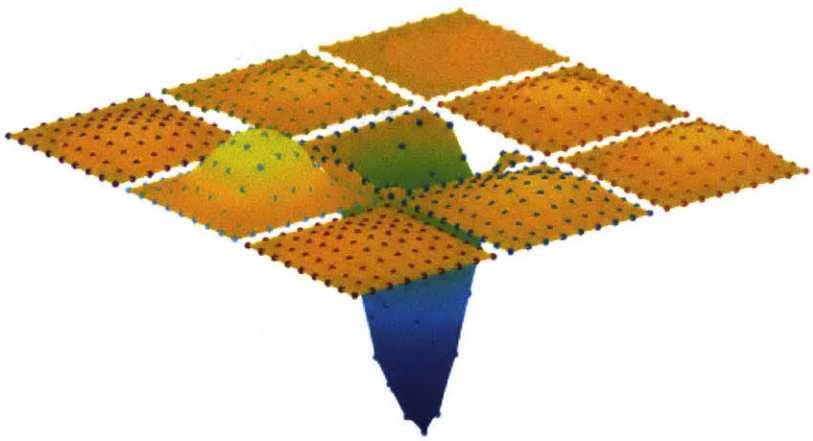

Figure 4-19: Map of transducer array surface deflection, constructed from the vibrometer data.

The data from the full scan is shown in Figure 4-19. Ideally, when the center transducer is driven the surrounding transducers should not experience any displacement unless there is an object above the surface that reflects a pressure wave back toward them. However, as shown in the scan, the other elements do experience some deflection. This crosstalk is not captured in the analytical model, so simulations on the full array geometry are performed in COMSOL to try and capture the behavior, as discussed in section 4.5.

4.4.4 Acoustic Pressure Output

An off the shelf receiver, the MA40S4R, was used to measure the pressure output of the transducer array. The transducer array was mounted on the table with Blu Tack, and the receiver was positioned 100 millimeters above the center transducer, element (2,2), as shown in Figure 4-20.

Transducer (2,2) was driven at 40kHz with a 20 V_{pp} sine wave, and the voltage was measured across the load resistor for the receiver. The measured voltage, V_{in}, was 74 mV_{pp}, or 26 mV_{RMS}. This result, as well as the sensitivity, s, of the receiver as given by the manufacturer, -63dB re 10 V/Pa with a 3.9 $k\Omega$ load resistance, were used to calculate the pressure output and source level of the transducer, as follows. First, the pressure at the receiver, p_{rec}, is calculated as

$$p_{rec} = \frac{V_{in}}{10^{\frac{s}{20}} s_{ref}} \tag{4.33}$$

Next, the transmission loss through space, H, is calculated as

$$H = 20 \log_{10} \frac{r}{r_{ref}} \tag{4.34}$$

where r is the distance from the transmitter to the receiver, in this case 0.1m, and r_{ref} is the reference distance, in this case 0.3m. Finally, the source level of the transmitter,

L_s is calculated as

$$L_s = 20 \log_{10} \frac{p_{rec}}{p_{ref}} + H \tag{4.35}$$

where p_{ref} is $20\mu Pa$ for air. The pressure output of the transducer was calculated to be 2.3Pa and the source level was calculated to be 91.5dB re $20\mu Pa$ and 30cm.

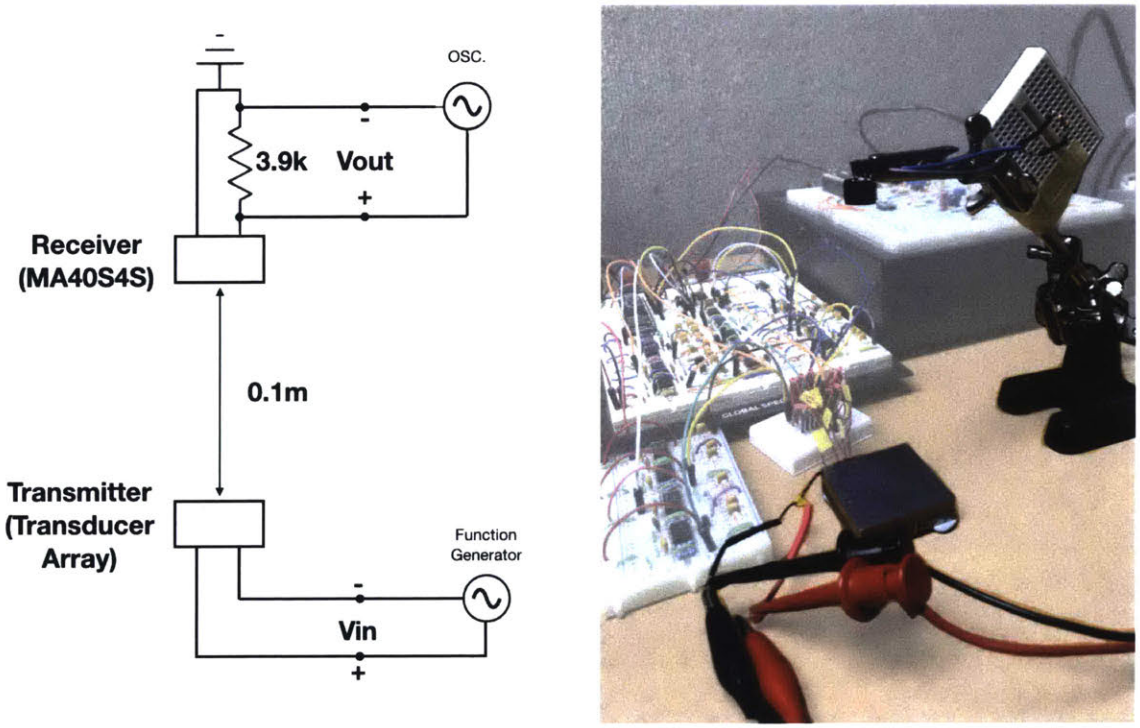

Figure 4-20: Experimental setup to measure the source level of the transducer array in transmit mode.

The same procedure was carried out to measure the source level of an off the shelf transmitter, the MA40S4S, in order to validate the measurement process. The source level was measured to be 117.3dB, which is in line with the manufacturer specifications, reported in appendix D.

The same circuit was used to measure the pressure at various distances directly above the center transducer and to measure the beam profile in the far field. For these measurements, the transducer array and the receiver were mounted in an anechoic chamber to minimize stray reflections from the room. Two structures were used to

mount the transducer array: a linear slide for the on-axis measurements and a rotation stage for the beam pattern measurements. The two configurations are shown in Figure 4-21, and the results are reported later in this chapter.

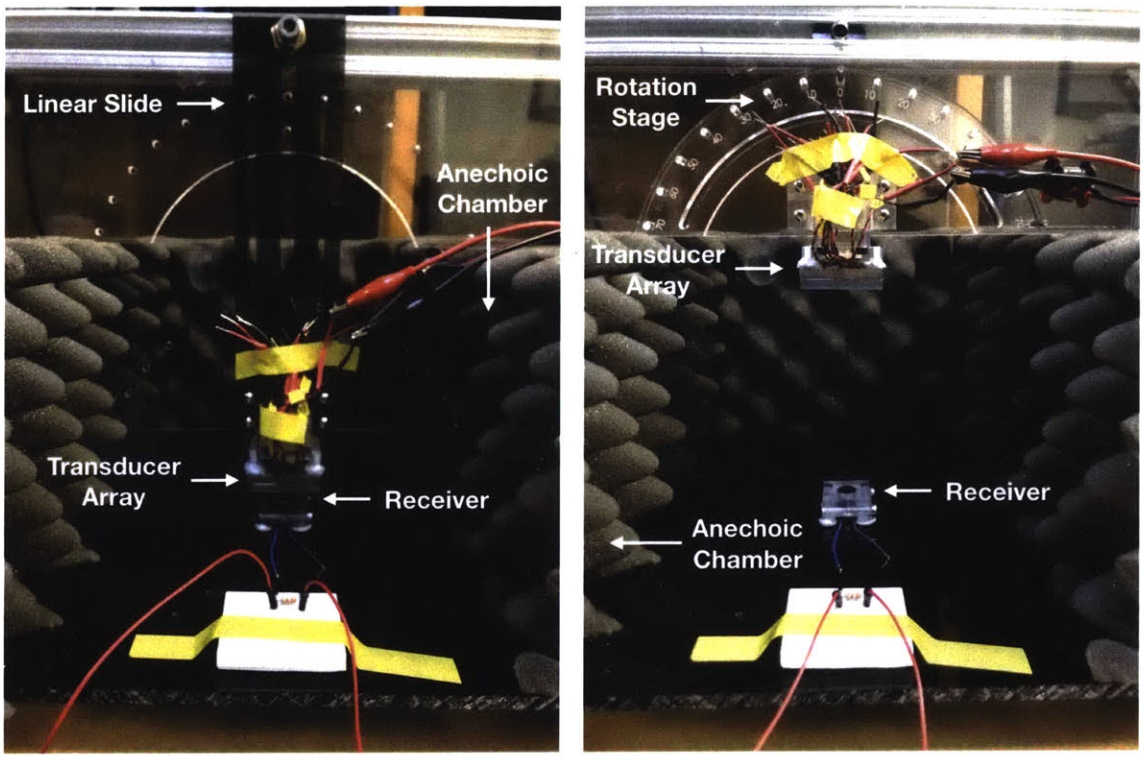

Figure 4-21: Anechoic chamber with linear slide (left) and rotation stage (right) with fourth wall removed.

4.4.5 Sensitivity

An off the shelf transmitter, the MA40S4S, was used to measure the sensitivity of the transducer array. The transducer array was mounted on the table with Blu Tack, and the transmitter was positioned 100 millimeters above the center transducer, element (2,2) as shown in Figure 4-22.

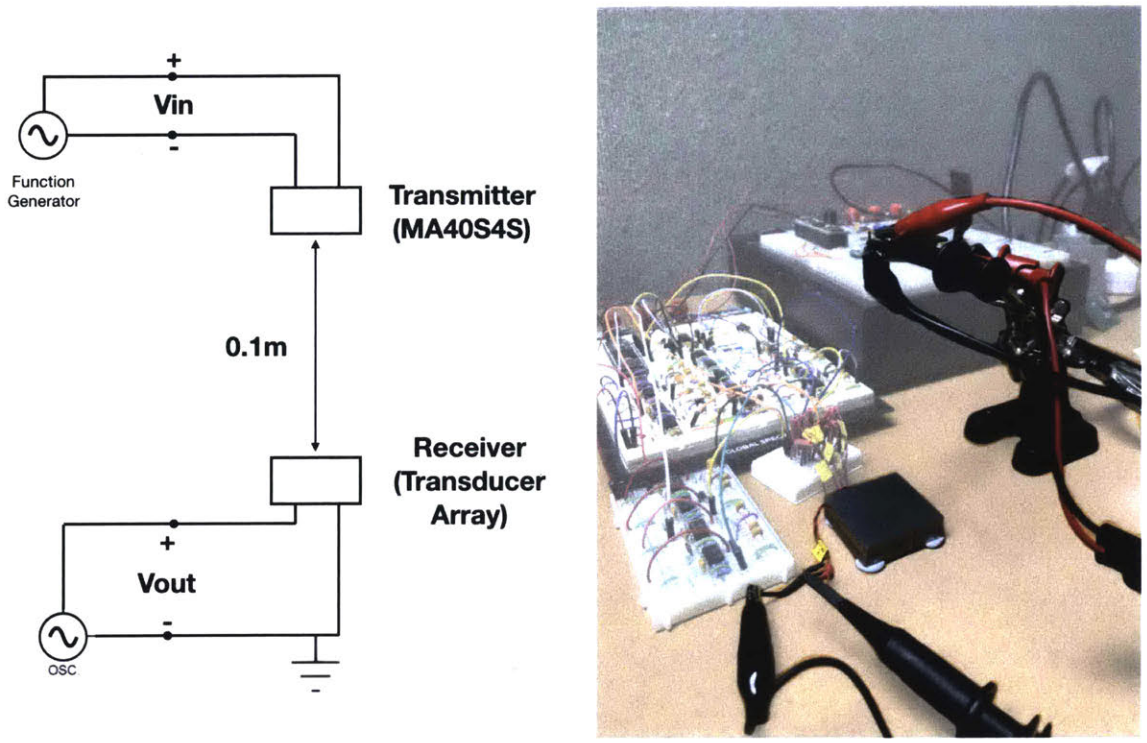

Figure 4-22: Experimental setup to measure the sensitivity of the transducer array in receive mode.

The MA40S4S was driven at 40kHz with a 20 V_{pp} sine wave, and the voltage across element (2,2) was measured. The measured voltage, V_{in}, was 54 mV_{pp}, or 19 mV_{RMS}. This result, as well as the source level, L_s, of the transmitter as given by the manufacturer, 117dB re 20 μPa and 30cm with an applied voltage of approximately 7 V_{RMS}, were used to calculate the sensitivity of the transducer, as follows. First, the pressure at the receiver, p_{rec}, was calculated as

$$p_{rec} = 10^{\frac{L_s - H}{20}} p_{ref} \tag{4.36}$$

where H is $20log_{10}\frac{r}{r_{ref}}$ and the constants are the same as previously defined. Next, the transfer function, TF, that relates the input pressure to the voltage produced across the piezo is calculated as

$$TF = \frac{V_{in}}{p_{rec}} \tag{4.37}$$

Finally, the sensitivity, s, is calculated as

$$s = 20 \log_{10} \frac{TF}{s_{ref}} \tag{4.38}$$

where s_{ref} is 10 V/Pa, as before. The sensitivity of the transducer was calculated to be -87dB re 10 V/Pa and the transfer factor to be 0.4 mV/Pa.

4.4.6 Crosstalk Signals

Crosstalk is evident in both the membrane displacement of passive transducers and the voltage across them. The latter is easier and less expensive to measure, as it only requires a function generator and oscilloscope as opposed to a laser vibrometer, so it may serve as a more helpful design tool.

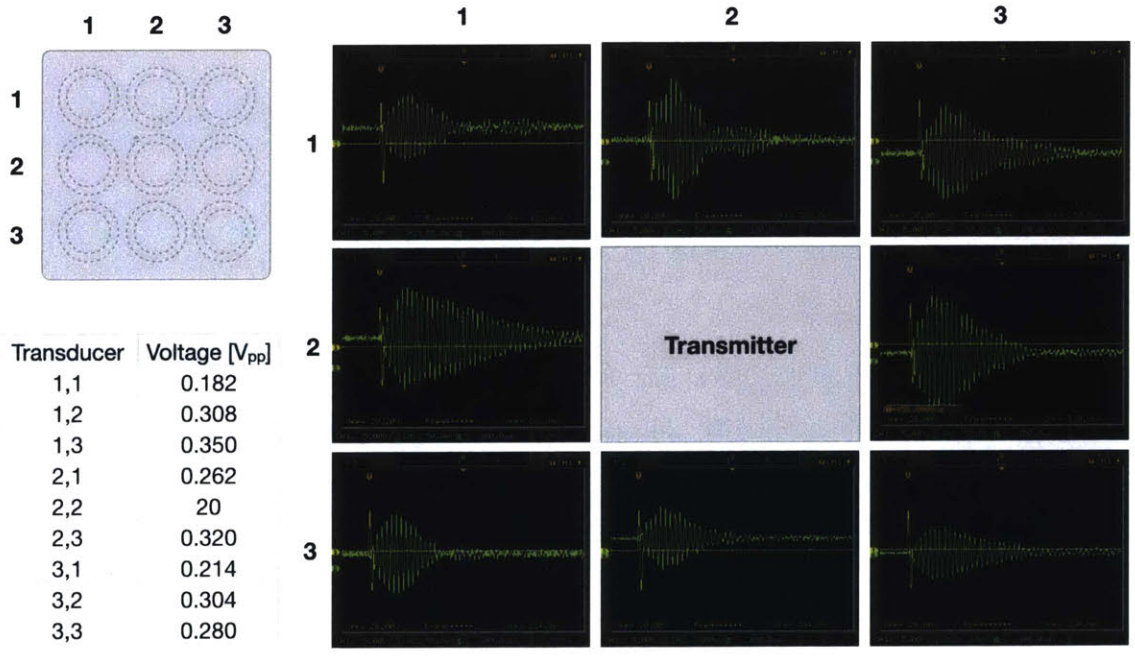

Figure 4-23: Voltage generated on passive transducers due to crosstalk when element 2,2 is driven with a 20Vpp single sine pulse at 40kHz. The driving pulse is shown in yellow and the response is shown in green.

In order to electrically measure the crosstalk in the current prototype, element 2,2 was driven with a 20Vpp single sine pulse at 40kHz and the voltage on the receive

transducers was measured and is reported in Figure 4-23. The same procedure was repeated with a continuous sinusoidal signal for comparison with simulation, and is reported in the next section.

The average crosstalk signal is about two orders of magnitude higher than the estimated voltage due to a hover gesture for a single sine burst and higher still for the continuous sine signal. There is a possibility that the crosstalk signal could be characterized and then subtracted out of the readings for hover detection, but it is preferable to reduce the crosstalk signal itself so that the measured hover signal can be higher resolution. Methods for crosstalk reduction will be discussed further in the remainder of this chapter and in future work.

4.5 Simulation

In order to better understand the effects of crosstalk, which is not captured in the analytical model, and to explore ways to reduce crosstalk, a COMSOL simulation was created to model the system.

4.5.1 Model Setup

The simulation was set up as a 3D model using the solid mechanics, electrostatics, and pressure acoustics, frequency domain modules. The device geometry was imported from SolidWorks as solid bodies and a hemispherical air domain was built around the device. A sound hard boundary condition was applied to the bottom face of the air domain to simulate the extension of the transducer surface when incorporated into a larger structure or mounted on a table, and a spherical wave radiation condition was applied to the spherical surface, to simulate the extension of the air domain past the meshed area. The outer edges of the transducer array were fixed. Since the device is symmetric, one quarter of the device and the air domain were modeled to reduce computation time, and symmetry boundaries were imposed on the cut faces of the various domains. The geometry is shown in Figure 4-24.

The simulation makes use of the built in materials for air, structural steel, and

lead zirconate titanate (PZT-5H) and a custom material for the epoxy using material properties from the datasheet for Loctite EA E-30CL. In future simulations, custom materials should be built for the piezoceramic used in the device and the particular grade of steel, but the built-in materials worked for the current purposes. An isotropic structural loss factor of 0.05 was used for the steel domain, based on a COMSOL tutorial [5]. The epoxy was modeled as a thin elastic layer with spring properties taken from the material data, a thickness of 0.0508 mm, and loss factor of 0.005. The loss factor was chosen by setting the other variables as constant and running the simulation with a few different values of epoxy loss factor. The simulation with loss factor of 0.005 matched experimental data best. It is strange that in the simulation that matched best, the loss factor of the epoxy is lower than that of the steel; more work should be done to check whether this is the best way to model the system, or whether the damping parameters should be adjusted.

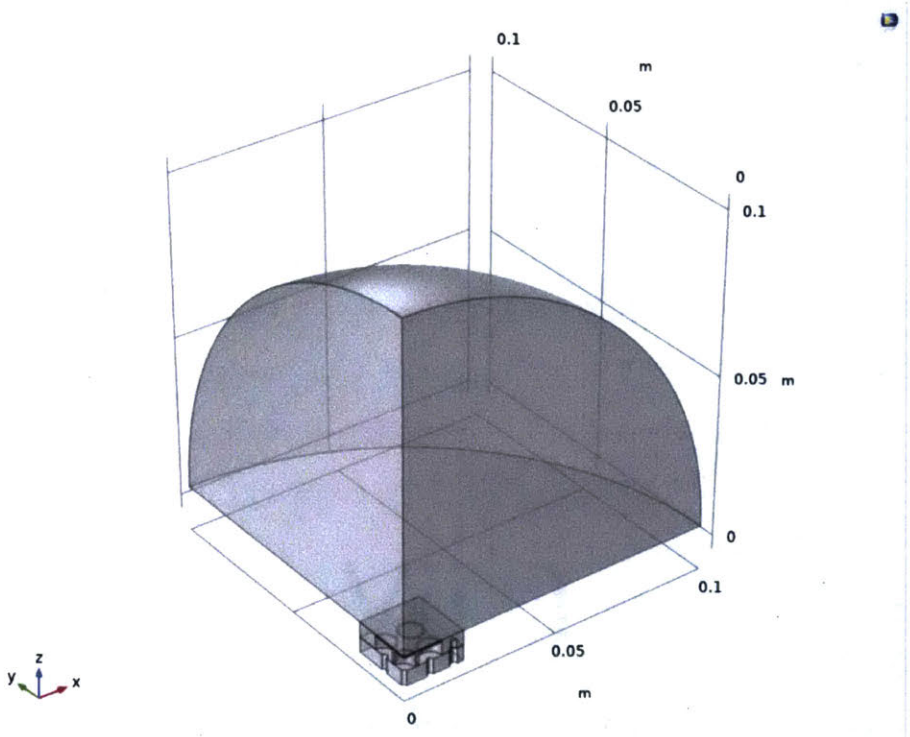

Figure 4-24: Geometry in the COMSOL model for the transducer array.

Two separate simulations were performed for the device, one which modeled its

behavior as a transmitter and one which modeled its behavior as a receiver. Both simulations used a frequency domain study to identify the resonant frequency of the device and then model behavior at that frequency. In the transmitter case, an electric potential of 20Vpp was applied across the central piezo element and a floating potential was observed on the surrounding piezo elements. The deflection of the transducer surfaces, the values of the floating potentials, and the pressure field in the air domain were the outputs of the study. In the receiver case, floating potentials were set across all piezo elements, and a plane wave directed toward the transducer surface was applied as an incident pressure field perpendicular to the surface. The deflection of the transducer surfaces and the values of the floating potentials were the outputs of the study.

4.5.2 Transducer Center Displacement

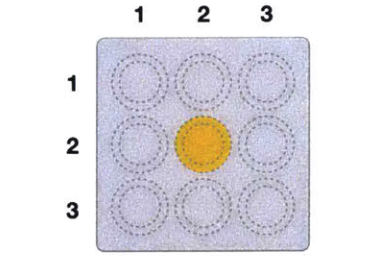

Transducer	δ_{meas} [μm]	δ_{qs39} [μm]	δ_{qs40} [μm]
1,1	0.0450	0.0639	0.1615
1,2	0.0570	0.0951	0.2221
1,3	0.0370	0.0639	0.1615
2,1	0.1600	0.0963	0.2272
2,2	1.0090	1.0556	0.7590
2,3	0.0950	0.0963	0.2272
3,1	0.0410	0.0639	0.1615
3,2	0.0700	0.0951	0.2221
3,3	0.0830	0.0639	0.1615

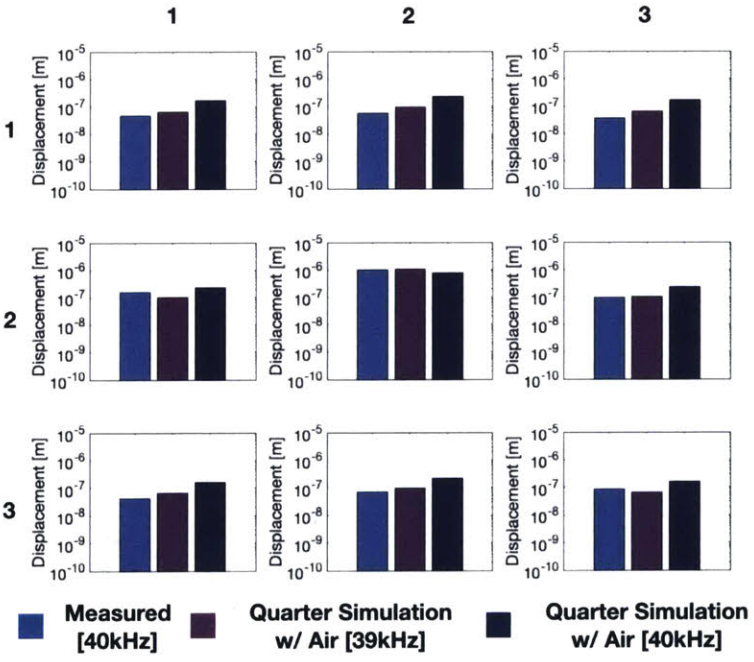

Figure 4-25: Measured and simulated transducer center displacement.

The simulated values for the center displacement on each transducer are plotted against the measured values in Figure 4-25. The resonant frequency of the prototype

array was measured to be approximately 40kHz, while the simulation predicted a resonant frequency of 39kHz. Simulation results for both 39kHz and 40kHz are plotted, and 39kHz shows better agreement with the measured data for all transducers but element 2,1, which lies between the 39kHz and 40kHz simulations. The discrepancy between elements is likely due to variation in the fabrication process. When comparing results, the measurements at 40kHz and the simulation at 39kHz will be used.

A simulation with the full array geometry and no air domain was also performed and its results are plotted against those of the quarter array geometry simulation with air domain in Figure 4-26. The simulations show good agreement, and the simulation without air can serve as a quicker method to explore how changing array geometry will affect crosstalk, for both symmetric and asymmetric geometries.

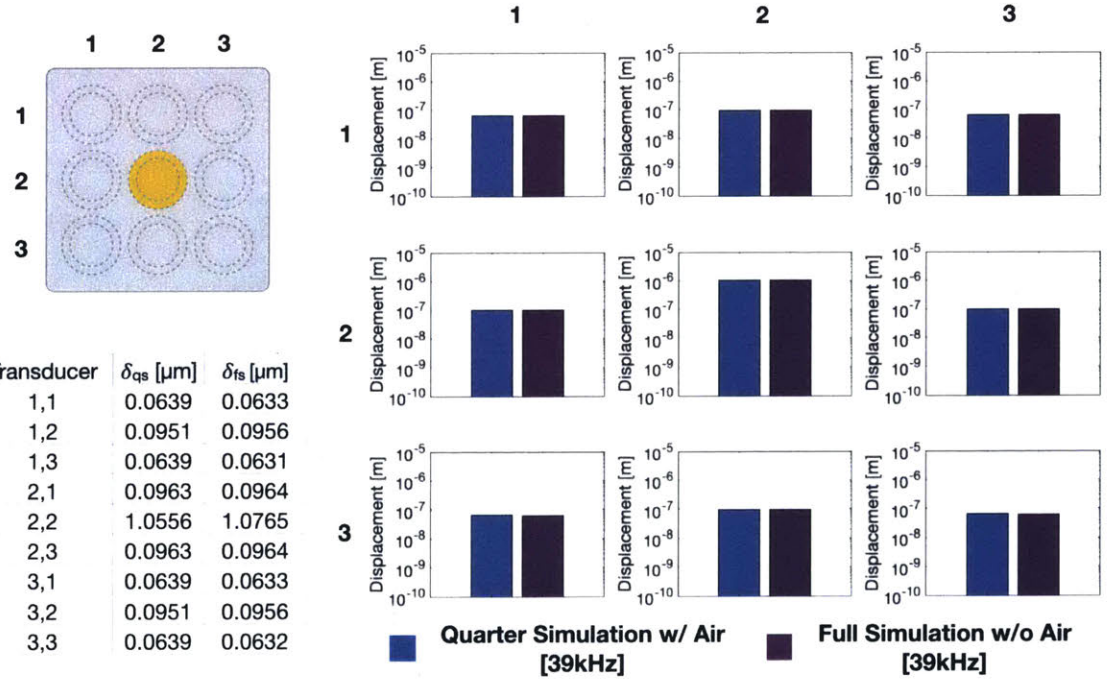

Transducer	δ_{qs} [μm]	δ_{fs} [μm]
1,1	0.0639	0.0633
1,2	0.0951	0.0956
1,3	0.0639	0.0631
2,1	0.0963	0.0964
2,2	1.0556	1.0765
2,3	0.0963	0.0964
3,1	0.0639	0.0633
3,2	0.0951	0.0956
3,3	0.0639	0.0632

Figure 4-26: Simulated transducer center displacement for the quarter simulation with air domain and the full simulation without air domain. The two simulations show good agreement.

The normalized deflection profile along the midsection of the center transducer

for the quarter simulation is plotted against the analytical and measured results in Figure 4-27.

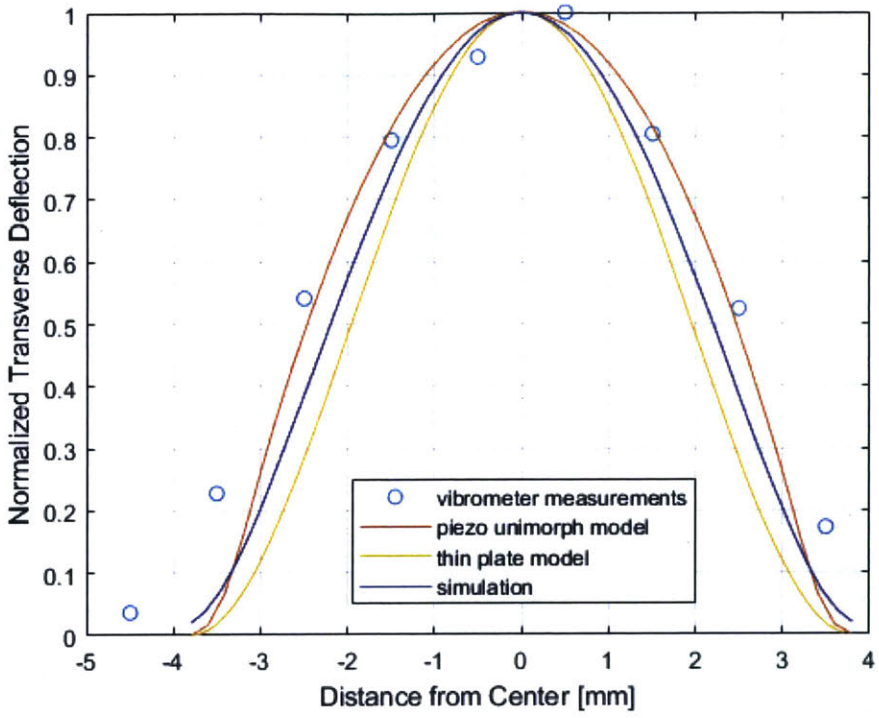

Figure 4-27: Analytical, experimental, and simulated results for normalized deflection along the midsection of the transducer.

4.5.3 Pressure

The pressure in the air domain above the transducer is simulated and is plotted along two profiles. The first looks at the on-axis pressure directly above the center transducer. Once the sensitivity of the device is known, this profile will help determine the range at which the sensor would be able to detect hover with an adequate signal to noise ratio. The second looks at the pressure profile measured at a radius of 0.1m from the center of the transducer. This gives an indication of the far field beam pattern and the directivity of the sensor. Both profiles are shown in Figure 4-28, and the simulation results are compared with the analytical model and experimental data below.

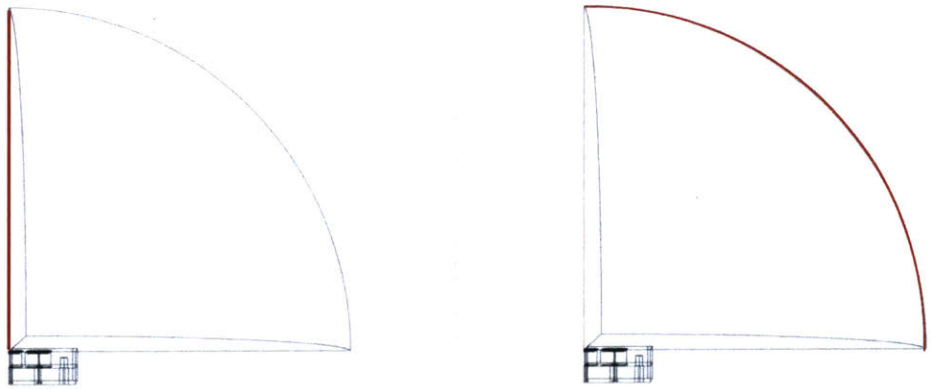

Figure 4-28: Profiles for pressure evaluation: on-axis (left), at a radius of 0.1m (right).

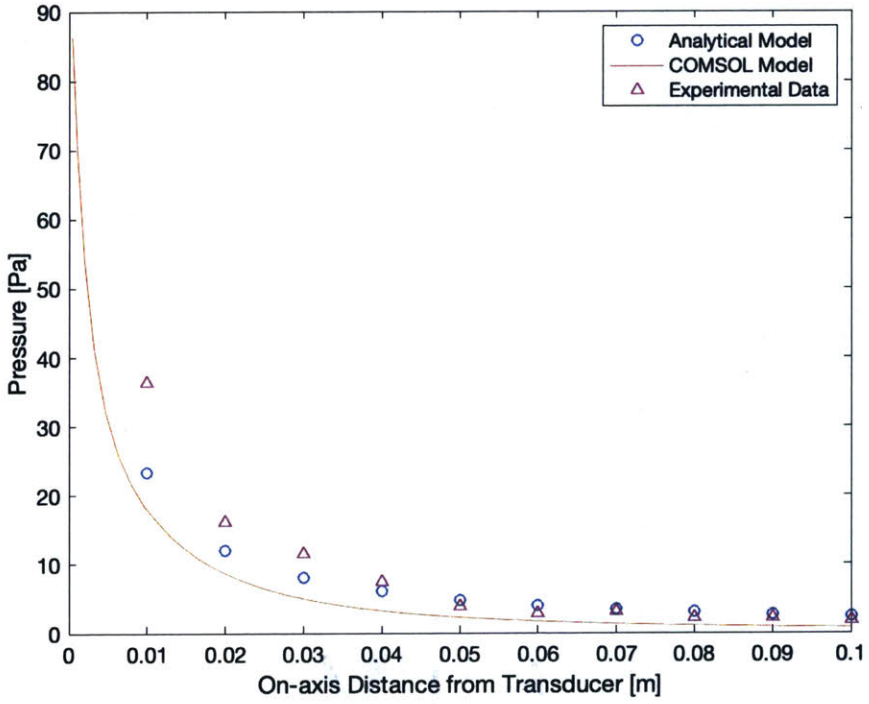

Figure 4-29: Pressure evaluated along on-axis profile.

The simulated, analytical, and measured pressure along the on-axis profile are plotted in Figure 4-29. The analytical model and COMSOL model display the same shape, but the COMSOL model lies approximately 1.5Pa below the analytical model.

The experimental data follows a similar trend, but has higher values than the analytical model up to about 50 mm from the surface and lower values than the analytical further away. Both analytical and simulated results are well within an order of magnitude and can give a fair approximation for pressure levels in device design.

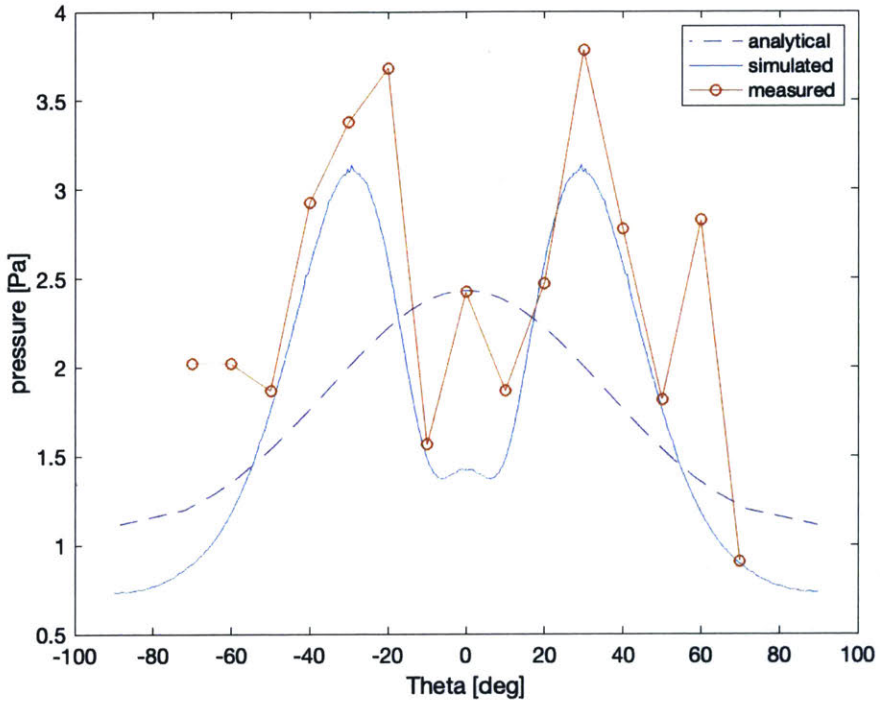

Figure 4-30: Pressure evaluated at a radius of 0.1 m from the center of the transducer array.

Figure 4-30 shows the pressure evaluated at a radius of 0.1 m from the center of the transducer array. The measured pressures are slightly greater than the simulated pressures but show the same general trend. There are some outlying points, and this may be a result of the experimental setup, which included a small anechoic chamber. In further testing, the chamber size could be increased and the size of the mounting structure for the transducer could be decreased to reduce stray reflections and give a better approximation of open space. The shape of the analytical pressure profile varies considerably from the simulated and measured profiles. This is due to the fact that the analytical model does not take crosstalk into effect. Activation of neighboring

elements causes constructive and destructive interference in the beam pattern, and leads to the higher and lower pressure areas seen here.

In order to check the analytical model for pressure in the ideal case, in which there is no crosstalk, a simulation was performed on a block with a single transducer in it. The simulation was set up the same way as it was for the transducer array, and the normalized pressure profile is plotted against the normalized analytical pressure profile in Figure 4-31. The shape of the analytical pressure profile is slightly narrower than that of the simulated profile. This trend was also seen in the normalized transverse deflection profiles, and could be improved by calculating pressure using the piezo unimorph model rather than the thin plate model.

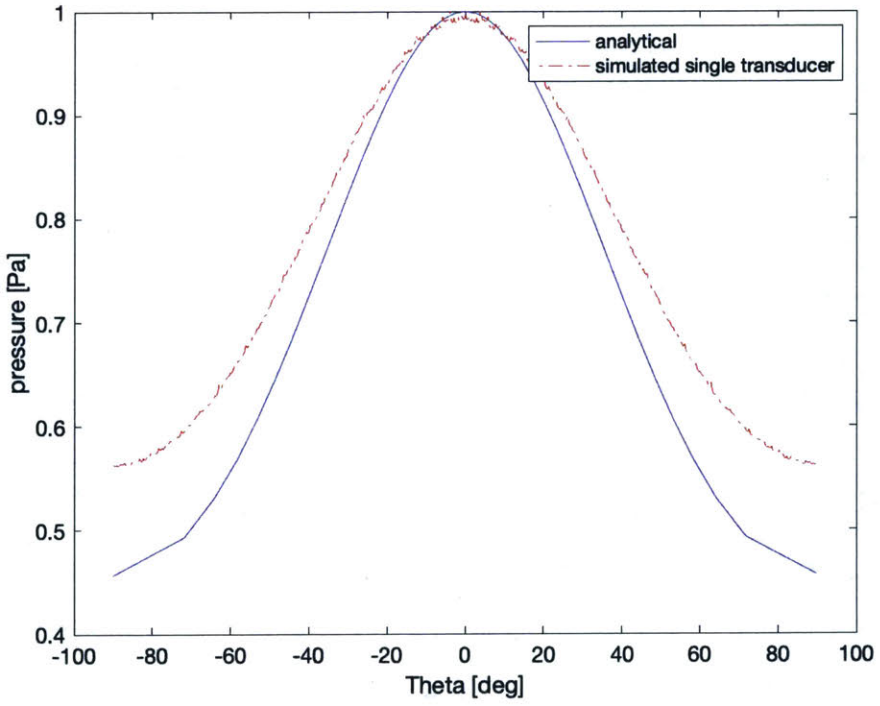

Figure 4-31: Normalized pressure evaluated at a radius of 0.1 m from the center of the transducer array for a block with a single transducer.

4.5.4 Sensitivity

The sensitivity for the analytical, simulated, and experimental results are reported in Table 4.2, rounded to the nearest tenth of a millivolt per Pascal. The analytical, simulated, and experimental results are all within 1 mVpp/Pa of one another.

Table 4.2: Sensitivity

Sensitivity [mVpp/Pa]	
Analytical	0.4
Simulated	0.4
Experimental	0.4

4.5.5 Crosstalk Signals

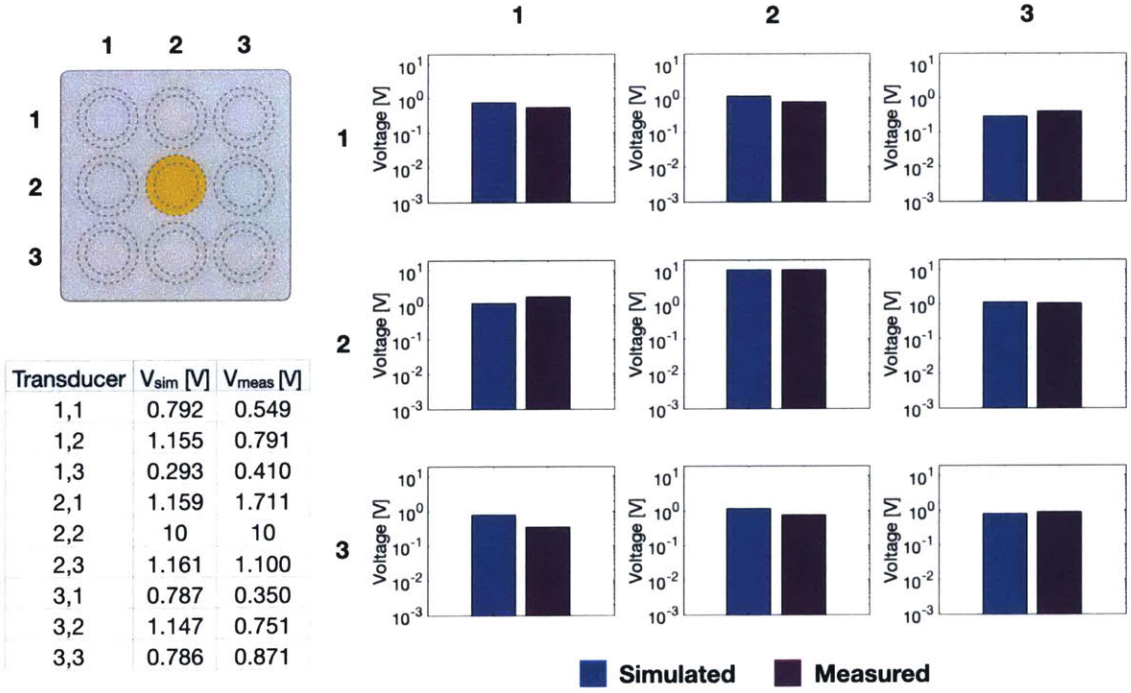

Figure 4-32: Simulated and measured peak voltage crosstalk due to a 20Vpp continuous sine wave across transducer (2,2).

The values of the floating potentials in the simulation are plotted against the measured peak crosstalk voltages in Figure 4-32. The measured crosstalk is 8.2 percent, versus a predicted crosstalk of 9.1 percent. The ratio of the measured to the simulated voltage is, on average, 0.8.

4.6 Crosstalk Reduction

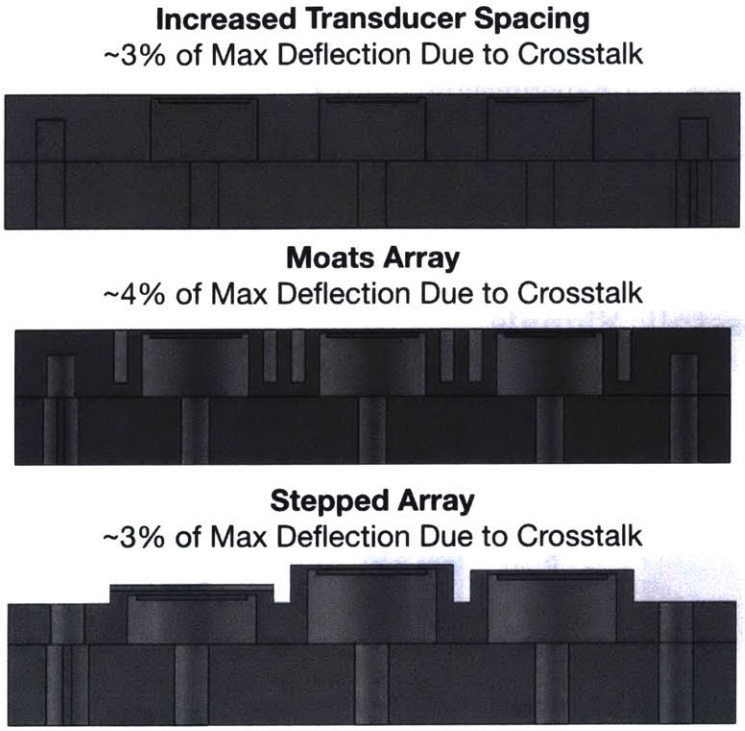

Figure 4-33: Cross sections of three geometries explored for crosstalk reduction. All three have lower crosstalk than the original design, which shows approximately 7 percent crosstalk.

As mentioned previously, there is significant crosstalk between array elements. Crosstalk changes the pressure field produced by the device, making it more difficult to model, and creates a relatively high voltage signal across receiving transducers, making hover signals more difficult to detect. In this section, crosstalk is defined as the ratio of the peak deflection of the passive transducers to the peak deflection of the active

transducer. Three geometries, pictured in Figure 4-33, were explored in COMSOL as possible ways to reduce crosstalk. The first design increases the thickness of the walls between transducers; the stiffer walls should come closer to providing a fixed edge for the membranes. The second design carves out a ring of material around each transducer to reduce physical coupling of vibrations from one membrane to the next. The third design breaks symmetry by moving transducers to different planes and should also reduce coupling of vibrations between membranes.

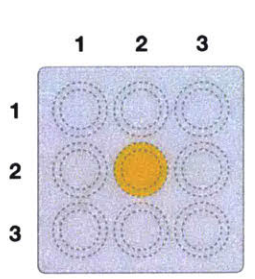

Transducer	δ_O []	δ_{IS} []	δ_M []	δ_S []
1,1	0.059	0.032	0.028	0.030
1,2	0.089	0.031	0.031	0.036
1,3	0.059	0.032	0.028	0.028
2,1	0.090	0.031	0.032	0.037
2,2	1	1	1	1
2,3	0.090	0.032	0.032	0.036
3,1	0.059	0.032	0.028	0.032
3,2	0.089	0.031	0.031	0.038
3,3	0.059	0.032	0.028	0.031

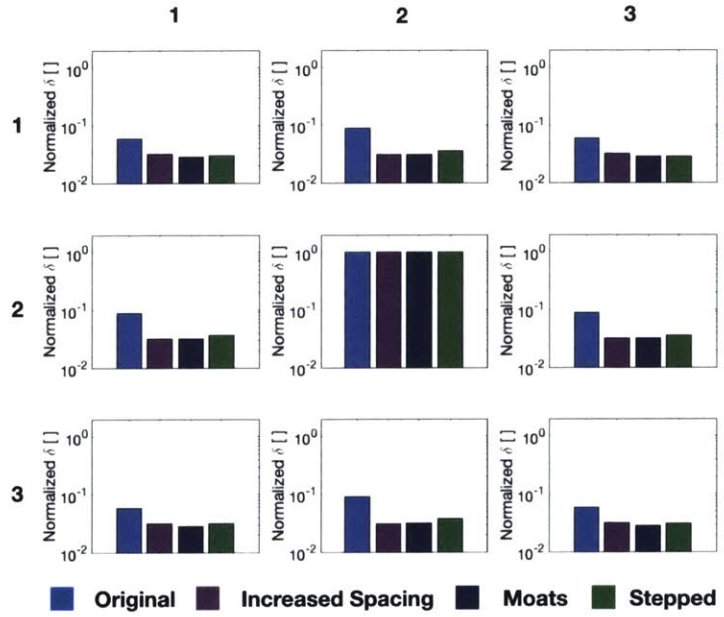

Figure 4-34: Simulated crosstalk for the original geometry and the three proposed geometries, plotted on a semi-log scale. The normalized center displacement of each transducer for each array is shown.

A COMSOL simulation with the full geometry and no air domain was performed for each array. The center element (2,2) was driven with a 20Vpp sine wave and the maximum displacement of each transducer was monitored. A frequency sweep was performed to identify the resonant frequency of the driving element, and the displacement values at that frequency were used to calculate crosstalk. In cases where the frequency response showed two peaks of similar magnitude separated by a few kilohertz, the peak with lower excitation of the passive transducers was chosen. The

normalized displacement results are plotted in Figure 4-34. The array with increased spacing and the stepped array both show approximately 3 percent crosstalk, and the moats array shows approximately 4 percent crosstalk. All three designs are expected to have improved crosstalk compared to the original.

A prototype of each array was built and characterized. The measured frequency response and crosstalk displacements are reported in the this chapter. The measured crosstalk voltages are reported in appendix B.

4.6.1 Array with Increased Transducer Spacing

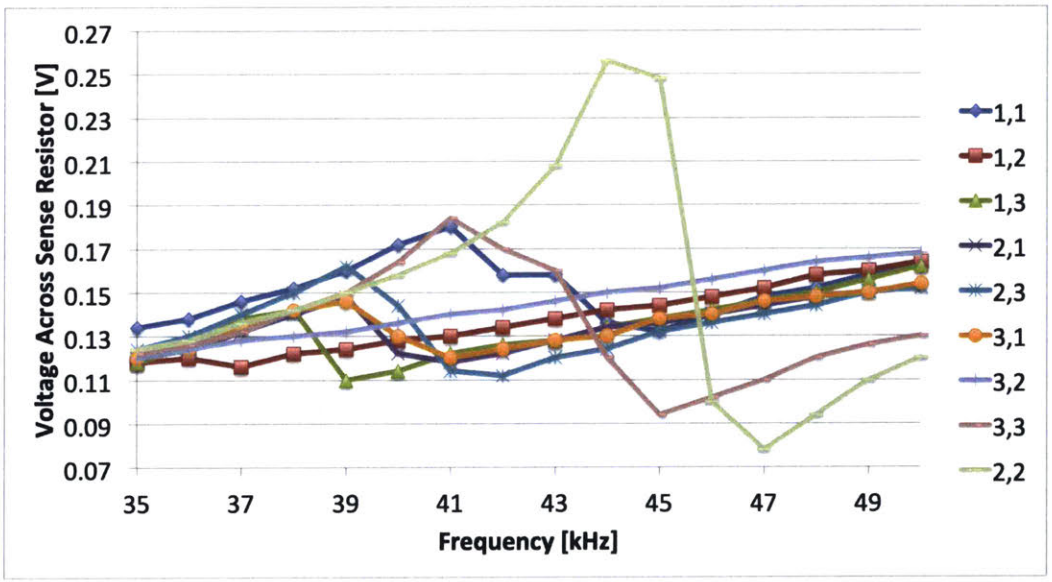

Figure 4-35: Measured frequency response for each transducer in the array with increased spacing.

The frequency response of each transducer in the array with increased spacing is shown in Figure 4-35; two of the transducers, (1,2) and (3,2), don't display a resonant peak. It is assumed that this behavior is the result of a poor epoxy bond, and these two transducers are disregarded in calculations of crosstalk and the ratio of measured to simulated displacement. It is also noted that the resonant frequencies of the individual transducers vary considerably more than they do in the original prototype. The resonant frequency of each transducer is expected to be around 40kHz from analytical results. In the first prototype, the resonant frequencies for

each transducer fall within ± 1kHz of this value. In the array with increased spacing, the resonant frequencies vary from approximately 38kHz to 44.5kHz, a span of 6.5kHz. The variation for the new array is not random; the responses of transducers that are expected to have the same behavior due to symmetry conditions generally resemble one another. As a result, it is hypothesized that the variation in resonant frequency is not due to fabrication defects. It may be that another structural mode is being excited in the array, but this should be investigated further.

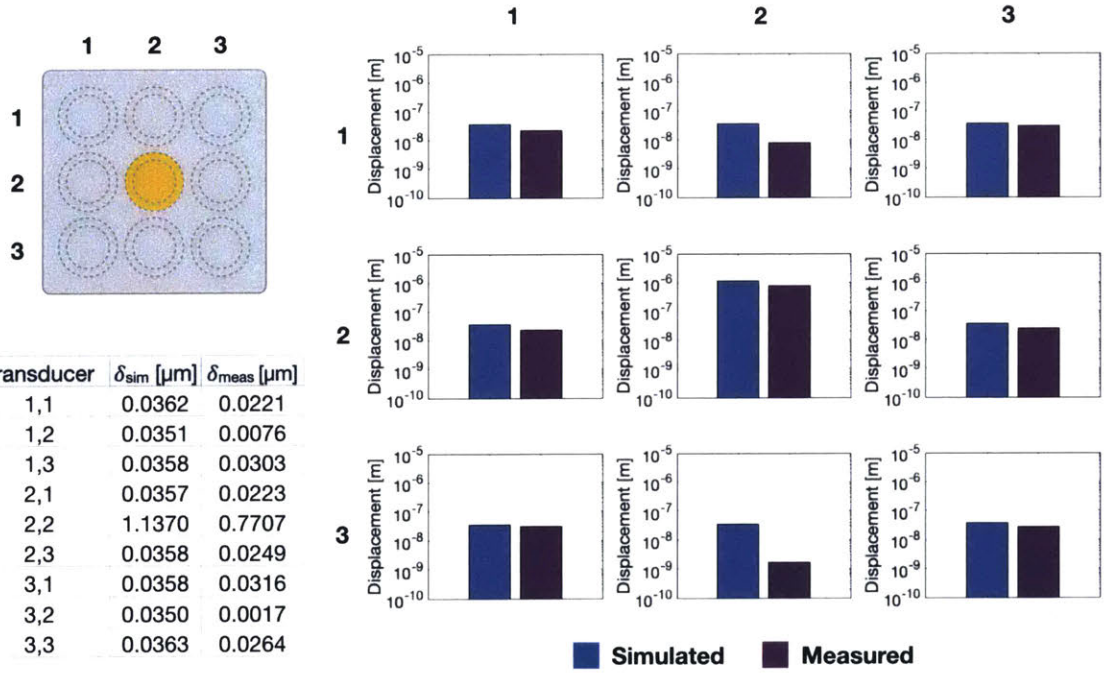

Transducer	δ_{sim} [μm]	δ_{meas} [μm]
1,1	0.0362	0.0221
1,2	0.0351	0.0076
1,3	0.0358	0.0303
2,1	0.0357	0.0223
2,2	1.1370	0.7707
2,3	0.0358	0.0249
3,1	0.0358	0.0316
3,2	0.0350	0.0017
3,3	0.0363	0.0264

Figure 4-36: Simulated and measured center displacements for the array with increased spacing, when transducer (2,2) is driven with a 20Vpp, 44kHz sine wave. The measured average crosstalk, excluding the two non-functional transducers, is 2.9 percent. The average ratio of measured to simulated values is 0.7.

In order to measure the crosstalk as represented by transducer displacement, the array was mounted in the laser vibrometer fixture and transducer (2,2) was driven near its measured resonant frequency with a 20Vpp, 44kHz signal while the surrounding transducers were left floating. The center deflections of all transducers were measured using the vibrometer. The results are shown in Figure 4-36, plotted against the simulated results.

The average crosstalk, calculated using the functional transducers, is approxi-

mately 2.9 percent, which is close to the simulated crosstalk of 3.1 percent. However, as shown in Figure 4-36, the measured deflections are lower than the simulated deflections. The average ratio of measured to simulated values is about 0.7. Possible reasons for this are explored in the discussion section of this chapter.

4.6.2 Moats Array

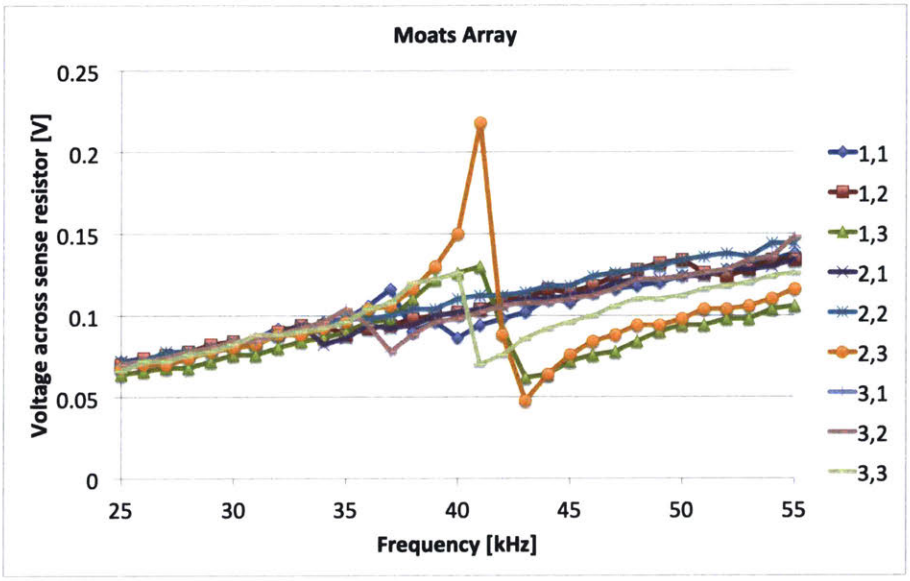

Figure 4-37: Measured frequency response for each transducer in the moats array.

Figure 4-37 shows the frequency response for each transducer in the moats array. As shown, many of the transducers have a linear or nearly linear frequency response with no resonant peak. Only three transducers, (1,3), (2,3), and (3,3), were considered to be functional. These three transducers were used for the calculation of crosstalk and of the ratio between the measured and simulated values. It is hypothesized that the other transducers failed due to a poor epoxy bond. Within the three functional transducers, (1,3) and (3,3) display a much weaker response than transducer (2,3). When measuring crosstalk, (2,3) was used as the driving transducer.

The displacement crosstalk was measured using the laser vibrometer. Transducer (2,3) was driven with a 20Vpp, 41kHz sine wave and the center displacement of each transducer was monitored. The results are shown in Figure 4-38. The measured crosstalk is calculated using (1,3), (2,3) and (3,3) and is approximately 10.6 percent.

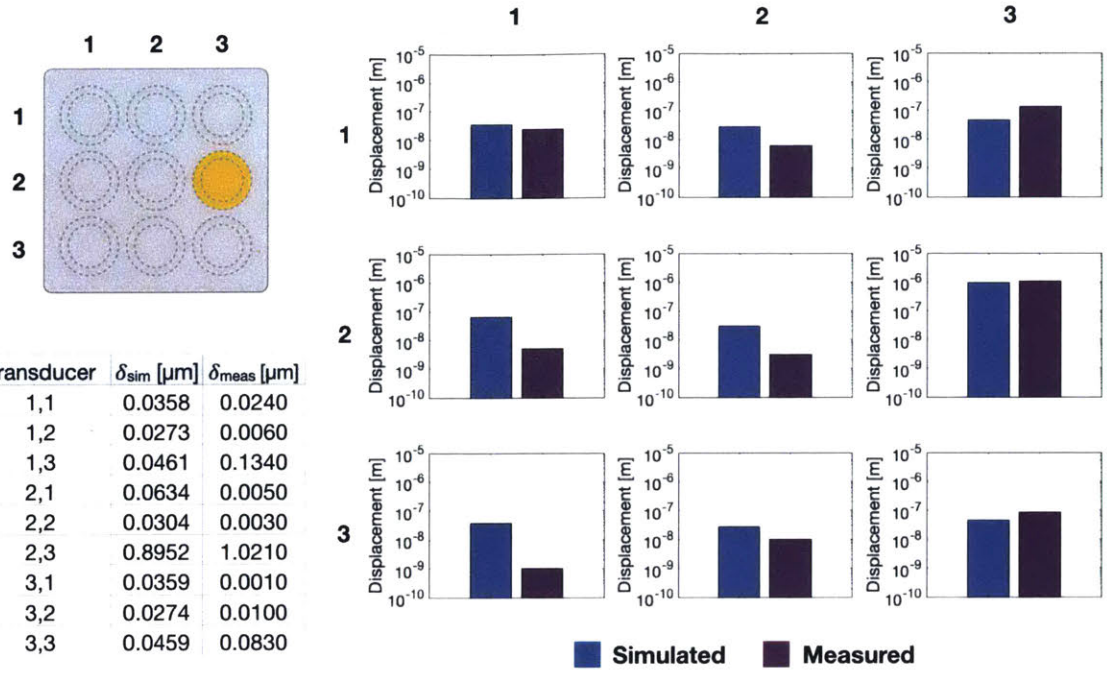

Transducer	δ_{sim} [μm]	δ_{meas} [μm]
1,1	0.0358	0.0240
1,2	0.0273	0.0060
1,3	0.0461	0.1340
2,1	0.0634	0.0050
2,2	0.0304	0.0030
2,3	0.8952	1.0210
3,1	0.0359	0.0010
3,2	0.0274	0.0100
3,3	0.0459	0.0830

Figure 4-38: Measured crosstalk displacement in the moats array. The response was captured by driving transducer (2,2) with a 20Vpp signal at 41kHz and measuring the displacement of all transducers. The electrodes on the neighboring transducers were left floating. The measured crosstalk is approximately 10.6 percent, and the average ratio of measured to simulated values is 2.0.

The ratio of measured to simulated values, calculated using the same transducers, is 2.0.

4.6.3 Stepped Array

The frequency response of each transducer in the stepped array is shown in Figure 4-39. The responses are fairly consistent, with resonant frequencies lying between 39 and 42kHz. The ground electrode on transducer (3,1) peeled off during fabrication, so no voltage data was collected for that transducer. It is also left out of calculations of crosstalk and comparisons between measured and simulated results for the displacement data.

The displacement crosstalk was measured using the laser vibrometer. Transducer (2,2) was driven with a 20Vpp, 41kHz sine wave and the center displacement of each transducer was measured. The results are shown in Figure 4-40. The measured

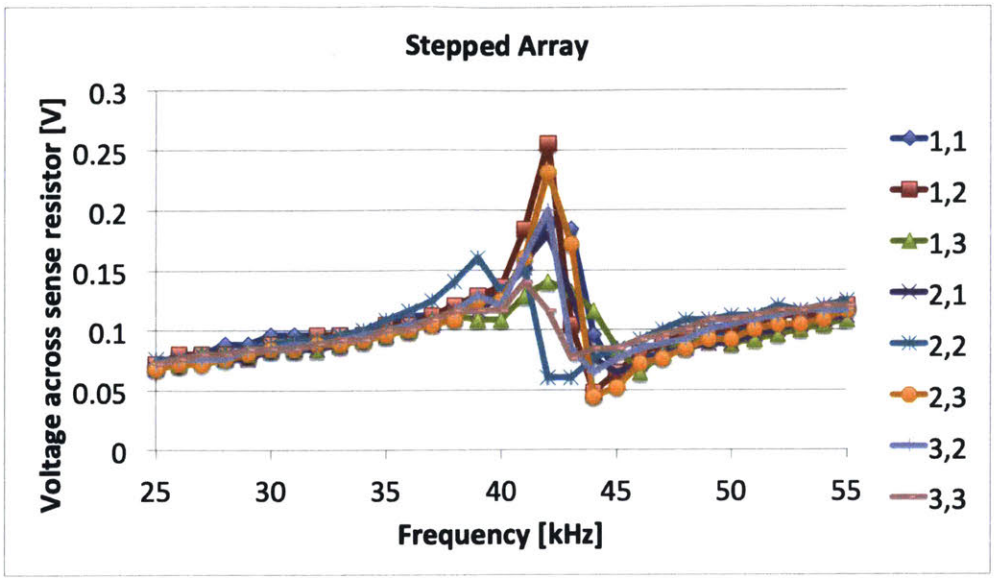

Figure 4-39: Measured frequency response for each transducer in the stepped array.

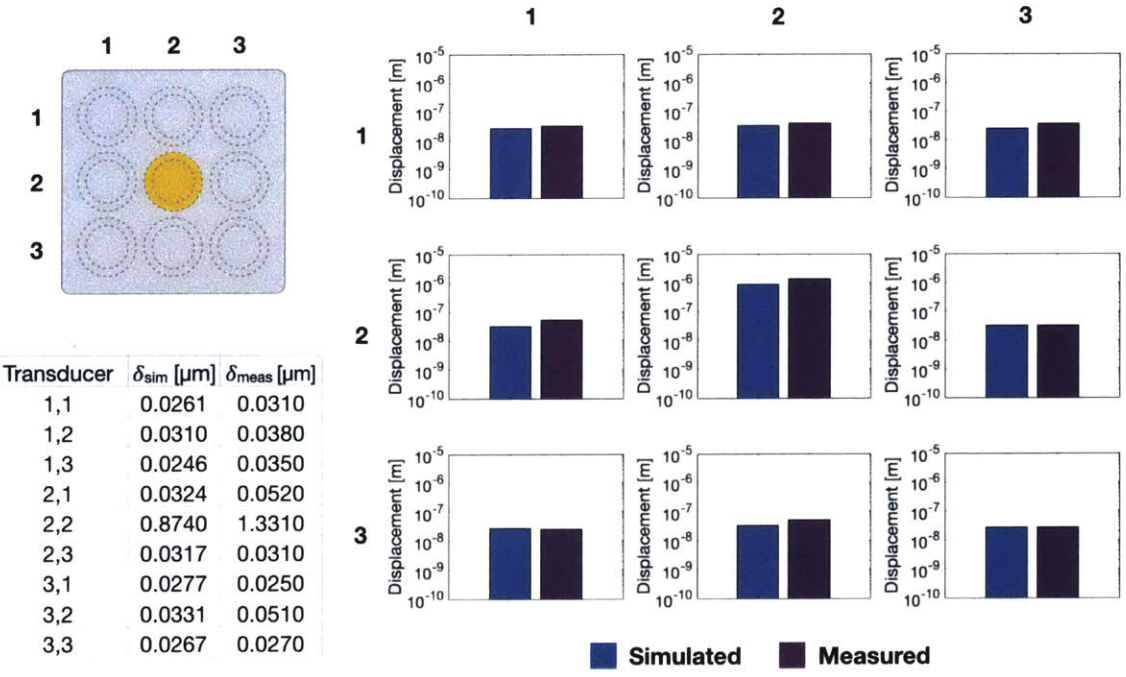

Transducer	δ_{sim} [μm]	δ_{meas} [μm]
1,1	0.0261	0.0310
1,2	0.0310	0.0380
1,3	0.0246	0.0350
2,1	0.0324	0.0520
2,2	0.8740	1.3310
2,3	0.0317	0.0310
3,1	0.0277	0.0250
3,2	0.0331	0.0510
3,3	0.0267	0.0270

Figure 4-40: Measured crosstalk displacement in the stepped array. The response was captured by driving transducer (2,2) with a 20Vpp signal at 41kHz and measuring the displacement of all transducers. The other transducers' electrodes were left floating. The measured average crosstalk is 2.8%, and the average ratio of measured to simulated displacements is 1.3.

crosstalk is approximately 2.8 percent, whereas the simulated crosstalk is about 3.3 percent. The ratio between measured and simulated displacements, calculated using

all transducers except (3,1), is 1.3.

4.6.4 Crosstalk Discussion

The predicted and measured average crosstalk for each type of array is reported in table 4.3. The predicted and measured crosstalk show good agreement for the original (1.4% error) and increased spacing (6.5% error) arrays. The agreement for the stepped array is also reasonable (15% error). Both the increased spacing and stepped arrays reduce crosstalk by greater than 50% compared to the original array. The moats array is also predicted to reduce crosstalk compared to the original design. However, its measured crosstalk is much higher than the simulated value (141% error). This discrepancy is likely due to fabrication errors, and a new prototype should be made. Fabrication errors could also explain the error in the stepped array. More data points should also be collected for each array. Overall, changes to array geometry show promise as a way to reduce crosstalk.

Table 4.3: Crosstalk displacement results.

Array Type	Predicted Average Crosstalk [%]	Measured Average Crosstalk [%]
Original	7.4	7.3
Increased Spacing	3.1	2.9
Moats	4.4	10.6
Stepped	3.3	2.8

It is noted that the absolute displacement varies between the measured and simulated arrays, which is not fully captured in the crosstalk results. The average ratio of the measured to the predicted displacement is calculated for each array type, excluding non-functional transducers, and is reported in Table 4.4.

One possible explanation for this discrepancy is poor representation of experimental damping parameters and boundary conditions in the simulation. In the experiments, the transducer array is mounted to the vibrometer stage using a 3D printed fixture, which clamps the edges of the array, and Blu Tack between the fixture and

Table 4.4: Ratio of measured to simulated displacement.

Array Type	Average Ratio of Measured to Simulated Displacement
Original	0.9
Increased Spacing	0.7
Moats	2.0
Stepped	1.3

the array. In the simulation, the outer walls of the transducer array are considered fixed, an isotropic structural loss factor of 0.05 is applied for the steel domain, and the isotropic loss factor for the epoxy is set to 0.005. This value was chosen by varying the loss factor until the simulation displacements showed good agreement with experimental results for the original array. This approach was followed with the rational that the high structural loss factor for the steel domain could represent the damping from the experimental mounting strategy. It was also assumed that, because the simulation showed good agreement for the first prototype and the mounting conditions were not expected to change considerably, it would hold for the other arrays. Further work should be done to more accurately match the simulated and experimental conditions by changing one or the other.

Chapter 5

Gesture Recognition

5.1 Touch Detection Implementation

The principle for touch detection, as described previously, involves exciting a piezo transducer at or near its resonant frequency and observing the voltage across a sense resistor in series with the transducer as it vibrates. If an object, like a finger, comes into contact with the transducer, a drop in voltage should be observed. There are a few ways to excite the transducers. The transducers could all be driven simultaneously, or they could be driven sequentially at a rate much faster than that of a gesture. For the current system the mechanical crosstalk could also be exploited to excite all transducers in the array by driving one element. The need for only one active element simplifies the circuitry and could reduce power consumption. Exciting the array by driving one element is not a long term solution, as there is a desire to reduce crosstalk for hover sensing, which would reduce the signal to noise ratio for touch detection using this strategy. However, this approach was implemented for proof-of-concept tests in the interest of time.

The circuitry for touch detection is shown in Figure 5-1. A teensy 3.6 microcontroller provides the input signal, which passes through a bridge amplifier to drive one of the piezo disks and a sense resistor in series with it. The gain of the op-amps is adjusted to provide maximum drive signal to the piezo transducer, $\pm$15V. The voltage across the sense resistor is fed into a differential amplifier, the output of which

is fed through a peak detector circuit to produce a DC voltage proportional to the amplitude of vibration of the transducer. The DC voltage is fed into one of the analog inputs of the teensy microcontroller.

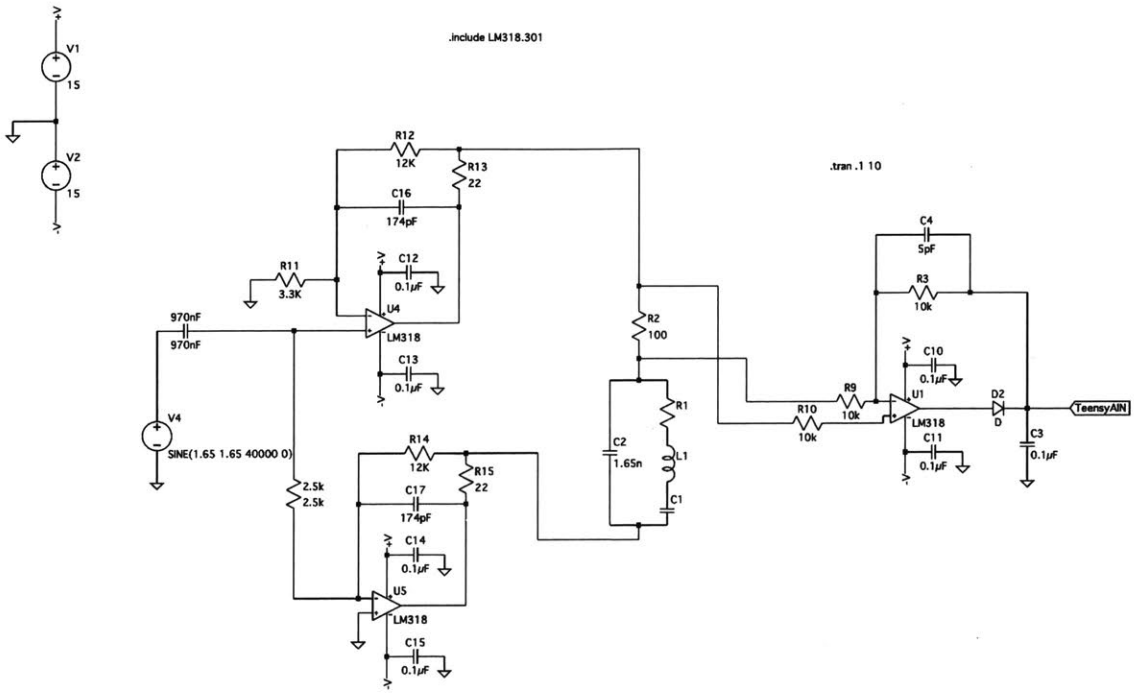

Figure 5-1: Circuitry to drive the active transducer and read the voltage across it.

The remainder of the elements in the array are excited by that same drive signal through mechanical crosstalk between the array elements. The voltage across each of those transducers is also passed through a peak detector circuit. The resulting DC voltage is passed through an op-amp that serves to isolate the signal when passing it into the analog input on the teensy.

Using the circuitry above, a single teensy microcontroller can drive and monitor all nine array elements. The signals from each of the analog inputs are monitored using the Arduino programming language. At the beginning of operation, the average of the peak voltage across each transducer is computed and stored in a static variable. When the current value across one of the transducers drops below a certain percentage of the average value, a touch event for that array element is recognized. The touch detection sensitivity can be adjusted by changing the chosen percentage.

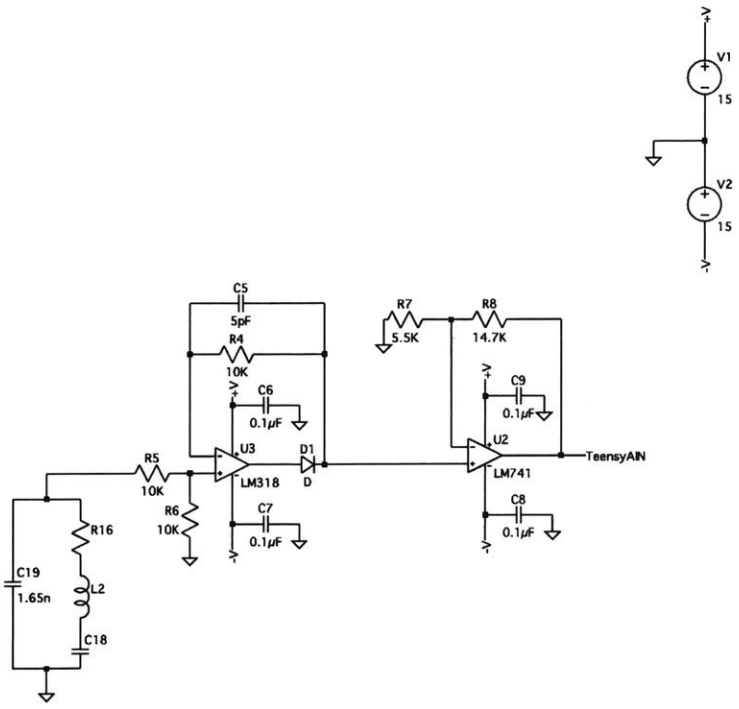

Figure 5-2: Circuitry to read the voltage across each passive transducer.

There is a complication in this method, which is that the voltage across one of the passive resistors can be decreased by touching either the transducer itself or by touching the active transducer. In the current implementation this is addressed by requiring that, in order to trigger a touch event for one of the passive transducers, the voltage for the active transducer must be above the touch event threshold. This allows the system to reliably determine which of nine transducers is being touched.

When a touch event is triggered, the teensy is prompted to record n samples for each transducer. In order to examine the raw data produced by various touch gestures, the values are sent over serial, copied into a text file and then read and stored in an nx9 table in MATLAB. Multiple instances of a particular touch gesture are stored in a structure for ease of comparison. The results for three types of gestures, a touch, a tap, and a swipe, are reported in section 5.3.

The profiles for each gesture type can be used to refine the definition of each gesture and create a prototype real-time categorization method. The prototype works as follows: Once a touch event is triggered, the teensy begins recording samples. For

each pass through the loop, a "current state" array with an entry for each transducer is created. If an element is touched, a number 1-9 corresponding to that element is entered into the current state array. If an element is not touched, the number 0 is entered for that element. After the current state array is filled, the maximum value from the array is added to a "touch log" array of size 1xn. Upon completion of the event, the array is broken into three parts and the mode is calculated for each section and stored in a new 1x3 "gesture" array. Individual gestures can be defined as a 1x3 array and the "gesture" array can be compared to each of those to find a match. For example, a tap event for element 1,1 looks like [1,0,0], a touch event for 1,1 is [1,1,1], and a swipe from 1,1 to 1,3 is [1,2,3].

In order to help new users become accustomed to the touch interface, a graphical user interface (GUI), shown in Figure 5-3, was created using Processing. The GUI shows a line drawing of the array with transducer locations visible. It highlights the current touch location on the figure and reports the transducer label in text below the image.

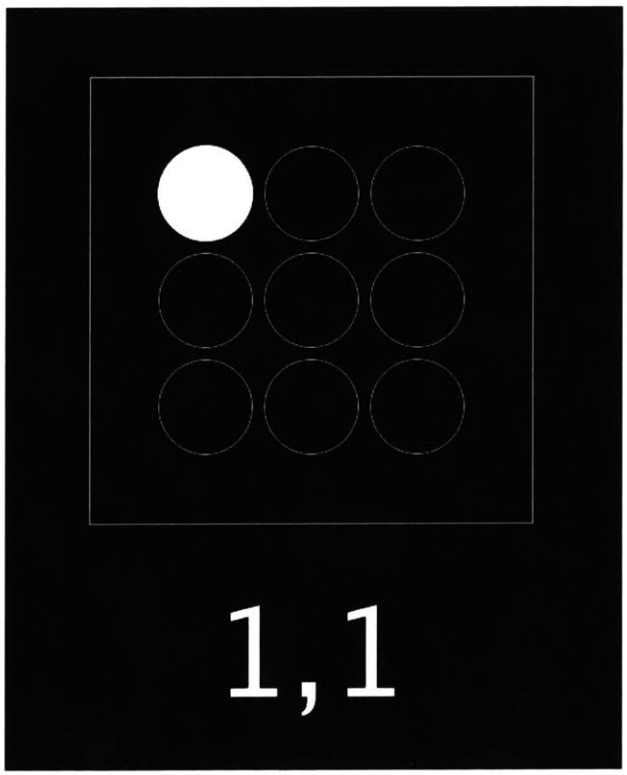

Figure 5-3: GUI for touch interaction.

5.2 Hover Detection Implementation

The ability of the current prototype to detect hover was tested using a function generator, oscilloscope, and the touch circuitry described above. Transducer (2,2) was driven near its resonant frequency by the function generator or touch circuitry, and the voltage across a neighboring transducer was monitored on the scope in two situations: first with no object above the transducer and then with a sheet of acrylic positioned above the transducer, as shown in Figure 5-4. The acrylic sheet was moved from 1 mm above the surface to 3.5 mm in increments of 0.5 mm and the received voltage on transducer 3,1 was measured for three drive levels: 10V, 20V, and 30V. The voltage due to crosstalk, measured when there is no object above the surface, was subtracted from each reading and the modified results are shown in section 5.3.

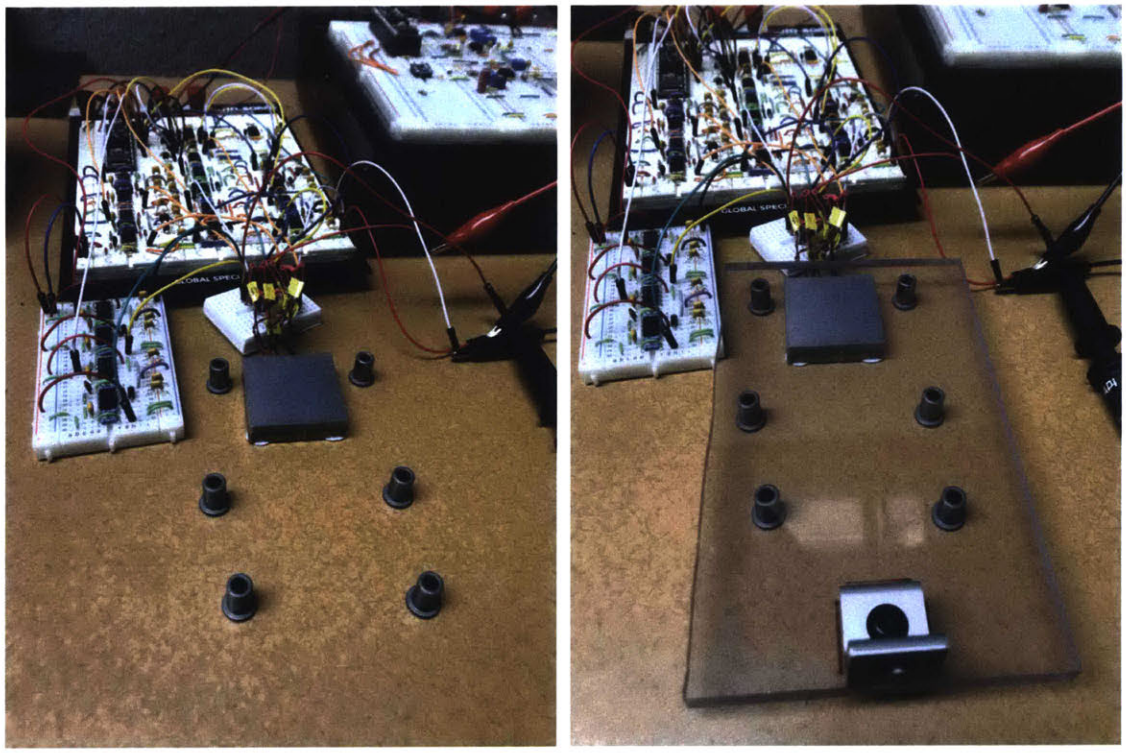

Figure 5-4: Experimental setup to evaluate the applicability of the wave propagation model to the hover system. At left is the transducer with free space above the surface and at right is the transducer with a sheet of acrylic positioned above it.

The current prototype can only detect up to a few millimeters from the surface,

so further hover gestures were not explored with this prototype. There are a few ways to increase the sensing range. The circuitry could be redesigned to allow for a higher operating voltage, which would lead to greater deflection and pressure output. Various materials and backing designs could be explored in COMSOL to increase the source level and sensitivity of the transducer. Methods to reduce crosstalk could also be explored to allow higher resolution measurements of the signal of interest. These steps are discussed further in future work. In the meantime, an approach for hover sensing based on gesture transfer functions was explored using off the shelf sensors as part of a class project and is reported in Appendix A.

5.3 Experimental Results

Preliminary experimental results for touch and hover are reported below. Data for three types of touch gestures, as performed by one user, are presented. Measurements of the proximity of a stationary object are presented for hover due to the limited sensing range.

5.3.1 Touch

Three touch gestures were explored in this prototype: touch, tap, and swipe. As described in chapter 1, a touch gesture is a stationary input with duration greater than 250 ms. A tap gesture is a similar, but shorter duration, stationary input. A swipe gesture involves the user moving their finger along the surface at a velocity between 200 and 500 mm/s. Touch and tap gestures can occur on any of the nine transducers, and swipe gestures include four directions: right, left, up, and down. Within each direction, there are three possible starting locations corresponding to each row or column. Ten instances of each of the 30 possible gestures were recorded. The data was collected from one person performing the gesture, as shown in Figure 5-5. Figures 5-6, 5-7, and 5-8 show an example of the data for each class of gesture.

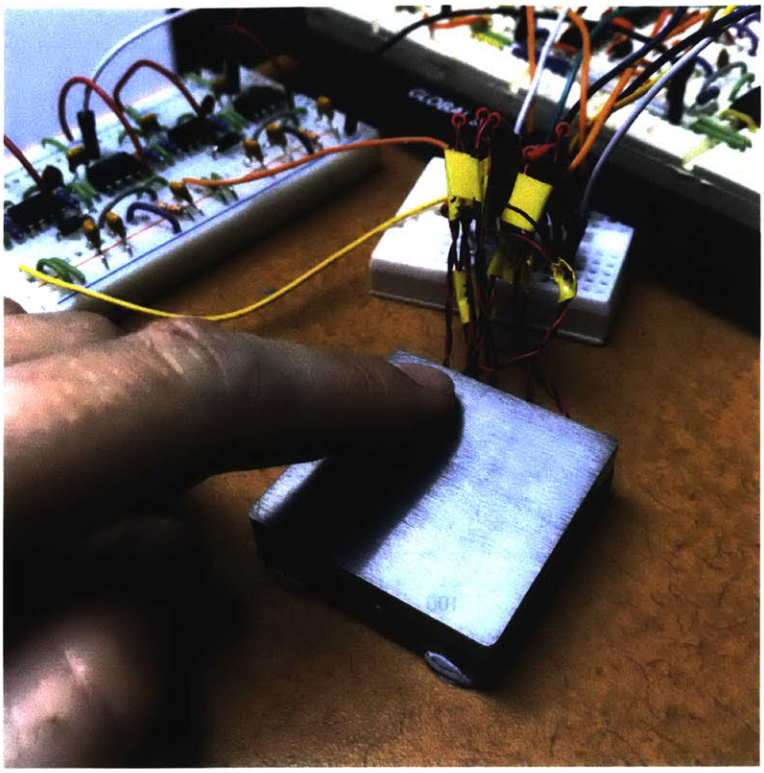

Figure 5-5: Image of a user touching the device.

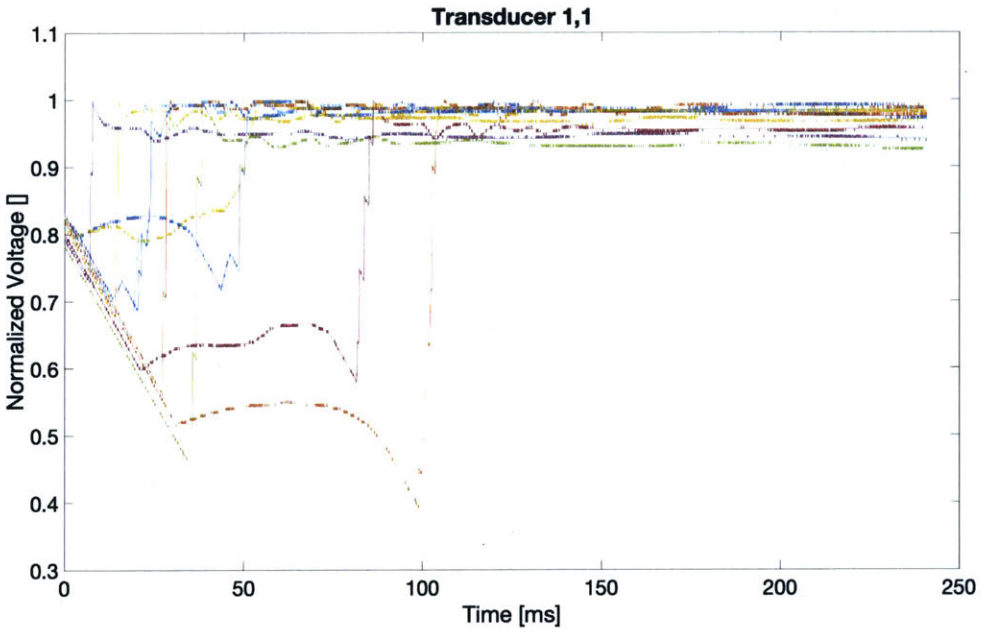

Figure 5-6: Data for ten instances of a tap gesture on (1,1).

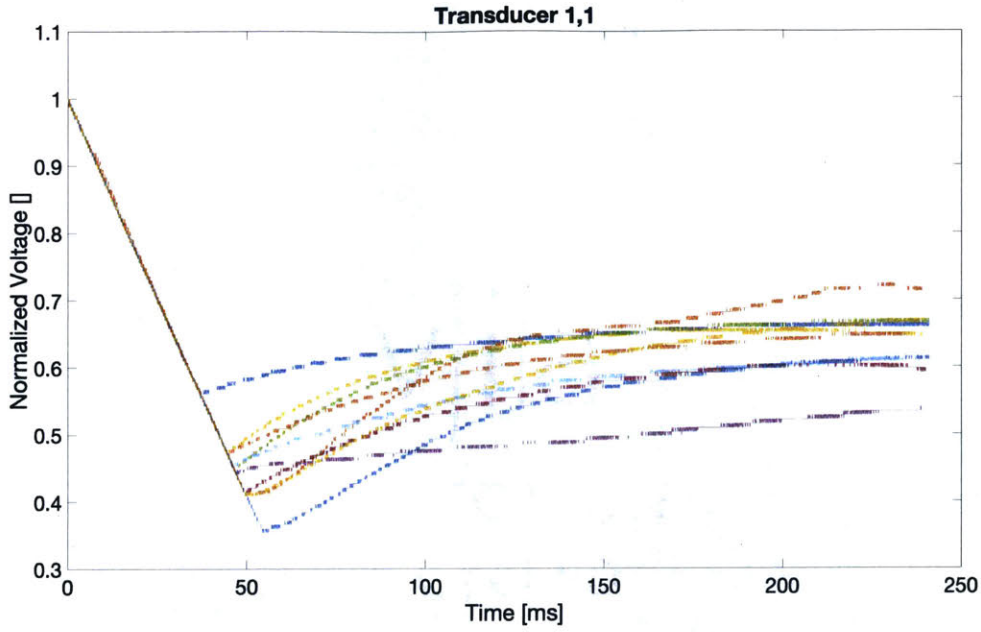

Figure 5-7: Data for ten instances of a touch gesture on (1,1).

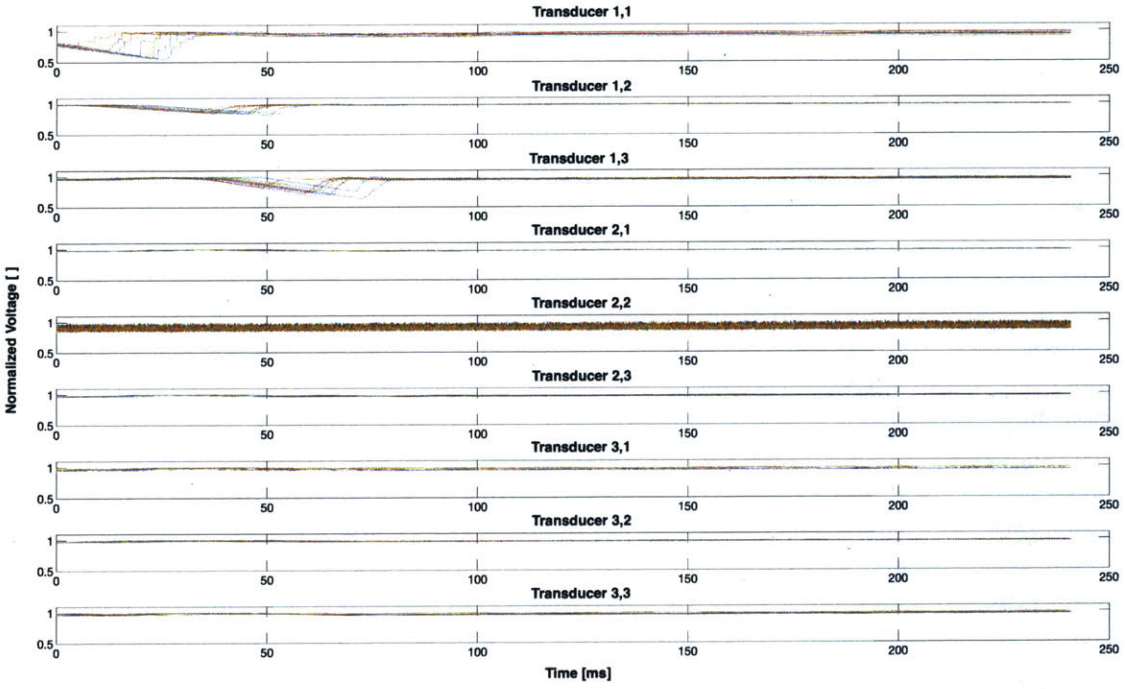

Figure 5-8: Data for ten instances of a swipe gesture from (1,1) to (1,3).

As shown in Figure 5-8, there is little change in the voltage across the transducers

in the array that are not involved in the swipe gesture. The same is true for the tap and touch gestures shown, although the other responses are not plotted. This is beneficial, as significant responses on other transducers could lead to incorrect gesture categorization.

The exception to this behavior is gestures including transducer (2,2), as it is the driving element. Figure 5-9 shows an example of a swipe gesture which passes through (2,2). The neighboring signals could be filtered by start time in order to correctly identify the other two transducers involved in the gesture. It should also be noted that (2,2) shows a difference response profile to the surrounding transducers due to its different circuitry. The responses could be standardized in future iterations.

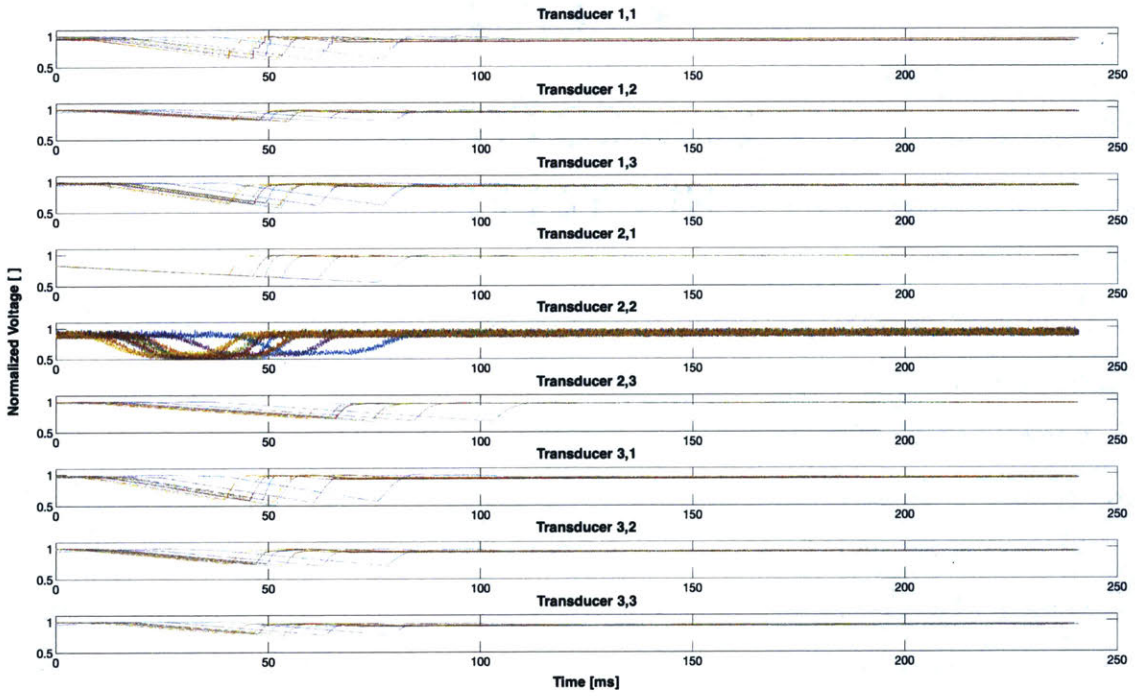

Figure 5-9: Data for 10 instances of a swipe gesture from (2,1) to (2,3), which involves the driving transducer.

5.3.2 Hover

The results from the previously described hover tests are shown in Figure 5-10 and compared to the expected results, which were calculated using the measured trans-

ducer source level and sensitivity and the model for acoustic wave propagation in a hover system.

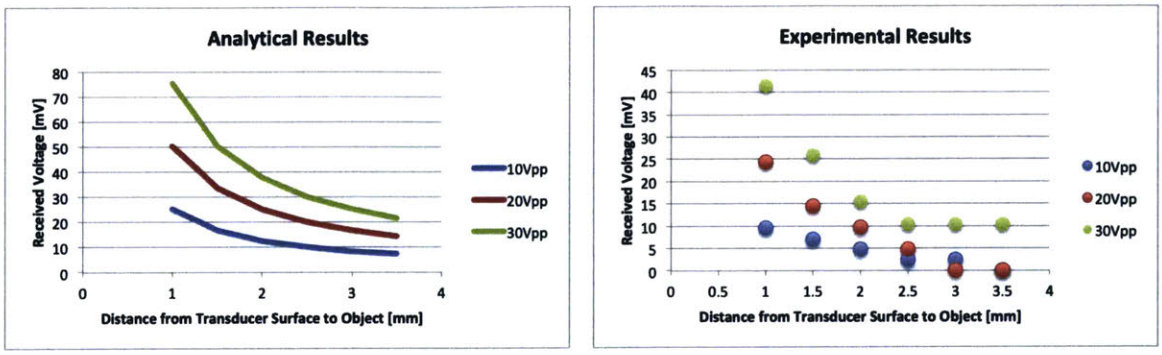

Figure 5-10: Hover data and analytical results at three drive voltages.

The analytical model predicts that the received voltage will increase linearly with drive voltage and will decrease as the reciprocal of the distance traveled, and this behavior is observed in the experimental results. However, the measured voltages are about a factor of two less than the analytical results. There are a few possible explanations for the discrepancy. One is that the model assumes that the received pressure wave has traveled a long enough distance that it can be approximated as a plane wave. However, the object in this test is placed close enough to the transducer that the round trip distance of the pressure wave would not put it in the far field, so the approximation may not be applicable. A second reason is that the transducer is driven with a continuous sine wave, which could lead to some interference between outgoing and incoming waves. In order to eliminate these concerns, a test should be performed with a sinusoidal burst drive signal and an object placed further from the device. However, with the current voltage level the transducer is only expected to detect a signal for object distances up to approximately 5mm, so these tests are left for future work.

Chapter 6

Summary

6.1 Conclusions

In this thesis, a mesoscale piezo unimorph array is proposed as a system to detect touch and hover gestures above metal substrates. Micromachined ultrasonic transducers are explored in literature and in industry as hover detection systems, but they require holes in product shells to operate. Flexural ultrasonic transducer arrays are explored in literature for use as pressure sensors, as transmitters for gas and liquid flow measurement, and as water-coupled ultrasonic imaging systems. This thesis fills a gap in the prior art by exploring the application of mesoscale flexural transducers to gesture sensing. It presents an analytical model, simulation, and experimental results for a prototype array, all of which show good agreement. The prototype demonstrates the capability of the system to distinguish between tap, touch, and swipe contact gestures and to detect objects hovering above the transducer surface at a range of a few millimeters. A comparison with the functional requirements set forth in the introduction is shown in Table 6.1. The prototype meets the requirements of modes (although with a limited range for hover), gestures (for touch), substrate, size, power, and performance specifications (for touch). The desired range for hover was not met, and other functional requirements were not explored in this thesis. Suggestions are made for improvements to touch circuitry and resolution, miniaturization, hover implementation, and fabrication. Potential ways to reduce crosstalk and to

improve the simulation are also discussed and left for future work. The hope is that these suggestions and the simulation and analytical tools presented above can be used as a starting point for continued transducer development.

6.2 Future Work

6.2.1 Touch Circuitry

In the current touch prototype, one active transducer drives the surrounding transducers through mechanical crosstalk. While this simplifies the drive circuitry and lowers power requirements, it leads to additional steps in determining which transducer is being touched and prevents implementation of multitouch gestures that include the driving element. In order to eliminate these shortcomings, new circuitry should be designed that can simultaneously drive and monitor all transducers or that can raster through all transducers at sufficient speed to achieve the same effect.

A simple way to drive all transducers simultaneously using one microcontroller would be to add a sense resistor in series with each transducer and use the circuitry that currently drives transducer 2,2 to drive all 9 transducer and sense resistor pairs in parallel. The voltage across each sense resistor could be read as shown in Figure 5-1. This system was modeled for two transducers in LTspice and the model confirmed that the additional transducer would not change the drive signal or output voltage. The model is shown in Figure 6-1.

If, instead, it was desired to drive each transducer sequentially, a demultiplexer could be used to direct the sinusoidal drive signal to the appropriate transducer. This system could still be driven and monitored by a single microcontroller.

The most flexibility would be provided by a system that could independently drive each transducer and could operate synchronously or asynchronously. Such a system could use nine instances of the circuitry used to drive and monitor transducer 2,2, shown in Figure 5-1. Synchronizing the 40kHz signals between the transducers may be somewhat challenging depending on the controllers used.

Table 6.1: Functional requirements and design parameters with results.

Functional Requirements		Design Parameters	Results
Modes	Touch	Contacting Surface	Successful for touch, limited range (order of mm) for hover
	Hover	2 - 100mm range from surface	
Gestures (for both modes)	Stationary Input	Duration >250ms	Met for touch, requires further investigation for hover once range is improved
	Swipe Input	Velocities between 200 and 500 mm/s	
	Tap Input	Duration <250ms	
Substrate	Solid Metal	Unbroken Surface, Thickness >0.4mm (Al)	Implemented in solid steel (thickness 0.25mm), unexplored for other substrates
	Perforated Metal	Holes or lines with width or diameter < 400 microns	
	Other (Plastic, Glass, etc.)	Unbroken Surface, Thickness of >0.7mm	
Size	Fits in a Small Mechanical Volume	Occupies Surface Area <25 Square Centimeters	Met requirements
		Occupies Thickness <10mm	
Robustness	Works in the Presence of Water Droplets	User Can Still Input Commands	Untested
	Works in the Presence of Rain	User Can Still Input Commands, No Accidental Inputs from Rain Droplets	
	Resistant to Moisture, Water, and Other Contaminants	User Can Still Input Commands	
	Robust to Environment	Not Triggered by Other Objects, Ambient Noise or Light, Motion, etc.	
Form	Works Through Curved Surfaces	Radius of Curvature >7.5mm	Unexplored
Power	Low Power Consumption	<100mW Active	Met requirement (6mW)
Performance Specifications	FOV	$\pm 45^o$	Resolution and SNR acceptable for touch, requires further investigation for hover once range is improved
	Resolution	Spatial Resolution (X,Y,Z): millimeter range (<1cm)	
		Velocity Resolution: <0.1cm/s	
	SNR	20x	
Manufacturability	Easy to Manufacture	Scalable	Unexplored

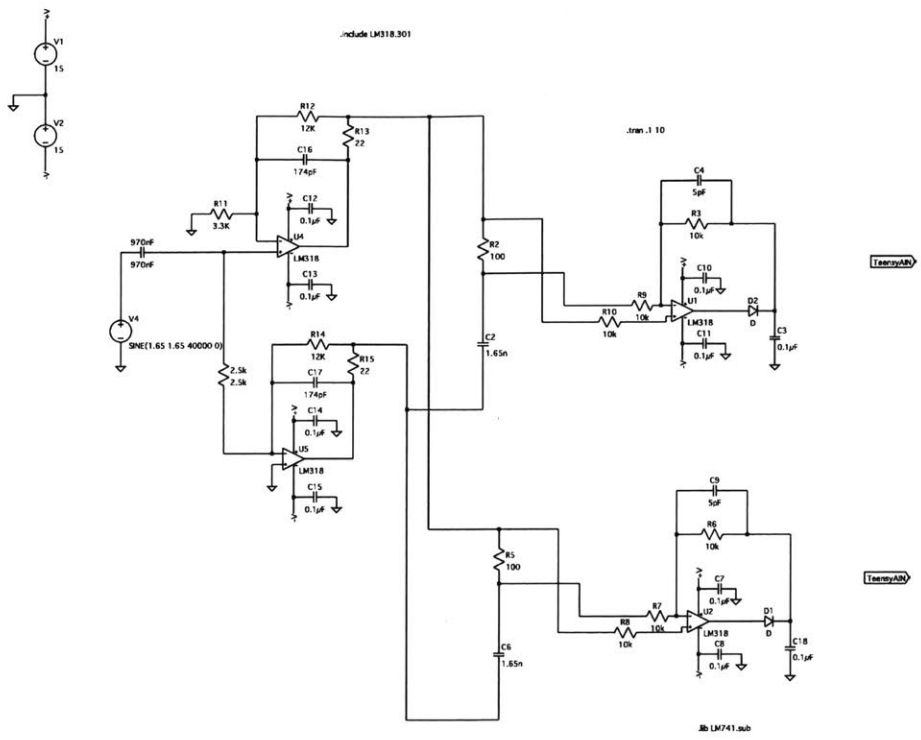

Figure 6-1: Circuitry to drive two transducers simultaneously, as well as read the voltage across their sense resistors. The drive signal and output voltage do not change significantly between this case and the case in which a single transducer is driven and monitored. The transducer is treated as a single capacitor in this test.

In all these approaches, implementing a "wake-up" functionality that would allow the device to switch from a passive mode to an active sensing mode would be helpful in order to save power and prevent unintended inputs.

6.2.2 Improvements to Resolution

In the current implementation of touch detection, each transducer effectively acts as a button with a binary signal for "touched" or "not touched". Therefore, the resolution is directly tied to transducer size and spacing. the resolution is approximately 1cm for the current prototype.

There are two main approaches to improving resolution in the proposed touch sensor. One way is to reduce the transducer diameter and maintain a similar touch detection strategy. There is a significant limitation in this approach because diameter

affects the resonant frequency of the transducer. In order to maintain a frequency of 40kHz and decrease the transducer diameter in the current material, the membrane thickness must also decrease. However, the thickness must be great enough for the structure to withstand impacts, and it is already near its lower bound. Another method would be to change the membrane material, as the resonant frequency is also directly proportional to the square root of the membrane's Young's modulus divided by its density; a change of material may allow a decrease in diameter without changing the resonant frequency or membrane thickness. Another option is to allow an increase in resonant frequency with decreasing diameter. The limitation here is mostly due to control circuitry. Once the frequency approaches several tens of kHz or higher, it becomes difficult to produce a sine wave of that frequency with standard microcontrollers.

The other approach is to maintain the current sensor hardware and change the way a touch gesture is defined from the collected data such that the touch location between transducers can be pinpointed. There is prior art to support this type of approach. In the late 90s, Levy introduced a sub miniature ergonomic keyboard (SMEK) which made use of the concept of passive chording to create $4F^2 - 4F + 1$ keys in an area that would normally support F^2 finger-sized keys. This system, shown in Figure 6-2, worked by assigning one value to each individual key and one value to each intersection of four keys and choosing the size and shape of the keys such that the human finger could actuate a key individually or could depress four at once by pressing on the intersection point. The intersection values could practically be selected by depressing two diagonal keys at the intersection rather than all four, making the system more robust to user error [17]. This approach uses binary keys and could be potentially be applied to a prototype with the current touch detection implementation provided the transducers are sized and spaced such that the human finger can damp the vibrations of one transducer individually or multiple adjacent transducers at once.

Alternatively, the radial and angular location of the contact point along the transducer could be determined by examining the characteristic frequencies and electrical

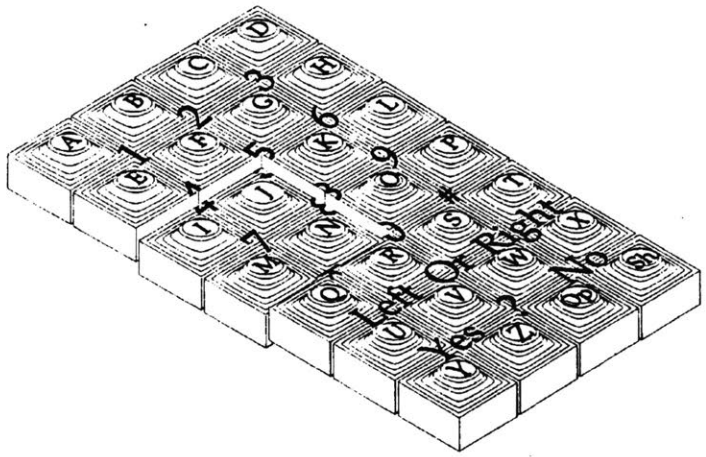

Figure 6-2: Illustration of the sub miniature ergonomic keyboard (SMEK) [17]. The system creates $4F^2 - 4F + 1$ keys in an area that would normally support F^2 finger-sized keys using the concept of passive chording.

input impedance of the transducer, as demonstrated by ACUPAD, Lamberti et al.'s track-pad device based on a piezoelectric bimorph [15]. The authors demonstrate that moving a stylus contact point outward along the radius of the device results in a monotonically decreasing resonant frequency and that moving the point along θ produces a change in the input impedance, although one of the electrodes must be split into four quadrants in order remove electrical symmetry and detect the change in impedance. A similar change could be made to the current prototype to allow it to identify radial and angular location of the finger's contact point.

Using the current hardware, the two approaches from literature could be combined; the radial position for multiple transducers could be used with the concepts of passive chording to define a higher number of positions than are achievable using only passive chording.

6.2.3 Miniaturization

The ability to scale the transducer size would allow this technology to fit in a wider range of products. There are more limitations involved in decreasing than increasing

the current prototype, so miniaturization in X, Y, and Z is discussed in this section. The surface area occupied by the sensors is dependent on the size, spacing, and number of transducers. The size of the transducers is subject to the limitations described previously. The minimum spacing is dependent on the transducer diameter and the wall thickness between transducers, which should not drop below approximately 1mm to maintain wall stiffness and ease of machining. From a hover perspective, the number of transducers needs to be at least two to maintain the potential for non-contact inputs (one could be used if ringing of the transmitter were not an issue) and may require more depending on the complexity of hover gestures and how hover recognition is implemented. From a touch perspective, one transducer could potentially support tap, touch, and swipe gestures with some of the changes described above to increase resolution. More complicated gestures, including multitouch, would likely require more transducers, as would the current gesture suite implemented with the current touch detection strategy.

The thickness depends on the thickness of each transducer. More work needs to be done to model the effect of wall height, backing layer thickness, air cavity dimensions, and potential fill materials in order to understand the thickness limitations on the device. These parameters will likely depend on the membrane thickness, which is limited by the material thickness required to withstand drop impacts in a consumer product. This thickness is approximately 0.4mm for aluminum or less for steel, and can be used as a starting point to determine the minimum thickness of the overall device.

6.2.4 Hover Implementation

As mentioned previously, the current prototype can only detect the presence of hovering objects out to a few millimeters. In order for hover gesture recognition to be feasible, the range must be increased to at least around 50 mm.

One way to do this would be to increase the drive voltage, which would increase the pressure output from the transducer. The pressure output is predicted to be linearly dependent on voltage, which has been verified experimentally up to 30 Vpp.

The piezoceramic disks used in the current prototype are rated for 5-7 VAC per mil, so at a thickness of 0.3 mm they can handle up to approximately 60 Vpp. Assuming the linear trend continues and assuming a noise floor of approximately 4 mVpp, the transducer operated at 60 Vpp should be able to detect the presence of an object up to a distance of around 38 mm. This estimate was performed by finding the distance at which the analytical model predicts a received voltage of the noise floor. In reality, it might not reach this range. The current prototype, operated at 30 Vpp, is expected to sense out to 12 mm before crossing the noise floor, but the signal levels off around a few millimeters. Should it work according to the analytical model, there are a few caveats for this approach. First, 38 mm still is still less than the desired range, and 4 mVpp does not give a good signal to noise ratio. Second, the linear trend between voltage and pressure is expected to break at some point, and it should be tested experimentally whether that point occurs after 60 Vpp. Finally, if the technology is to be used in consumer electronics devices, it is generally desirable that the voltage does not reach this level.

An alternate approach to increasing pressure output would be to drive all transducers simultaneously to generate a plane wave or to drive multiple transducers with delays to beamform. Either drive strategy could be accomplished by the independent drive circuitries described in section 6.1.1. The plane wave approach could also use the version of the circuitry in which all transducers are driven in parallel, and the beamforming approach could use the circuit with the demultiplexer.

6.2.5 Improvements to Fabrication

During fabrication, there were many instances in which one or more transducers in an array exhibited a linear or diminished frequency response, as shown in Figure 4-35. It is hypothesized that the cause of this behavior is a poor epoxy bond. For this prototype, glass microspheres were mixed into the epoxy to set the bond height, and the mixture was spread across the piezo disks before they were placed onto the vacuum fixture using tweezers. A 1kg weight was used to hold the assembly together as the epoxy cured. Issues with the density of the microspheres, the amount of epoxy

applied, or the consistency of the coat could explain the diminished frequency response on some of the transducers. The use of a tape-type epoxy, as used in manufacturing of PCBs, or of different methods for dispensing liquid epoxy could be explored to improve consistency in the fabrication process.

Additionally, there was one transducer in which the ground electrode peeled off of the piezoceramic disk after a ground wire was tugged after soldering. In the future, some strain relief should be applied during the soldering process. Alternatively, other types of contacts could be used, such as PCB spring contacts, which could also make the assembly process less labor intensive.

6.2.6 Crosstalk Reduction and Simulation

In previous sections, a few different array geometries were explored as ways to reduce crosstalk. The simulation predicted that all three proposed geometries could reduce crosstalk in the array, and the experimental results showed that the increased spacing and stepped arrays decreased crosstalk by over 50% compared to the original array. The moats array did not show decreased crosstalk, but it is assumed this was due to fabrication errors.

However, the absolute deflection varied between the simulation and the measurements. It is expected that this has to do with the way the system damping parameters and boundary conditions are modeled. More work should be done to explore where the discrepancy comes from and adjust the COMSOL model or experimental setup accordingly. Additional geometries, along with various transducer constructions and backing materials, should also be investigated.

Active crosstalk suppression could also be explored. This approach would apply a phase shifted voltage to either the driving transducer after the main burst signal or to surrounding transducers during the main burst signal to cancel vibrations caused by crosstalk.

6.2.7 Robustness

One of the important functional requirements which was not addressed in this thesis is robustness to environmental inputs, like water droplets, rain, moisture, noise, motion, or other objects in the area, among other things. In order to assess the practicality of this sensor design for touch and hover sensing in a consumer electronics product, or in other applications, these factors should be investigated.

Appendix A

Hover Gesture Recognition

An Acoustics Sensing Method for In-Air Hand Gesture Detection

J. Canning, J. Carrus, A. Cobi, B. Colson, W. Harvey
Mechanical Engineering
MIT
Cambridge, MA USA

***Abstract*—Motion detection is widely used as a form of feedback in control systems in numerous applications. Specifically, gesture detection has numerous use applications in mobile devices and smart devices. This paper outlines an acoustic method by which the transfer functions of the transducers and hand gestures can be computed in order to do system identification. A 40 kHz ultrasonic transmitter is used in conjunction with an array of receivers in order to do gesture identification. Initial results show that the transfer function of the ultrasonic transducers can be computed and fitted with a five-parameter analytical model with 99.2% Variance Accounted For (VAF). The hand gesture transfer function was computed for three gestures: no hand present, horizontal hovering hand, and vertical hovering hand. The system was able to correctly distinguish the gestures in even moderate ambient noise.**

Keywords—acoustics, ultrasonic, piezoelectric, consumer electronics, gesture sensing

I. Introduction

In-air gesture detection has applications in numerous fields and products. The engineering of faster and smaller microcontrollers has allowed for small, everyday objects like cell phones, keys, and wearables to become "smart" devices: devices able to communicate with other devices and humans. [1] Smart devices have allowed people to have more control over them, including control through non-contact methods. As technology of smart devices advances, an important question arises: what additional capabilities can be fit inside these objects to make them usable by anyone, regardless of physical capability? Some examples of non-contact methods of interacting with smart devices are voice recognition, face recognition, and gesture detection.

This paper explores a method of performing in-air hand gesture detection through ultrasonic sensing. Acoustic sensing has advantages for gesture recognition in mobile devices, as it requires less power than optical methods and is unaffected by lighting conditions. [2] Ultrasonic sensing is the preferred method of acoustic sensing because it operates at frequencies above the audible range, which makes it ideal for consumer products.

II. System Design and Prototype

The system, outlined in this section, consists of one ultrasonic transmitter (Murata MA40S4S), a human hand, and an array of receivers (Knowles SPU0410LR5H-QB-7). Additional circuitry to generate the input signals and to process the output signals is outlined below. The overall block diagram of the system is shown below.

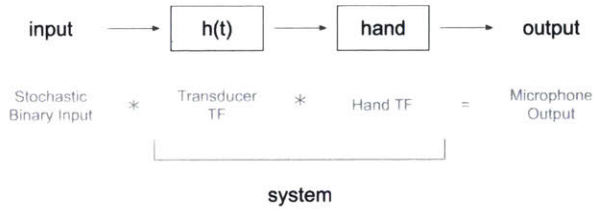

Fig. 1. Block diagram of the system setup.

A. Transmitter

A Murata MA40S4S ultrasonic transmitter, with a resonant frequency of 40 kHz, was used to generate an acoustic signal. This specific transmitter was chosen because it generates frequencies well above the audible range.

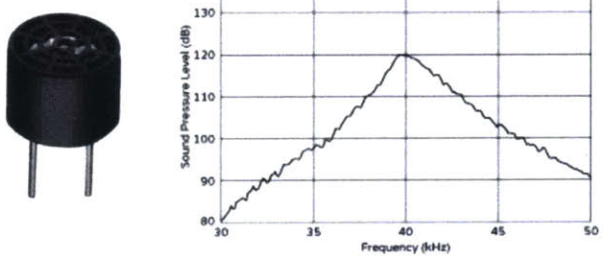

Fig. 2. Murata MA40S4S ultrasonic transmitter and frequency response curve.

B. Receiver Array

A MEMS microphone (Knowles SPU0410LR5H-QB-7) was used to generate an output signal from the system. To allow for beam-forming capabilities [2], an array of 49 receivers was used. For the purposes of this paper, beam-forming was not used, and data from only a single receiver was used to demonstrate the system identification capabilities. A custom four-layer printed circuit board (PCB) with an array of 7 x 7 receivers was designed and sent out for fabrication. The PCB was assembled in-house, under a microscope, and tested with a multimeter to ensure proper electrical connections.

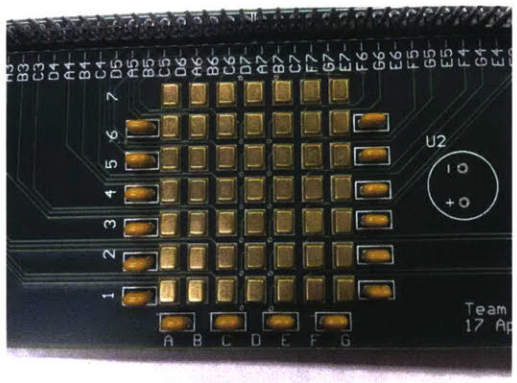

Fig. 3. Receiver Array mounted on custom PCB.

C. Hand Gestures

The primary hand gestures that were used for the system were "horizontal hand" (0 degrees) and "vertical hand" (90 degrees). To complete the experimental system, these gestures were performed above the PCB. A diagram showing the system setup is shown in Fig. 4.

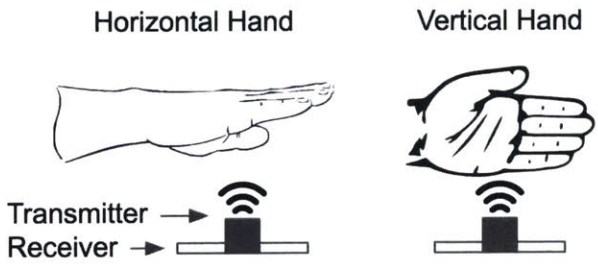

Fig. 4. Diagram of sensing experimental setup.

D. Input Circuit Topology

The input to the system was a signal generated to drive the ultrasonic transmitter. The signal was generated by a computer and then sent to a Teensy 3.6 microcontroller. The microcontroller then drove the transmitter through a low power audio amplifier (LM386) with a high pass filter. A diagram of the input signal circuit topology is shown in Fig. 5.

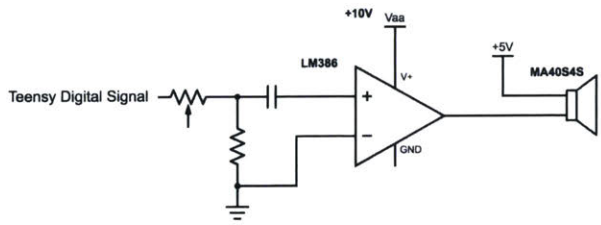

Fig. 5. Schematic of transmitter driver circuit.

E. Output Circuit Topology

The output signal generated by the receivers was amplified via an operational amplifier (LM318) and biased to a 0-3.3V signal. This signal was sampled with a 12-bit ADC (Texas Instruments ADS7886) at a sample rate of 600 kHz and communicated to the Teensy via SPI. The gain was adjusted manually via a potentiometer to use the full range of the ADC. The topology of the output signal circuitry is shown in Fig. 6.

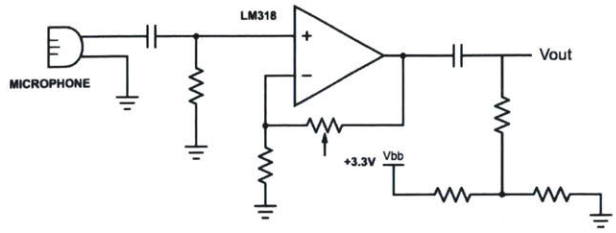

Fig. 6. Schematic of receiver circuit.Vout is sampled by the ADC.

The 600 kHz sampling rate is appropriate for the frequencies in this system as shown in Fig. 7 that details a small sample of the microphone's output.

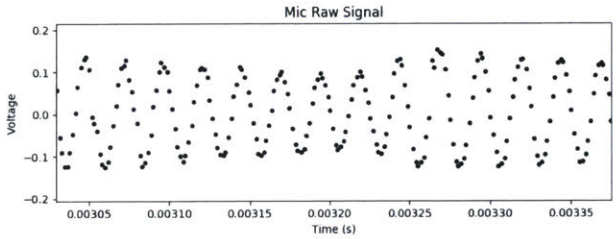

Fig. 7. The microphone raw signal.

III. Experimental Setup

In this section, we outline the setup used to perform experiments and gather data, in order to then do signal processing to distinguish between different hand gestures. We call this ability to distinguish between hand signals System Identification (System ID). A block diagram of the experimental setup is shown in Fig. 8.

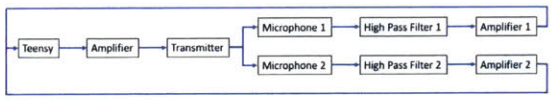

Fig. 8. Block diagram of system for generating and receiving signals.

A. Experiment 1: Determining Impulse Response of Transmitter

For this experiment, the transmitter was positioned directly above the PCB, pointing toward the microphones. The input to the system was a stochastic binary signal. An image of the experimental setup is shown in Fig. 9.

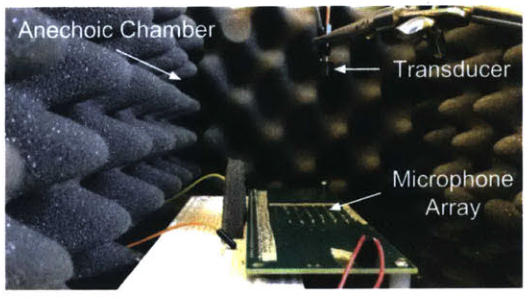

Fig. 9. Transmitter characterization experimental setup.

B. *Experiment 2: System Response to Horizontal Gesture*

For this experiment, a horizontal gesture was used. In order to obtain repeatable results, a (165mm x 100mm x 9mm) piece of acrylic was mounted to a fixture next to the transmitter-receiver set-up and used to mimic a human hand. This was useful to eliminate variance in the signal due to unsteady human hands for initial system characterization. An image of experiment 2 is shown in Fig. 10.

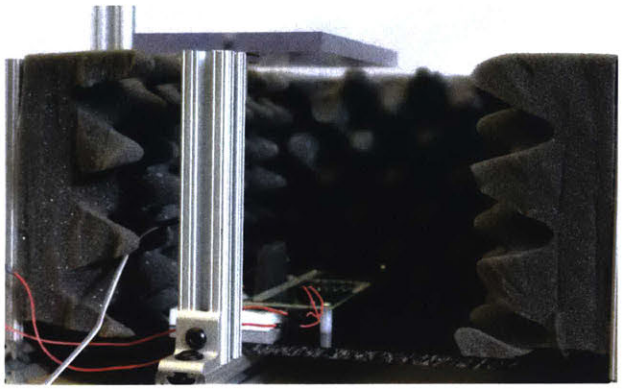

Fig. 10. Horizontal gesture experimental setup.

The height from the PCB top surface to the reflective surface (bottom of the acrylic) was measured to be 135 mm. The input to the system is again a binary stochastic signal.

C. *Experiment 3: System Response to Vertical Gesture*

For this experiment, the same piece of acrylic was used but in the vertical configuration, rotated 90 degrees relative to the sensor setup. The height from the PCB top surface to the bottom-most surface of the acrylic was measured to be at 66 mm. An image of experiment 3 is shown in Fig. 11.

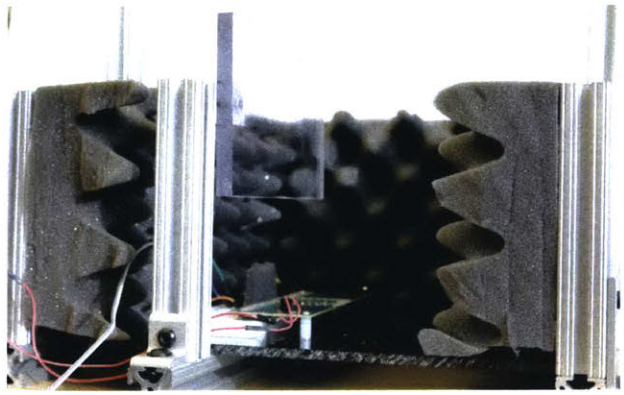

Fig. 11. Vertical gesture experimental setup.

IV. Signal Processing and Results (System ID)

After experimental data was acquired, various signal processing techniques were used to identify the system's characteristics. For each of the three experiments, the same input and output analog circuits were used. However, for the digital signal processing and system ID, different techniques were used, which are outlined in the following sections.

A. *Digital Signal Processing*

For Experiment 1, the transfer function of the transducer system was discovered by deconvolving the input autocorrelation function from the input-output cross correlation function using Fourier techniques. This method improves noise immunity over simply dividing the output fft by the input fft. The system may also be discovered via Toeplitz matrix inversion, but a 10x system speedup was observed when FFT methods were used, due to the already highly optimized FFT libraries. [3,4] The specific method is outlined in equation 1, where fft* denotes the complex conjugate of the fft.

$$h(t) = \text{ifft}\left(\frac{\text{fft}(y)\cdot\text{fft}^*(x)}{\text{fft}(x)\cdot\text{fft}^*(x)}\right) \quad (1)$$

The resulting transfer function for the transmitter was then fitted to a parametric model with 6 parameters. This model was able to account for 99.2% of the variance in the data. The model is shown in equation 2 where a is a static gain, t_d is a pure time delay, τ_1 and τ_2 are exponential time constants, ω is an oscillatory frequency, and ϕ is a phase shift.

$$y(t) = ae^{-(t-t_d)/\tau_1}(1-e^{-(t-t_d)/\tau_2})\sin(\omega(t-t_d)+\phi) \quad (2)$$

The resulting system response and model fit is shown in Fig. 12.

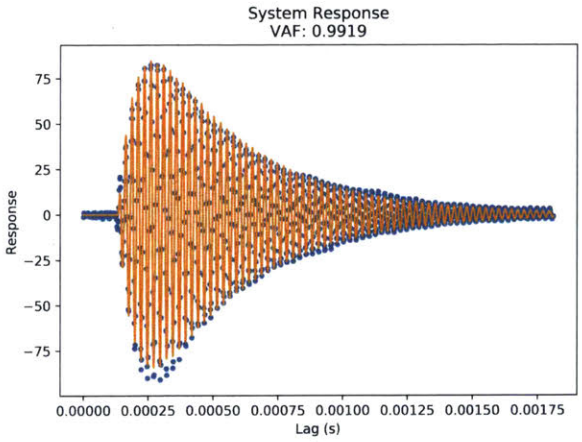

Fig. 12. Experimentally determined impulse response of ultrasonic transmitter.

The system oscillated as expected, and the smaller oscillations are consistent and centered about 40kHz. The system transfer function was further validated as the gain portion of the bode plot corresponds well with the bode plot supplied in the datasheet of the transducer, as seen in Fig. 13.

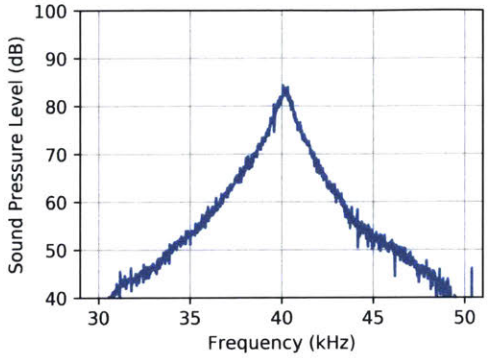

Fig. 13. Measured gain portion of the bode plot for the ultrasonic transmitter. It is in agreement with the manufacturer supplied data (Fig 2), except we observed a lower response at frequencies above 40 kHz. Absolute differences in sound pressure level are due to a different driving voltage as well as the physical separation of the transmitter to the receivers.

There still remains variance unaccounted for by the model. In an attempt to better understand this variance, the model was used to predict the output of the experiment and the nonlinearity was visualized by cross-plotting the predicted response against the measured values.

If a static nonlinearity was present in the system, Fig. 14 should show a trend corresponding to this static nonlinear transformation.

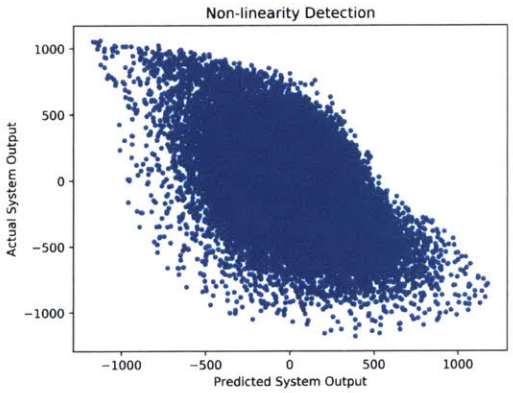

Fig. 14. Nonlinearity is not included in the transmitter system model.

No visible trend was present, though a hysteresis loop could be a potential explanation for this behavior. Piezoelectric materials exhibit hysteresis nonlinearity, but usually this is only significant at higher driving voltages. [5] Further analysis was not pursued.

For experiment 2, detecting a horizontal hand gesture, the hand system was discovered by using the same strategy as previously described, however, the already known impulse response of the transducer was convolved with the binary stochastic input signal prior to system discovery to eliminate the influence of the transducer system on the discovered hand system. The resulting system shows two distinct echos and is shown in Fig. 13.

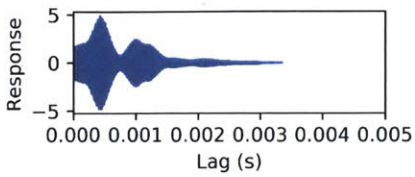

Fig. 15. System response for horizontal hand system.

This process was repeated for experiment 3. The vertical hand system features a single reflection of lesser magnitude than the horizontal hand as seen in Fig. 16.

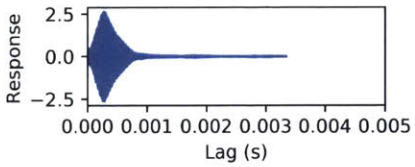

Fig. 16. System response for vertical hand system.

B. Phase 3: Gesture Classification

The next step was to then classify these hand systems into gestures. Several techniques were considered including a model fit, bulk statistical measurements, and a neural net algorithm, but distinguishing between a simple vertical and horizontal hand could easily be done by looking for the intensity of an echo in the hand system.

The simplest method for making this classification was to use a discrete Fourier Transform to identify the amount of frequency content within a range that was reasonable for an echo at a distance of 100-200mm. Statistics for this parameter, well represented by the gain of the 500Hz "bin" of the discrete fourier transform, in each of the positions are shown in Table 1. It is important to note that these values are for 100 trials of each gesture with a human hand performing the gesture as opposed to our acrylic phantoms.

TABLE I. GESTURE CLASSIFICATION THRESHOLDS

Gesture	Mean	Std. Deviation
No Hand	0.5	0.2
Vertical Hand	6.1	2.4
Horizontal Hand	13.9	3.0

Table 1. Summarized results of 100 experiments identifying the hand gestures.

These statistics show an acceptable separation that allows for a suitable level of classification with a simple characterization routine that uses a series of thresholds to categorize different gestures.

V. Future Work

Future work on this project includes the expansion of identifiable gestures through more advanced gesture classification techniques. Additionally, using the signals from multiple microphones to generate additional information for the gesture classification system to use will improve the sensitivity of our system to different, more nuanced, gestures. Finally, the system should be miniaturized for productization. None of the components are inherently large and should be able to easily be integrated into a much smaller package. Furthermore, the current transmitter could be replaced with a different transmitter, provided that the new transmitter could be easily sampled. Using existing signals in the environment as the transmitter for passive sensing could be an area for future exploration.

VI. Conclusion

This paper introduces and outlines a method to do in-air gesture detection through ultrasonic sensing. It was shown that simple binary gestures, like hand angle above sensor array (0 degrees or 90 degrees) were successfully distinguished. The authors also outlined a set of critical parts including a microcontroller, a transmitter, and receivers that can fit inside a miniature form factor to create a gesture detection system. The future work remaining primarily lies in doing gesture detection for more advanced gestures, like hand or finger swipes, or even more advanced gestures with fingers.

Acknowledgment

The authors would like to thank the following people for providing insight, advice and facilities that greatly assisted with the project: Professor Ian Hunter, Randall Miller Briggs, Span Spanbauer, and Nat Atnafu.

References

[1] S. Madakam and H. Date, "Security Mechanisms for Connectivity of Smart Devices in the Internet of Things" Springer, pp. 23–41, 2016

[2] D. M. van Willigen, E. Mostert and M. A. P. Pertijs, "In-air ultrasonic gesture sensing with MEMS microphones," *IEEE SENSORS 2014 Proceedings*, Valencia, 2014, pp. 90-93. doi: 10.1109/ICSENS.2014.6984940

[3] National Instruments, "The Fundamentals of FFT-Based Signal Analysis and Measurement in LabVIEW and LabWindows/CVI" *NI White Paper*, 2009. http://www.ni.com/white-paper/4278/en/

[4] Professor Ian Hunter, "2.131 Course Notes", *Massachusetts Institute of Technology*, 2018.

[5] APC International, Ltd., "Piezoelectricity" 2016 https://www.americanpiezo.com/knowledge-center/piezo-theory/piezoelectricity.html

Appendix B

Crosstalk Reduction

For each prototype, crosstalk voltage was also measured. For each array, the same transducer used in the displacement crosstalk measurements was driven at 20Vpp at or near its resonant frequency, and the voltage across the neighboring passive transducers was monitored. The results for each array are presented in the following sections. It should be noted that for each array, the voltage across the driving transducer matches between the simulated and measured results. This is because the voltage is fixed at 20Vpp. A more complete picture of crosstalk may be provided by observing the current across each transducer.

B.1 Increased Spacing Array

The voltage crosstalk for the increased spacing array was measured by driving the center transducer (2,2) with a 20Vpp, 44kHz sine wave and observing the voltage across the neighboring transducers. The measured peak voltage is plotted against the simulated peak voltage in Figure B-1. The measured crosstalk, excluding the two non-functional transducers, is 2.4 percent. The ratio of the measured to the simulated voltage is, on average, 0.4.

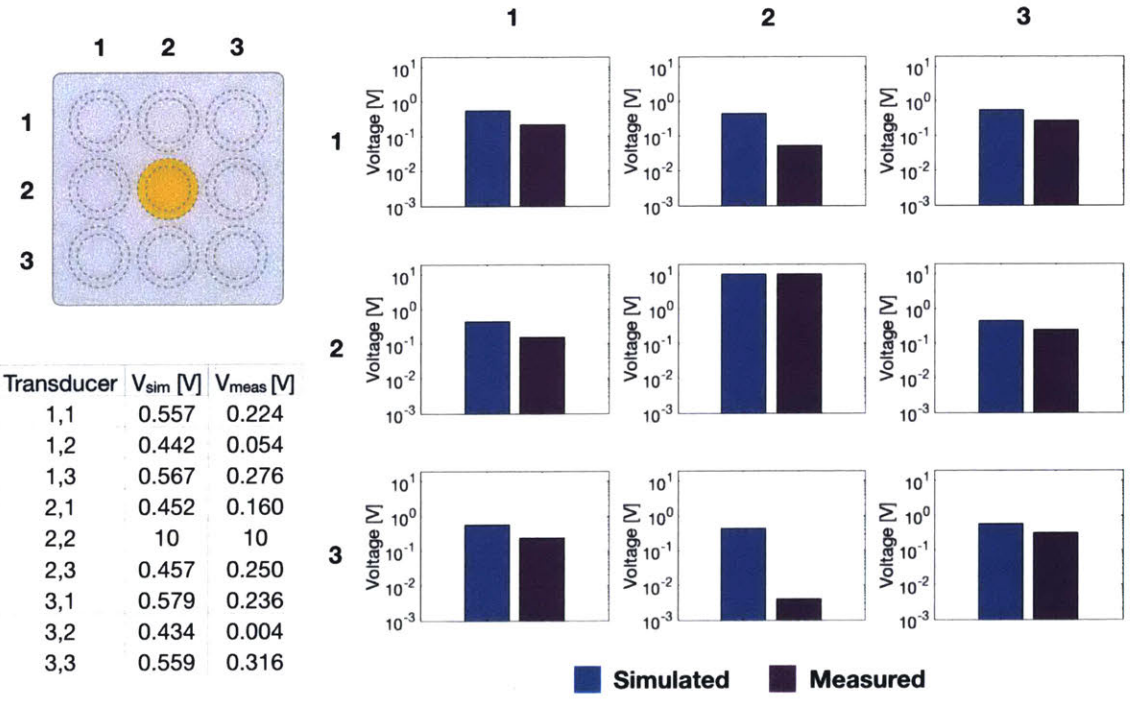

Transducer	V_{sim} [V]	V_{meas} [V]
1,1	0.557	0.224
1,2	0.442	0.054
1,3	0.567	0.276
2,1	0.452	0.160
2,2	10	10
2,3	0.457	0.250
3,1	0.579	0.236
3,2	0.434	0.004
3,3	0.559	0.316

Figure B-1: Simulated and measured voltage for the increased spacing array, with transducer (2,2) driven with a 44kHz, 20Vpp sine wave. The measured average voltage crosstalk, excluding two non-functional transducers, is 2.4%. The ratio of the measured to the simulated voltage is, on average, 0.4.

B.2 Moats Array

The voltage crosstalk for the moats array was measured by driving transducer (2,3) with a 20Vpp, 41kHz sine wave and observing the voltage across the neighboring transducers. The measured peak voltage is plotted against the simulated peak voltage in Figure B-2. The measured crosstalk, calculated using transducers (1,3), (2,3) and (3,3), is 16 percent. The ratio of the measured to the simulated voltage is, on average, 4.2.

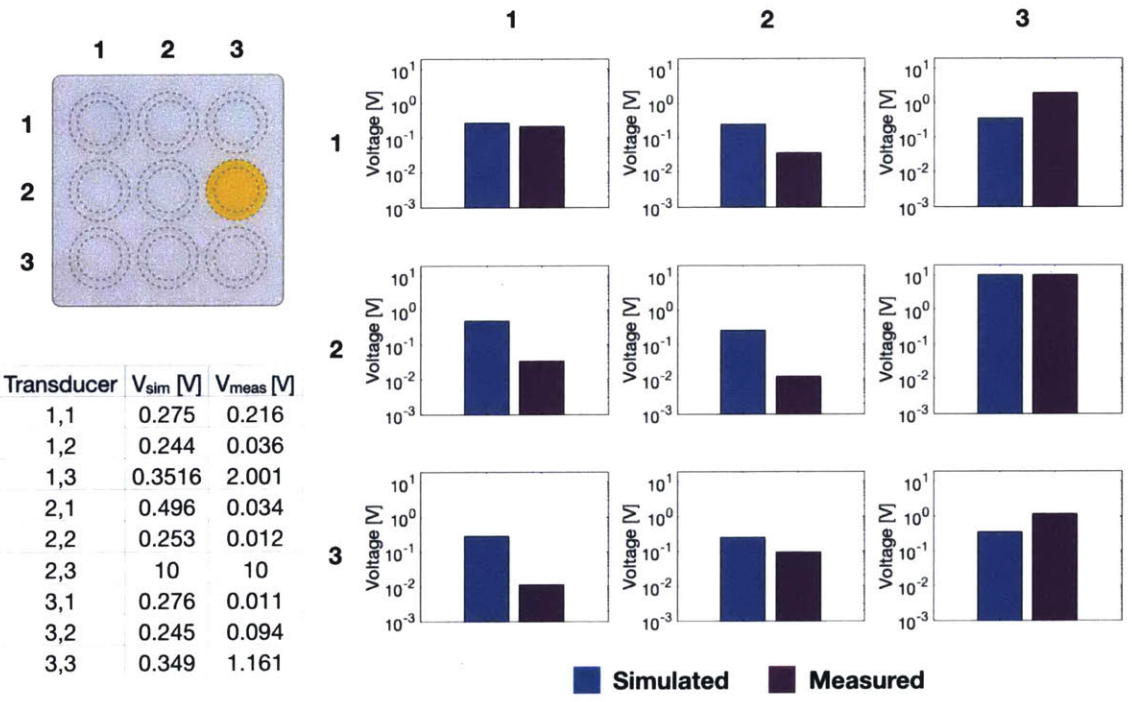

Transducer	V_{sim} [V]	V_{meas} [V]
1,1	0.275	0.216
1,2	0.244	0.036
1,3	0.3516	2.001
2,1	0.496	0.034
2,2	0.253	0.012
2,3	10	10
3,1	0.276	0.011
3,2	0.245	0.094
3,3	0.349	1.161

Figure B-2: Simulated and measured crosstalk voltage for the moats array, with transducer (2,3) driven with a 20Vpp, 41kHz sine wave. The average measured crosstalk is 15.8%. The average ratio of measured to simulated voltage is 4.2.

B.3 Stepped Array

The voltage crosstalk for the stepped array was measured by driving the center transducer (2,2) with a 20Vpp, 41kHz sine wave and observing the voltage across the neighboring transducers. The measured peak voltage is plotted against the simulated peak voltage in Figure B-3. The measured crosstalk is approximately 6.1 percent. The ratio of the measured to the simulated voltage is, on average, 2.6.

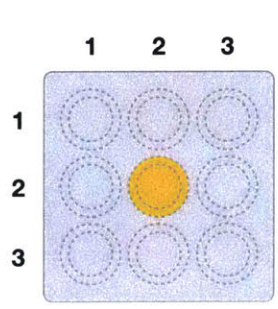

Transducer	V_{sim} [V]	V_{meas} [V]
1,1	0.209	0.440
1,2	0.241	0.561
1,3	0.200	0.561
2,1	0.245	0.821
2,2	10	10
2,3	0.243	0.581
3,1	0.211	N/A
3,2	0.246	0.741
3,3	0.208	0.581

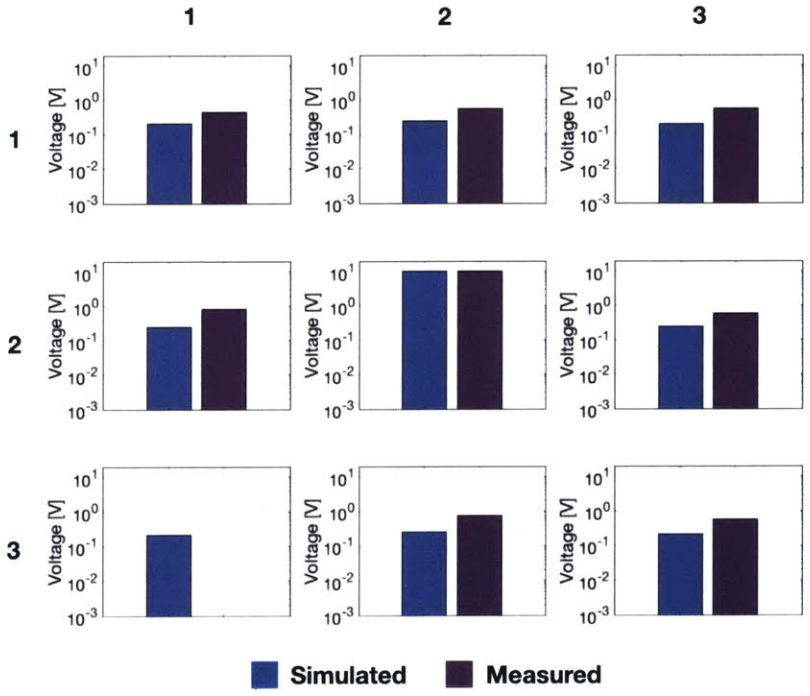

Figure B-3: Simulated and measured crosstalk voltage in the stepped array, when driving transducer (2,2) with a 20Vpp, 41kHz sine wave. The average measured crosstalk is 6.1% and the ratio of the measured to the simulated voltage is, on average, 2.6.

B.4 Voltage Crosstalk Discussion

The average predicted and measured voltage crosstalk for each array type is reported in Table B.1. There is a good deal of variation between the predicted and measured crosstalk. The closest match is for the original array, which has 9.9% error. There is also a large variation in absolute voltage between the measured and simulated values, as shown in Table B.2. The ratio of measured to simulated values is expected to be the same for voltage and displacement, as they are linearly related, but this is not the case.

Table B.1: Crosstalk voltage results.

Array Type	Predicted Average Crosstalk [%]	Measured Average Crosstalk [%]
Original	9.1	8.2
Increased Spacing	5.1	2.4
Moats	3.1	15.8
Stepped	2.3	6.1

Table B.2: Average ratio of measured to simulated values.

Array Type	Voltage	Displacement
Original	0.8	0.9
Increased Spacing	0.4	0.7
Moats	4.2	2.0
Stepped	2.6	1.3

These discrepancies may be due to the difference in mounting conditions between the displacement and voltage measurements. For measurements of displacement, the arrays were mounted to the vibrometer stage using Blu Tack and a 3D printed fixture, which clamped the edges of the array. For measurements of voltage, the array was mounted to the table with Blu Tack. It was assumed that the results could be compared because the array should be much stiffer than both the transducer

membranes and the mounting structure, and damping is added by the Blu Tack in each case. The reasonable agreement between the voltage and displacement results for the original prototype reinforced this assumption. However, it appears that the array is very sensitive to mounting conditions. More voltage measurements should be collected with the array mounted in the vibrometer fixture to test this hypothesis.

Appendix C

Hover Measurements

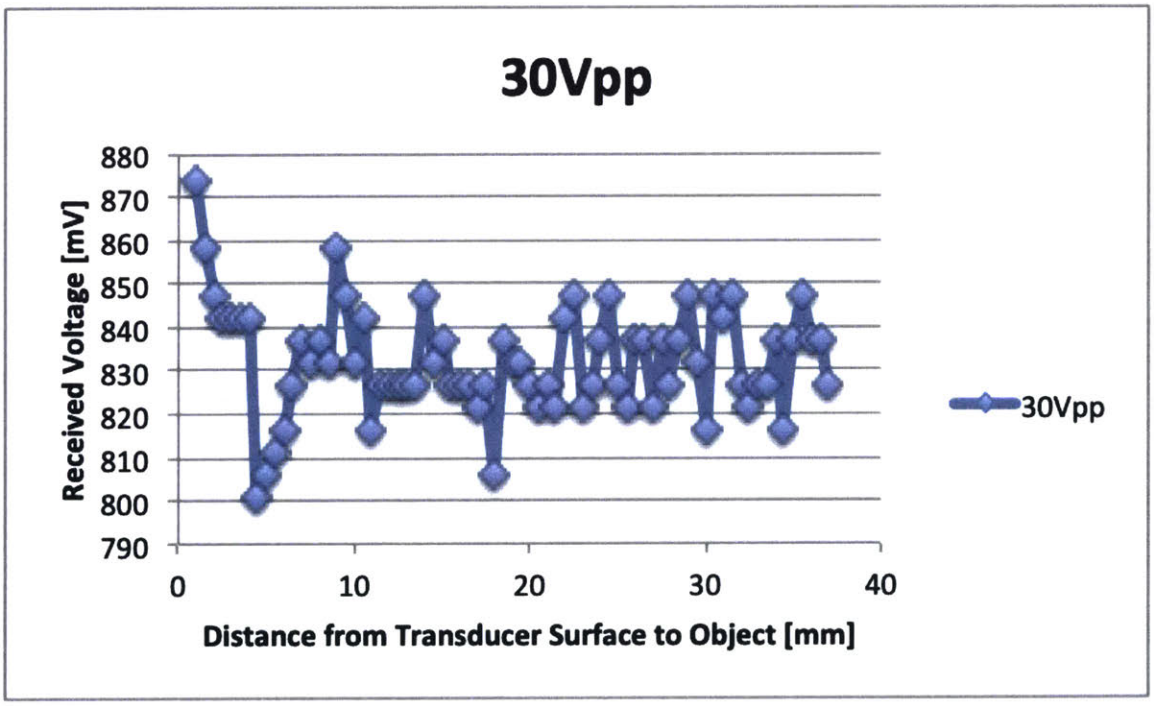

Figure C-1: Hover data for the original prototype driven at 30 Vpp. The received voltage with no hovering object is 830 mV.

As shown in 5-10, the measured hover data shows fairly good agreement with the predicted results up to a distance of about 3.5mm. However, measurements were taken out to a distance of about 35mm and show deviation from the predicted values. It is possible that this is due to the object being in the transducer's near field, whereas the calculations make far field assumptions. It is also possible that this is

due to the test setup, which uses a continuous sinusoidal signal to drive the central transducer. Interference between incoming and outgoing signals and reflections from the surrounding area may have lead to the observed peaks in pressure. Further testing should be done in an anechoic environment with different types of signals to understand the cause. A full simulation should also be run that takes into account the transmitter and receiver system simultaneously. The current simulation process records the pressure value from the transmitter model and then uses it as the amplitude of an incoming plane wave for the receiver model.

Appendix D

Off the Shelf Transducer Specifications

The MA40S4S and MA40S4R were used to validate the measurement process for transducer source level and sensitivity, as described in chapter 4. The transducer specifications given by the manufacturer are shown in Figure D-1 for reference.

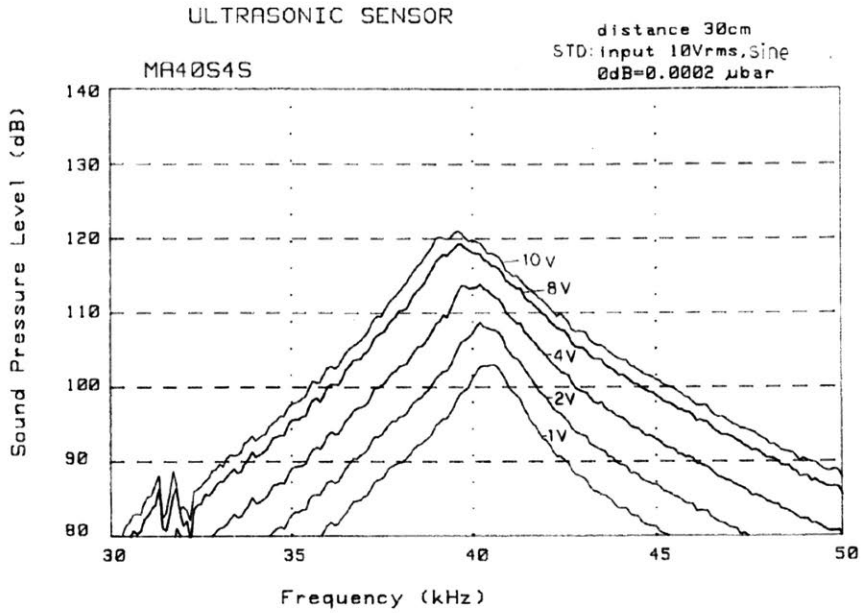

Fig.4 Frequency – Sound Pressure Level characteristic of MA40S4S (input voltage dependency)

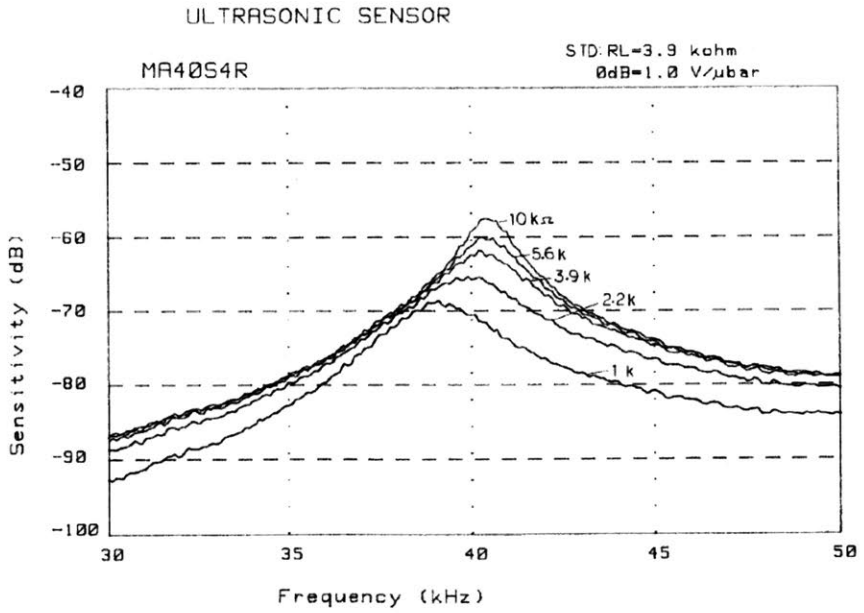

Fig.5 Frequency – Sensitivity characteristic of MA40S4R (load resistance dependency)

Figure D-1: Transducer specifications for the MA40S4S/R, reported by muRata.

Appendix E

Array with Epoxied Membrane

A version of the original transducer array was also made with the steel front plate separated into two parts, joined using epoxy. The frequency response for each transducer in this array is shown in Figure E-1. The frequency responses are much less consistent than in the array with the monolithic front plate. This could be improved by using tape-type epoxy, as used in circuit boards, which would give more control over the thickness and consistency of the epoxy layer.

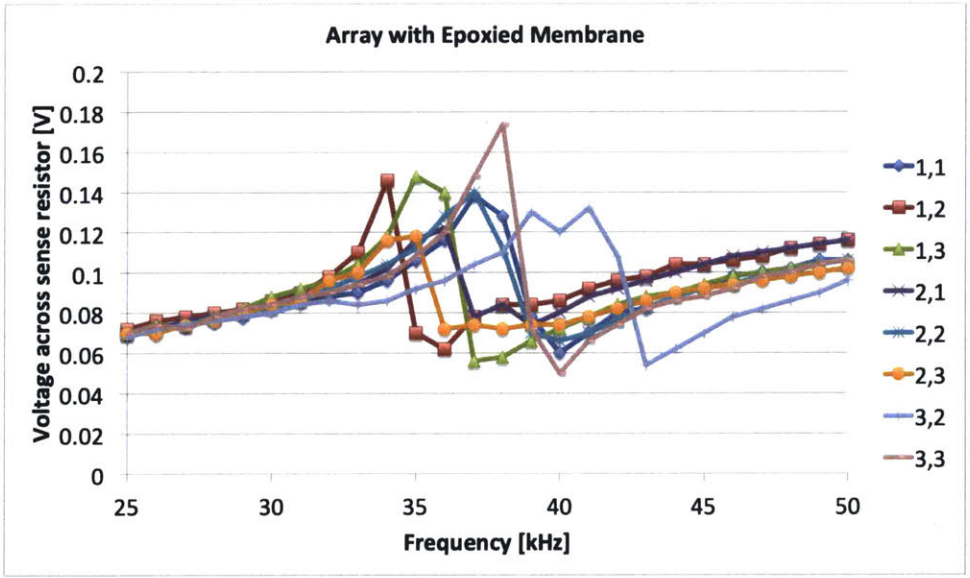

Figure E-1: Frequency response for each transducer in the array with the epoxied membrane.

Appendix F

Code

For code associated with this project, see:

https://github.com/juliacanning/GestureSensingFUT

Appendix G

Constant Definition

When optimizing geometry to maximize static deflection for an aluminum transducer using the analytical model and comparing the results to the simulation, the values in Table G.1 are used in the analytical equations.

Table G.1: Constant definition for geometry optimization in aluminum.

Variable	Value	Definition
a	0.005 m	membrane radius
h_m	5.0e-4 m	membrane thickness
S_m	1.4293e-11 $\frac{m^2}{N}$	membrane elastic compliance constant
ν_p	0.31	piezo Poisson's ratio
S_{11}^E	1.65e-11 $\frac{m^2}{N}$	piezoceramic elastic compliance constant
d_{31}	-2.74e-10 $\frac{m}{V}$	piezoelectric constant

When comparing the analytical, simulated and experimental results for the prototype array, the values in Table G.2 are used in the analytical equations.

Table G.2: Constant definition for analytical calculations for prototypes.

Variable	Value	Definition
a	0.0038 m	membrane radius
h_m	2.54e-4 m	membrane thickness
ρ_m	7870 $\frac{kg}{m^3}$	membrane density
Y_m	200e9 $\frac{kg}{ms^2}$	membrane Young's modulus
S_m	$\frac{1}{Y_m}$	membrane elastic compliance constant
ν_m	0.30	membrane Poisson's ratio
b	0.0032 m	piezo disk radius
h_p	3.0e-4 m	piezo disk thickness
ρ_p	7600 $\frac{kg}{m^3}$	density of piezo ceramic
Y_p	63e9 $\frac{N}{m^2}$	piezo Young's modulus
ν_p	0.30	piezo Poisson's ratio
S_{11}^E	$\frac{1}{Y_p}$	piezoceramic elastic compliance constant
d_{31}	-175e-12 $\frac{m}{V}$	piezoelectric constant
k_{31}	0.36	electromechanical coupling factor for a piezo plate for low frequencies
ϵ_{33}^T	$\frac{d_{31}^2}{S_{11}^E k_{31}^2}$	piezo permittivity in the direction of polarization under constant stress
m	0	vibration mode
λ^2	10.2158	constant related to vibration mode shape
c_m	343 m/s	sound speed in air
rho_m	1.225 $\frac{kg}{m^3}$	density of air
r_{ref}	0.03 m	reference distance
p_{ref}	2e-5 Pa	reference pressure in air
$\rho_0 c_{0,air}$	408 $\frac{kg}{m^2 s}$	acoustic impedance of air
$\rho_0 c_{0,fat}$	1.33e6 $\frac{kg}{m^2 s}$	acoustic impedance of fat

Appendix H

Touch & Hover Circuitry Photo

An image of the touch circuitry described in section 5.1 and the hover circuitry described in Appendix A is shown in Figure H-1.

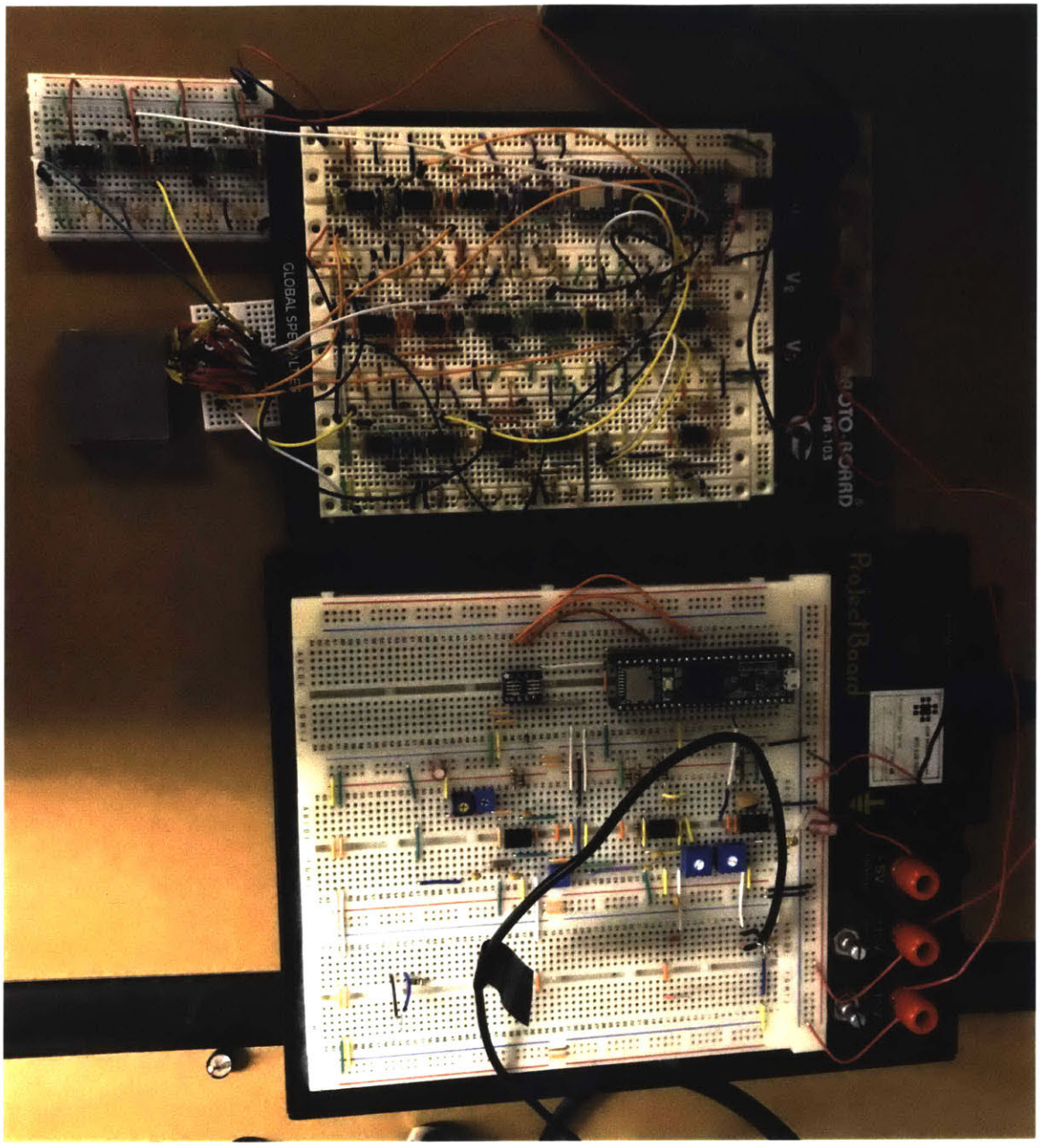

Figure H-1: Photo of touch and hover circuitry.

Bibliography

[1] Fernando Alonso-Martín, Juan Jos Gamboa-Montero, Jos Carlos Castillo, lvaro Castro-González, and Miguel ngel Salichs. Detecting and classifying human touches in a social robot through acoustic sensing and machine learning. *Sensors (Switzerland)*, 17(5), 2017.

[2] David Askew. Touch Technology.

[3] Che Wei Chang, Min Hung Chen, Kuan Chang Chen, Chi Ming Yeh, and Yi Chang Lu. Mask design for pinhole-array-based hand-held light field cameras with applications in depth estimation. In *2016 Asia-Pacific Signal and Information Processing Association Annual Summit and Conference, APSIPA 2016*, pages 1–4, 2017.

[4] Heng Tze Cheng, An Mei Chen, Ashu Razdan, and Elliot Buller. Contactless gesture recognition system using proximity sensors. *Digest of Technical Papers - IEEE International Conference on Consumer Electronics*, (1):149–150, 2011.

[5] COMSOL. Bracket - Frequency-Response Analysis.

[6] EMI Analyst. Coplanar Capacitance, 2019.

[7] Sidhant Gupta, Daniel Morris, Shwetak Patel, and Desney Tan. SoundWave: Using the Doppler Effect to Sense Gestures. In *Proceedings of the 2012 ACM Conference on Human Factors in Computing Systems - CHI '12*, pages 1911–1914, 2012.

[8] Jordan Hanania, Kailyn Stenhouse, and Jason Donev. Wien's Law, 2018.

[9] Matthew Hirsch, Douglas Lanman, Henry Holtzman, and Ramesh Raskar. BiDi Screen: A Thin, Depth-Sensing LCD for 3D Interaction using Light Fields. *ACM Transactions on Graphics*, 28(5), 2009.

[10] Shahram Izadi, Steve Hodges, Alex Butler, Darren West, Alban Rrustemi, Mike Molloy, and William Buxton. ThinSight - A Thin Form-factor Interactive Surface Technology. *Communications of the ACM*, 52(12):90–98, 2009.

[11] Kaustubh Kalgaonkar and Bhiksha Raj. ONE-HANDED GESTURE RECOGNITION USING ULTRASONIC DOPPLER SONAR. In *IEEE International Conference on Acoustics, Speech, and Signal Processing*, pages 1889–1892, 2009.

[12] Lei Kang, Andrew Feeney, Riliang Su, David Lines, Axel Jager, Han Wang, Yavor Arnaudov, Sivaram Nishal Ramadas, Mario Kupnik, and Steve Dixon. Two-dimensional flexural ultrasonic phased array for flow measurement. *IEEE International Ultrasonics Symposium, IUS*, pages 3–6, 2017.

[13] Keyence. What is a sensor? Sensor Basics.

[14] Thomas A. Kinney. Proximity Sensors Compared: Inductive, Capacitive, Photoelectric, and Ultrasonic, 2001.

[15] Nicola Lamberti, Giosu Caliano, and Alessandro Savoia. ACUPAD : A trackpad device based on a piezoelectric bimorph. *Sensors & Actuators: A. Physical*, 222:130–139, 2015.

[16] Arthur W. Leissa. *Vibration of Plates.* Scientific and Technical Information Division, Office of Technology Utilization, National Aeronautics and Space Administration, 1969.

[17] David H Levy. *Portable Product Miniaturization and the Ergonomic Threshold.* PhD thesis, Massachusetts Institute of Technology, 1997.

[18] Bau-Jy Liang, Don-Gey Liu, Chia-Hung Yeh, Hsiao-Chun Chen, Yu-Chen Fang, and Pi-Fang Hung. Analytical Calculation for Capacitances of Electrode Patterns in Touch Panels. *Optical Data Processing and Storage*, 3(1):67–78, 2017.

[19] Wojciech Matusik. MIT EECS 6.837 Computer Graphics Part 2 Rendering Today: Intro to Rendering, Ray Casting.

[20] Microchip. Touch and Input Sensing for Wearable Devices: Microchip 1-2-3D Innovative Electronics Solutions.

[21] Microchip Technology Inc. GestIC® Design Guide, 2016.

[22] Changki Mo, Rika Wright, William S. Slaughter, and William W. Clark. Behaviour of a unimorph circular piezoelectric actuator. *Smart Materials and Structures*, 15(4):1094–1102, 2006.

[23] Patrick Moorhead. Qualcomm's New Fingerprint Sensors Go Through Metal, Glass And Displays. *Forbes*, 2017.

[24] OmniVision Technologies. Datasheet - OV2640 Color CMOS UXGA (2.0 MegaPixel) CAMERACHIP with OmniPixel2 Technology, 2006.

[25] Ann P. Dowling and John E. Ffowcs-Williams. *Sound and Sources of Sound.* Halsted Press: a division of John Wiley & Sons, New York, New York, USA, 1983.

[26] Panasonic Corporation. Specifications for Infrared Array Sensor: Infrared Array Sensor Grid-EYE, 2011.

[27] Da-Chen Pang and Yu-Hsuan Chiang. A TRANSPARENT CAPACITIVE MICROMACHINED ULTRASONIC TRANSDUCER (CMUT) ARRAY FOR FINGER HOVER-SENSING DIAL PADS. In *IEEE Transducers*, pages 2171–2174, 2017.

[28] Richard J. Przybyla, Hao Yen Tang, Stefon E. Shelton, David A. Horsley, and Bernhard E. Boser. 3D ultrasonic gesture recognition. *Digest of Technical Papers - IEEE International Solid-State Circuits Conference*, 57:210–211, 2014.

[29] Yu Sang, Laixi Shi, and Yimin Liu. Micro hand gesture recognition system using ultrasonic active sensing. *IEEE Access*, 6:49339–49347, 2018.

[30] Alessandro Stuart Savoia, Barbara Mauti, and Giosu Caliano. A low frequency broadband flextensional ultrasonic transducer array. *IEEE Transactions on Ultrasonics, Ferroelectrics, and Frequency Control*, 63(1):128–138, 2016.

[31] Katherine Marie Smyth. *Design and Modeling of a PZT Thin Film Based Piezoelectric Micromachined Ultrasonic Transducer (PMUT).* PhD thesis, Massachusetts Institute of Technology, 2012.

[32] Fang Tang and Amine Bermak. An 84 pW/frame per pixel current-mode CMOS image sensor with energy harvesting capability. *IEEE Sensors Journal*, 12(4):720–726, 2012.

[33] H Tang, Y Lu, S Fung, J M Tsai, M Daneman, D A Horsley, and B E Boser. Pulse-echo ultrasonic fingerprint sensor on a chip. In *2015 Transducers - 2015 18th International Conference on Solid-State Sensors, Actuators and Microsystems, TRANSDUCERS 2015*, pages 674–677, 2015.

[34] Steve Taranovich. MEMS ultrasonic time-of-flight innovation: sensors advance user experiences, 2017.

[35] Touch International. Surface Capacitive Touch Screen Solutions.

[36] TouchSystems. SURFACE ACOUSTIC WAVE TECHNOLOGY (SAW).

[37] V Javier Traver, Pedro Latorre-carmona, Eva Salvador-balaguer, Filiberto Pla, and Bahram Javidi. Three-Dimensional Integral Imaging for Gesture Recognition Under Occlusions. 24(2):171–175, 2017.

[38] Masaya Tsuruta, Shuhei Aoyama, Arika Yoshida, Buntarou Shizuki, and Jiro Tanaka. Hover Detection Using Active Acoustic Sensing. In *International Conference on Human-Computer Interaction*, pages 104–114, 2016.

[39] Douwe M Van Willigen, Erwin Mostert, and Michiel A P Pertijs. In-Air Ultrasonic Gesture Sensing with MEMS Microphones. In *Sensors, 2014 IEEE*, pages 90–93, 2014.

[40] Piotr Wojtczuk, Alistair Armitage, T David Binnie, and Tim Chamberlain. PIR Sensor Array for Hand Motion Recognition. In *Sensor Devices 2011*, pages 99–102, 2011.